Structural and Electrical properties of (PVDF-TrFE)/$CoFe_2O_4$ nano-composites

By

Fahad Atta

DEPARTMENT OF PHYSICS

QUAID-I-AZAM UNIVERSITY

ISLAMABAD, PAKISTAN

2024

In the name of Allah, the Most Merciful, the Most Kind

This work is submitted as a dissertation

In partial fulfillment of the requirement for the degree of

MASTER OF PHILOSOPHY

IN

PHYSICS

To the

Department of Physics

Quaid-i-Azam University

Islamabad, Pakistan

CERTIFICATE

This is to certify that the experimental work in this dissertation has been carried out by ***Fahad Atta*** under my supervision in the Superconductivity and Magnetism Lab, Department of Physics, Quaid-i-Azam University, Islamabad, Pakistan.

Supervisor:

Prof. Dr. Ghulam Hassnain Jaffari

Department of physics

Quaid-i-Azam University

Islamabad, Pakistan

Submitted Through:

Prof. Dr. Kashif Sabeeh

Chairman

Department of Physics

Quaid-i-Azam University

Islamabad, Pakistan.

To

My Family

Acknowledgements

*All praise to be **Allah Almighty** the most Beneficent, Merciful and Gracious who gave me courage and energy to complete this research work. Peace and Blessings be upon the last Messenger 'The Holy Prophet Muhammad (S.A.W)' the most perfect and splendid.*

*I owe my deepest gratitude to my supervisor **Dr. Ghulam Hassnain Jaffari,** for his concern, insightful guidance, and persistent support during my research work and thesis. I am grateful to him for listening my ideas with such interest and patience and guiding me with the precious knowledge.*

My heartfelt thanks to my beloved parents, though you are no longer physically with us, your love, guidance, and unwavering support continue to shape every step of my journey. Your teachings and the values you instilled in me remain my guiding light, inspiring me to navigate life's challenges with resilience and grace. I am forever grateful for the precious moments we shared and the lessons you imparted. Your legacy lives on in my heart, and I strive to honor your memory by living a life that reflects the love and wisdom you showered upon me.

*And most importantly, I would like to pay my heartfelt thanks to my beloved brothers **Dr, Asif Atta**, **Muhammad Suleman** and **Hameed ullah** for their unconditional love, prayers and sacrifices for educating and preparing me for my future. My words would never be enough for all that they have done for me in life, from motivating and encouraging me at my worse to raising me to a person that I am today.*

*I am grateful to my seniors **M. Shahid Iqbal khan, Israr Ahmad** and all other for their support, guidance and helpful advices. Their valuable discussions have always been a source of inspiration for me throughout my research. I would like to pay my gratitude to my lab fellows specially **Jehanzad Zafar.** A special thanks to my school friends for their support and encouragement.*

*Finally, I am incredibly grateful to **Mr. Imran Khaliq**, my dedicated school teacher of physics, for his unwavering guidance and support throughout my educational journey. His passion for teaching and belief in my potential have been instrumental in shaping my growth. I extend my heartfelt appreciation to my former supervisor, **Dr. Rizwan Hussain**, whose mentorship and*

valuable insights have played a pivotal role in my professional development. His guidance has been a beacon of inspiration, illuminating my path to success.

Table of Contents

Chapter 1 Introduction

Chapter 2 Techniques and Characterization

Chapter 3 Structure and Characterization

Chapter 4 Results and Discussion

Table of Figures

Chapter 1 Introduction

Chapter 2 Techniques and Characterization

Chapter 3 Structure and Characterization

Chapter 4 Result and Discussion

List of Tables

Abstract

In present work, P(VDF-TrFE)/$CoFe_2O_4$ nanocomposite free-standing films are prepared, and their structural, electrical and magnetic properties are discussed in detail. $CoFe_2O_4$ nanoparticles are synthesized by a low-cost sol-gel method. While, free-standing P(VDF-TrFE)/$CoFe_2O_4$ nanocomposite films with varying $CoFe_2O_4$ (CFO) concentrations have been prepared using solvent casting (The drying casting method). XRD and FTIR techniques were used for structural analysis. The crystallinity of the films is affected by the addition of cobalt ferrite nanoparticles to P(VDF-TrFE). Fourier transform infrared spectroscopy reveals the presence of the beta-phase in all composite films. Reflectance is measured against energy, reveals the presence of the d-d transition associated with the CFO particles. Ferroelectric response at room temperature is measured by measuring polarization against electric field loops at frequency 10 Hz. P(VDF-TrFE) films show saturated ferroelectric hysteresis loops, indicating that the addition of TrFE monomers caused a high content β-phase. Good ferroelectric response has been achieved for low CFO concentration, while P(VDF-TrFE)/CFO films show non-saturated ferroelectric hysteresis loops at higher concentrations, confirming lossy capacitive behavior. Change in saturation and remanent polarization is observed and discussed in detail as a function of CFO concentration. A detailed analysis of the dielectric properties of P(VDF-TrFE) and P(VDF-TrFE)/CFO are done and their corresponding activation energies has been calculated. Both P(VDF-TrFE) and P(VDF-TrFE/CFO) nanocomposite films exhibit significant variations in the magnitude of the dielectric constant. Magnetic moment vs magnetic field loops is measured to observed the magnetic response of P(VDF-TrFE)/CFO nanocomposite films, which show ferromagnetic behavior. Additionally, the variation of magnetic moment due to the inhomogeneous distribution of CFO nanoparticles within the film from the center to the edge of the film is observed.

Chapter 1 Introduction

1.1. Introduction:

Richard P. Feynman's renowned speech, "There's plenty of room at the bottom," delivered in 1959, introduced a fresh perspective on the vast potential of the microscopic world. By drawing inspiration from the compact cell, which holds the entire blueprint of the human body, Feynman's address envisioned the ability to manipulate the configuration of atoms on a minute scale [1]. Nanoscale pertains to a size that is one billionth or 10^{-9} of a whole. When materials are reduced to the nanoscale level, their properties become distinct and differ from that of the atomic and bulk scale. Recently, there has been a lot of interest in the distinct electrical [2], optical [3], magnetic [4], and biological properties [5-7]. Due to their high s/v ratio (s = surface, v = volume), nanomaterials have unique properties that are further influenced by quantum effects as a result of the restricted migration of electrons [6]. These materials are therefore extensively used in a number of industries, including biomedicine, agriculture, defense, and security, as well as electronics, energy storage, and communication, to name just a few [7].

Due to their small size, nanoparticles are essential elements in the fields of nanoscience and nanotechnology. They serve as the perfect building blocks for larger nanostructures. These particles, which can contain one or more atomic species or molecules, are comprised of up of clusters of atoms and molecules and range in size from 1 to 100 nm. The qualities of nanoparticles depend heavily on their size, which causes a range of traits to be displayed by them [8].

Polymer composite materials have attracted the attention of both scholars and business in recent decades. Greek terms "poly" (which means "many") and "mers" (which means "parts") are the source of the English word "polymer." A polymer chain is made up of several monomers—repeating units—that are joined together by covalent bonds to form the chain. Copolymers are polymers that contain multiple different types of monomers [9].

A polymer composite is made up of two or more components, such as a rigid and durable filler and a binder or matrix (polymer) that holds the filler in place. Both the filler and the matrix directly affect the final qualities of the composite while yet maintaining their distinct identities. [10]. The use of these materials in polymer composites has gained popularity as nanotechnology

and nanomaterials become more significant. Today, polymer nanocomposites are made commercially and used in many different fields, such as solar energy conversion, optics, piezoelectric sensors, batteries, microelectronics, and biotechnology. Polymer nanocomposites can be prepared in a variety of ways to attain different characteristics. The interaction of the nanoparticles and polymer matrix in polymer nanocomposites is crucial for determining their final characteristics and electrical properties [11].

This chapter covers a thorough investigation of the materials' dielectric properties, including ferroelectricity, piezoelectricity, and pyroelectricity as well as polarization mechanisms in dielectrics. It also offers a brief introduction to the primary materials of interest in our current investigation, including Poly (Vinylidene Fluoride) (PVDF), Poly (Vinylidene Fluride-Trifluoroethylene) P(VDF-TrFE) and Cobalt Ferrite ($CoFe_2O_4$).

1.2. Dielectric material:

"Dia" means "through/across" thus a dielectric is a material that allows electric flux or fields to pass through it, but not electrons [12]. When electric field is applied, these materials get polarized. Charges only move within the material and shift only when electric field is applied. This polarization results in positive charges moving slightly towards the applied field's direction while negative charges flows in the opposite direction, creating an internal electric field called depolarizing field. As a result, it decreases the net electric field inside the dielectric [13]. The response of dielectric materials to an electric field is shown in figure 1.1. The figure illustrates that E_o signifies the external electric field, while E_p indicates the electric field produced internally by the material. This internal field acts in the opposite direction to the applied field.

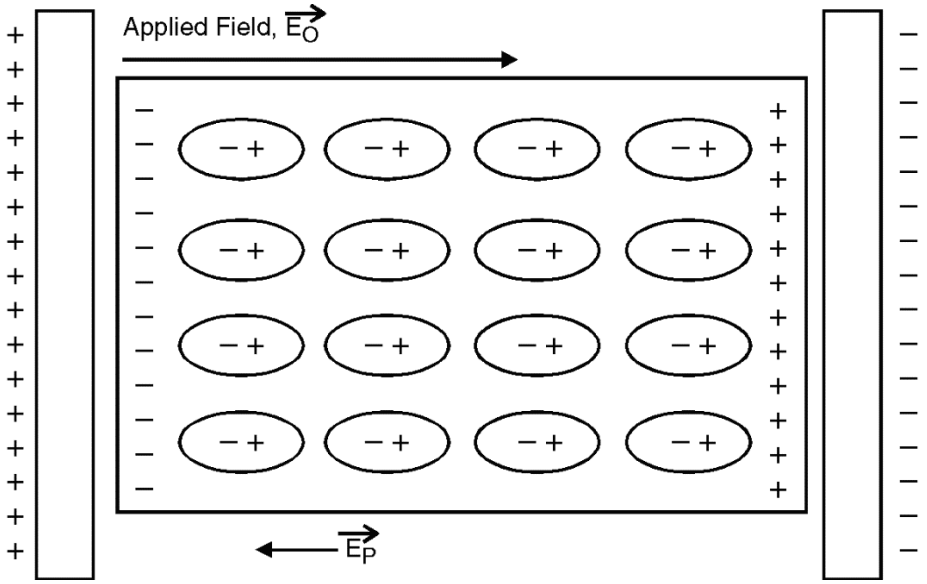

Figure 1.1 Induced Polarization in Dielectric when Placed in an External Electric Field [14]

The ratio of the dielectric material's permittivity (ε) to the free space permittivity (ε_o) is known as relative permittivity also called dielectric constant. Mathematically:

$$\varepsilon_r = \frac{\varepsilon}{\varepsilon_o} \tag{1.1}$$

This is a complex quantity which comprised of two components: the in-phase part (ε'), which reflects the induced polarization within the material, and the out-of-phase part (ε''), which indicates the energy losses. The dielectric constant is an innate property of a material and is affected by factors including its structure, temperature, and the frequency of the applied electric field [15].

1.3. Polarization:

The dipole moment (p) is a geometric representation of the distance between two opposite charges of the same magnitude, denoted by (q), and separated by a distance (r) given by:

$$\boldsymbol{p} = q\boldsymbol{r} \tag{0.2}$$

Its orientation, which is from the negative charge to the positive charge, indicates that it is a vector quantity. When an external electric field is applied to dielectric materials, the material's internal dipole moments align with the field's direction i.e. polarized the material. Polarization can be defined as total dipole moments ($\sum P$) per unit volume (V) [16].

$$P = \frac{\sum P}{V} \quad 0.3$$

The redistribution of charges can also be termed as Electric Polarization [15]. Five main types of Electric Polarization are explained below:

1.3.1. Electronic Polarization:

Dielectric materials display electronic polarization, or atomic polarization, when exposed to an electric field. Under normal conditions, the center of the electronic cloud and the positive nucleus are in the same position [15]. However, when dielectric material is placed in external electric field, it causes the negatively charged electronic cloud and positively charged nuclei to displace relative to each other, creating an electric dipole as shown in figure 1.2. This displacement can occur with a strong enough electric field (E).

$$P_E = \alpha_E E \quad 0.4$$

where,

$$\alpha_E = 4\pi\epsilon_o R^3 \quad 1.5$$

As we know $V_{atm} = \frac{4}{3}\pi R^3$ so put it in eq. 1.4

$$\alpha_E = 3\epsilon_o V_{atm} \quad 0.6$$

Where V_{atm} volume of atom, R is is the radius of atom, α_E is the Electronic Polarizability and is defined as the induced dipole moment that results from a given strength of an applied electric field. This property is directly influenced by the volume of the electronic shell and is not affected by changes in temperature [15].

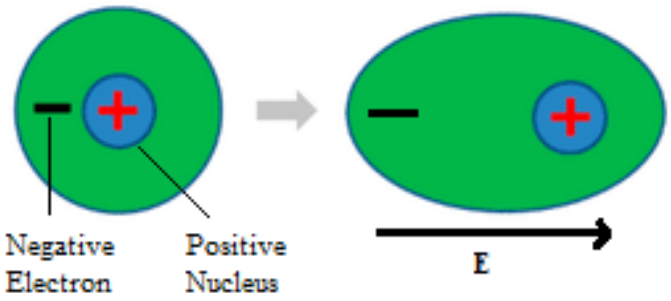

Figure 1.2 Displace the Centroid of Electron Cloud under the Application of Electric Field [17]

1.3.2. Ionic Polarization:

Ionic polarization occurs in ionic materials as they are composed of positively and negatively charged ions. While possessing dipoles, their polarization is typically neutralized in the absence of an external field, since the positive and negative ion dipoles offset each other. Applying an electric field (*E*), however, the cations and anions are shifted slightly in opposite directions, giving rise to a net dipole moment as depicted in figure 1.3. It is also known as vibrational polarization [15].

$$P_i = \alpha_i E \qquad 1.7$$

Where the average dipole moment per unit electric field is ionic polarizability α_i. Ionic polarizability surpasses electronic polarizability in value and is not influenced by temperature [18].

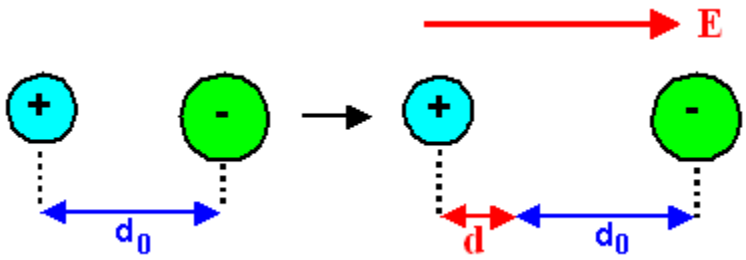

Figure 1.3 Displacement of ions under the Electric Field in Ionic Polarization [19]

1.3.3. Orientational polarization:

Polar molecules such as H_2O and HCl possess a permanent dipole moment, resulting in orientation polarization. However, these dipoles randomly align in all directions in the absence of an electric field, therefore they do not show net polarization. The average dipole moment as a result of this randomness is zero. The dipoles line up in the field's direction when an electric field (*E*) is introduced, resulting in Orientational or dipolar polarization as shown in figure 1.4.

Mathematically

$$P_o = \alpha_o E \qquad 0.8$$

Where α_o is the Orientational Polarizability and is equal to

$$\alpha_o = \frac{p^2}{3KBT} \quad 0.9$$

This phenomenon is dependent on temperature, because the thermal energy of the molecules increases as the temperature rises, affecting their alignment, which distinguishes it from the polarizability caused by electronic and ionic effects.

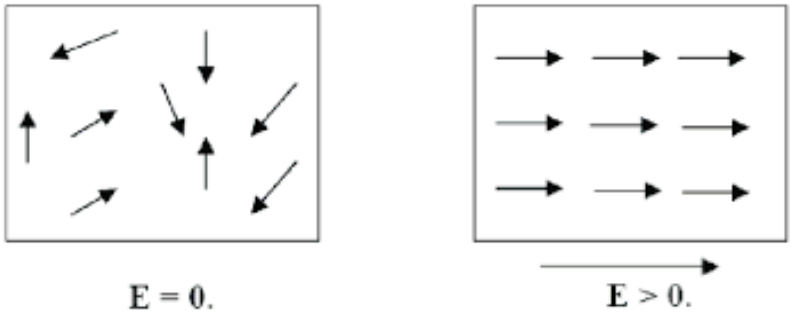

Figure 1.4 Orientation of Dipole under Electric Field in Orientational Polarization [20]

1.3.4. Space charge polarization:

Space charge polarization, also referred to as interfacial polarization, occurs in ceramics when charge carriers accumulate between different regions of a single crystal, at grain boundaries, or at the interface of polycrystalline dielectric materials. Unlike point-like charges, space charge refers to the distribution of charges over a region of space as shown in figure 1.5. Space charge polarization is caused by defect sites within the dielectric material, which is an inevitable phenomenon. The presence of charges at grain boundaries causes an increase in the dielectric constant. At higher temperatures, these charges become involved in the conduction mechanism, resulting in the Maxwell Wagner relaxation phenomenon in dielectrics [21]. The equation that describes the relationship between external field and space charge polarization is given as:

$$P_{SC} = \alpha_{SC} E \quad 0.10$$

where α_{SC} is the space charge polarizability.

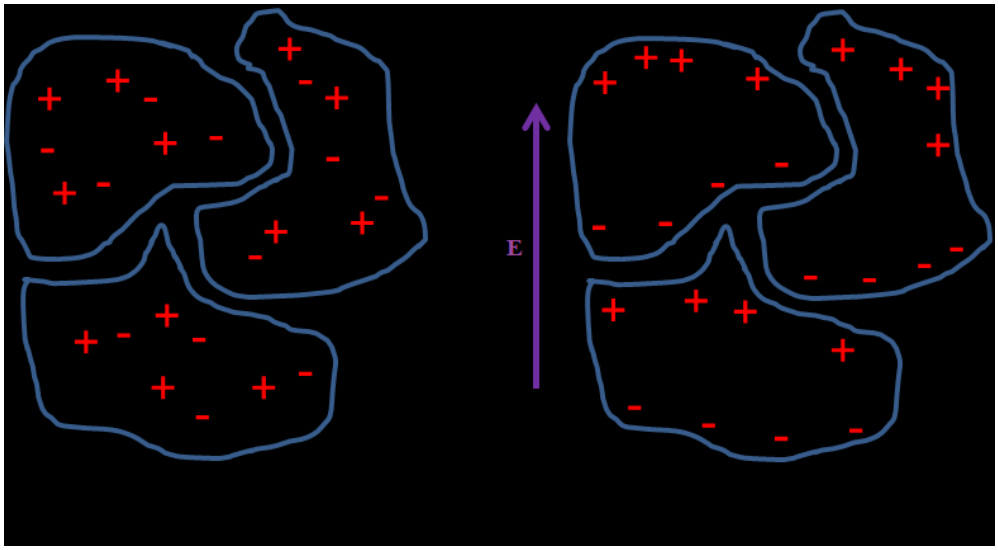

Figure 1.5 Charges at gain boundaries in Space Charge (Interfacial) Polarization [22]

Relaxation time of the above studied polarization and comparison between them are shown in figure 1.6.

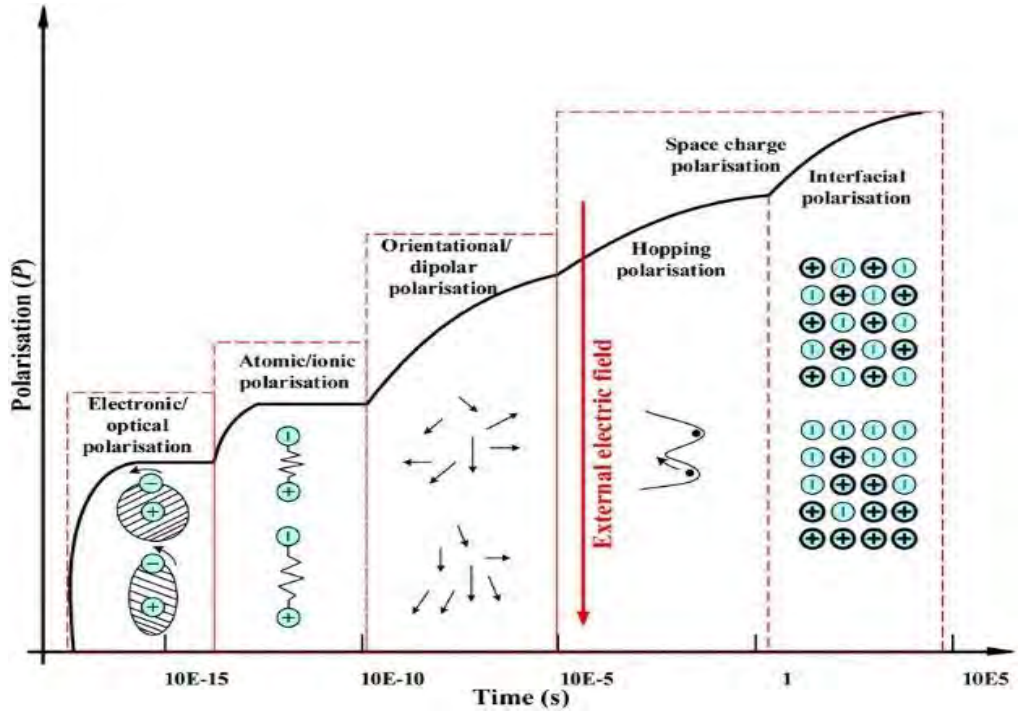

Figure 1.6 Different Type of Polarization vs their Relaxation Time [23]

1.3.5. Spontaneous Polarization:

Materials with an ordered non-centrosymmetric structure exhibit spontaneous polarization, where each unit cell's dipole moment is orientated naturally parallel to the dipole moment of its neighboring unit cells, resulting in the formation of domains with a specific polarization direction. This process requires an increase in free energy. However, the growth of a particular domain will cease once it reaches a certain size, and another domain will develop with a different polarization direction to minimize the free energy [15]. Under the electric field the net electric polarization increase but when we remove the field we will have the net polarization greater than 0.

1.4. Dielectric constant:

Dielectric materials exhibit induced polarization that is directly proportional to an externally applied electric field, given as

$$\vec{P} = \varepsilon_o \chi \vec{E} \qquad 0.11$$

Where ε_o is the permittivity of free space and χ is the dimensionless electrical susceptibility [13]. When a dielectric material satisfies the equation 1.10, it is considered a linear dielectric. Electric flux density, also known as electrical displacement (D), is a critical quantity in dielectrics that describes the displacement of charges per unit area caused by an external applied field. It is given as

$$\vec{D} = \varepsilon_o \vec{E} + \vec{P} \qquad 0.12$$

We know $\vec{P} = \varepsilon_o \chi \vec{E}$ so put in equation 1.12

$$\vec{D} = \varepsilon_o \vec{E} + \varepsilon_o \chi \vec{E}$$

$$\vec{D} = \varepsilon_o (1 + \chi) \vec{E} \qquad 0.13$$

$$\vec{D} = \varepsilon \vec{E}$$

as,

$$\varepsilon = \varepsilon_o (1 + \chi)$$

where ε is the permittivity of the medium.

Dielectric constant or relative permittivity is defined in section 1.2 can also be quantifies the capacity of a dielectric material to store electrical energy when subjected to an electric field. On the other hand, permittivity is a measurement of a dielectric's capacity to tolerate or enable the application of an external electric field. A higher permittivity of a material implies a stronger polarization response. Therefore, for applications needing high storage capacitance, dielectric materials with high permittivity values are preffered. [24]. Dielectric constant can be effected by different factors such as,

1. Frequency
2. Structure
3. Temperature

1.4.1. Effect of Frequency:

The realignment of polarization in a dielectric substance with a change in the direction of external electric field does not occur instantaneously. Instead, it takes a certain amount of time, termed as relaxation time, for the polarization to align fully with the new direction of the electric field. Different polarization mechanisms, such as electronic, ionic, molecular, and interfacial, have distinct resonance or relaxation frequencies at which they exhibit a significant effect on the net dielectric constant. For example, electronic and ionic polarization resonance occurs when the natural frequency of electrons and ions, which is around 10^{11} to 10^{13} Hz, becomes equal to the applied frequency. Molecular polarization has a relaxation time of 10^{-11} s, so it doesn't occur at frequencies greater than 10^{11} Hz. At higher frequencies, electronic and ionic polarization predominates, while at lower frequencies, space charge polarization is dominant. In addition, in the ultraviolet-visible spectrum, electronic polarization becomes active, ionic in the infrared spectrum, and orientational polarization in the microwave spectrum. [25]. Effect of frequency on dielectric constant is shown in figure 1.7.

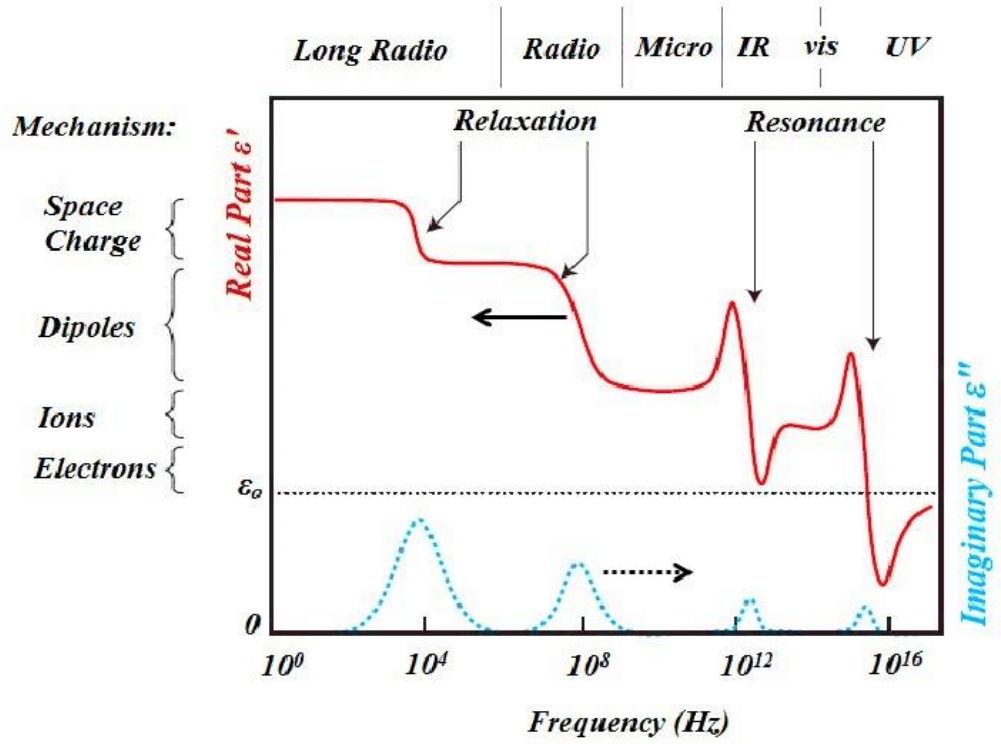

Figure 1.7 Effect of Frequency on Dielectric Constant [26]

1.4.2. Effect of Structure:

The material's structure also has an impact on the dielectric constant. Materials that have a greater number of polarization mechanisms tend to have a higher dielectric constant. For instance, polymers with more mobile chains have higher dielectric constants. The dielectric constant of polar materials, which have permanent dipoles, is larger than that of non-polar materials. Additionally, the magnitude of polarization and thus the dielectric constant depends on the density and magnitude of dipoles in polar materials [27, 28]. Consequently, materials with a high density and magnitude of dipoles have higher dielectric constants than those with lower density and magnitude of dipoles. For example, materials such as barium titanate ($BaTiO_3$), which have a non-centrosymmetric structure, exhibit large values of spontaneous polarization and therefore have higher dielectric constants than those with a centrosymmetric structure [29, 30].

1.4.3. Effect of temperature:

The dielectric constant of polar materials with permanent dipoles is strongly affected by temperature due to the influence of heat on polarization orientation. The alignment of molecules

with respect to the applied electric field is disturbed at higher temperatures, causing them to move randomly and resulting in a decrease in the dielectric constant. However, this does not always imply that when temperature rises, the dielectric constant will decrease. Defects and space charges can induce polarization, causing the dielectric constant to increase as the temperature rises. The dielectric constant can increase significantly at higher temperatures because mobile charge carriers generated at elevated temperatures accumulate at the grain boundaries [27, 31].

1.5. Magnetic Materials:

The first magnetic material studied in depth is lodestone (Fe_2O_3) [32]. Magnetism originates from the movement of electrons, specifically their orbital and spin motions. The electrons within an atom arrange themselves in a way that their magnetic moment, which includes both orbital and intrinsic magnetic moments, cancels out. However, when there is an unpaired electron in the *d* subshell of rare earth metal or *f* subshell of transition metals, it behaves like a tiny magnet with a magnetic moment and leads to magnetism. The magnetic ordering in crystalline magnetic materials arises due to exchange interactions between these localized moments. These materials exhibit four different types of magnetic ordering. [33].

- Paramagnetism
- Ferromagnetism
- Anti-ferromagnetism
- Ferrimagnetism

When there is no magnetic field, paramagnetic materials do not exhibit magnetic properties since their dipole moments are randomly aligned and result in a net magnetic moment of zero. However, the dipole moments of these materials align in the direction of the applied field when they are exposed to a magnetic field. When the field is removed, this ordering is disappeared. [33].

Ferromagnetic materials possess permanent magnetic moments and exhibit spontaneous magnetization when exposed to an external magnetic field. Even when the applied field is removed, the permanent dipoles remain aligned in that direction and continue to be magnetic. However, beyond a certain temperature called Curie temperature, ferromagnetic materials undergo a phase transition to become paramagnetic materials. At higher temperatures, the thermal motion causes misalignment of dipoles with the applied field, leading to the disappearance of spontaneous

polarization at the Curie temperature. As a result, the material responds to the applied field paramagnetically.

In contrast to ferromagnetic materials, antiferromagnetic materials have magnetic moments that are of equal magnitude but are arranged in opposite directions to each other, as illustrated in figure 1.8. Antiferromagnetic ordering occurs at low temperatures, known as the Neel temperature, above which the material behaves paramagnetic, while ferrimagnetic materials exhibit spontaneous magnetization due to the anti-parallel alignment of their magnetic moments, which have unequal magnitudes as depicted in figure 1.6.

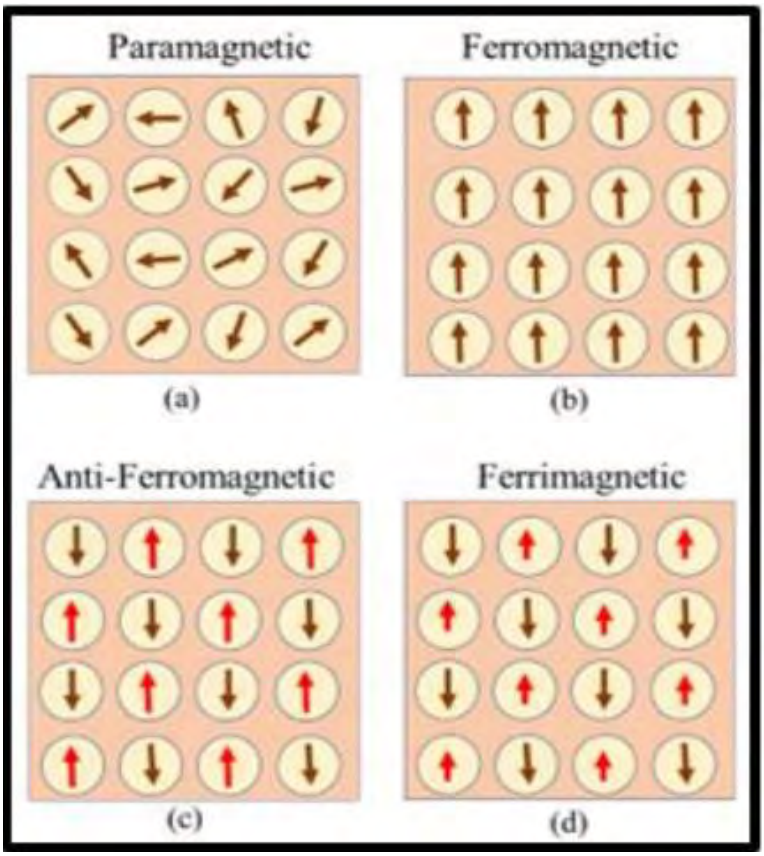

Figure 1.8 Magnetic Ordering (a) Paramagnetic (b) ferromagnetic (c) Anti-ferromagnetic (d) ferrimagnetic [33]

1.6. Ferroelectricity:

Ferroelectric materials are a unique category of insulators that exhibit spontaneous polarization, even in the absence of an external electric field. This phenomenon occurs in materials

with an electrically ordered crystalline structure, where the dipole moment of each unit cell is aligned with its neighboring unit cells. As a result, a domain structure is formed, which increases the free energy of the system. To lower this free energy, an additional domain with dipole moments pointing in the opposite direction is created. Therefore, multiple domains with dipole moments pointing in opposite directions are formed within a single crystal. The vector sum of these dipole moments is zero. When an external electric field is applied, these randomly oriented domains align themselves in the direction of the field, which results in a net electric polarization within the crystal. Even after the field is removed, the dipole moments are not completely randomized, and polarization still exists in the material as shown in the figure 1.9. The relationship between polarization and electric field is illustrated by a hysteresis loop [15, 34].

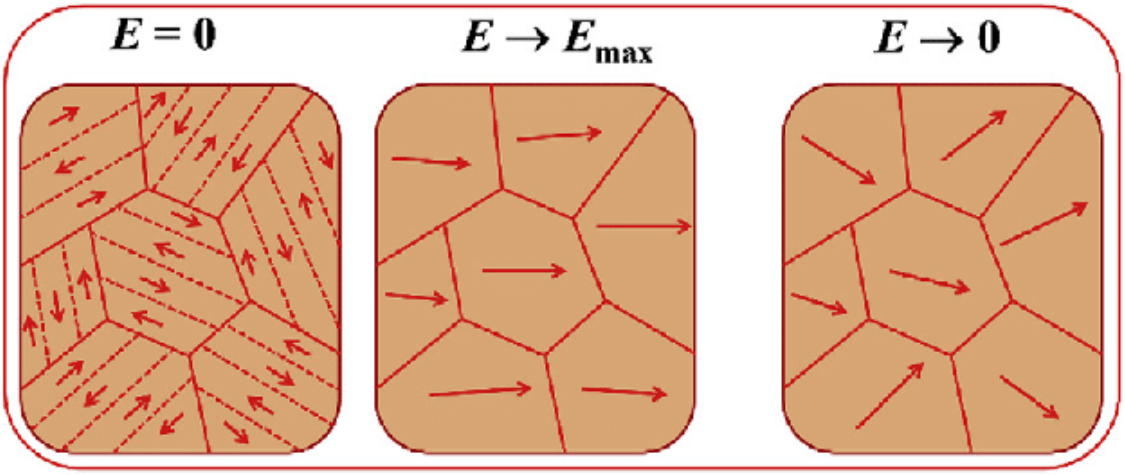

Figure 1.9 Domain Structure of Ferroelectric [35]

1.6.1. Ferroelectric hysteresis loop (P-E loop):

Ferroelectric materials demonstrate a reversible spontaneous polarization where the direction of polarization can be switched by applying an electric field in the opposite direction. The switching behavior of spontaneous polarization can be illustrated by a hysteresis loop.

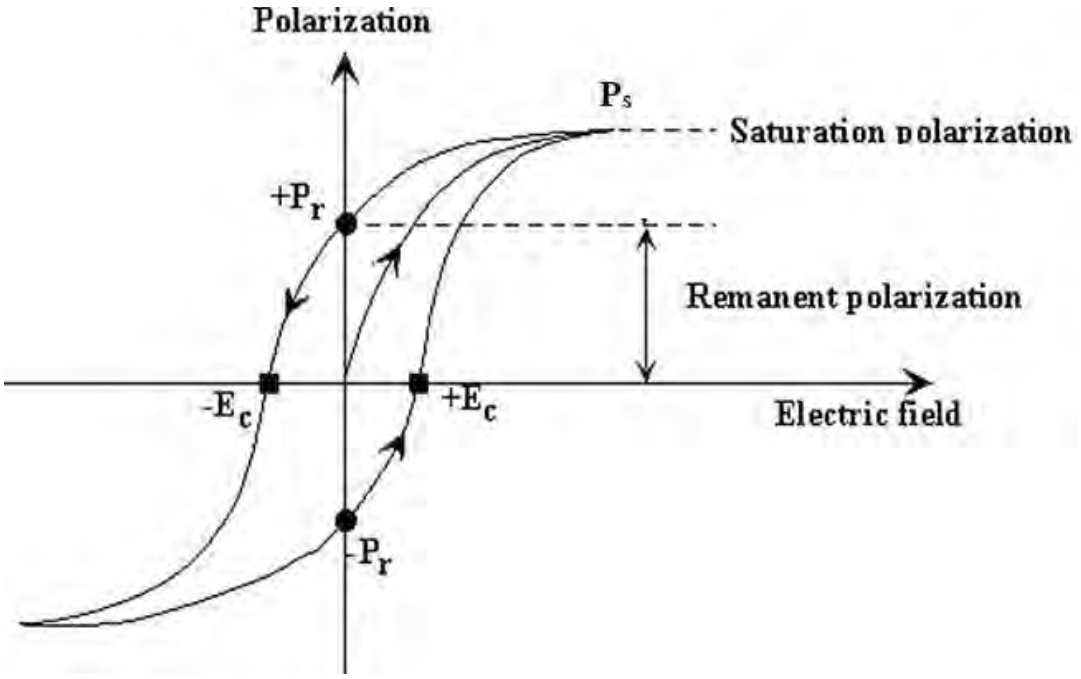

Figure 1.10 Ferroelectric Hysteresis Loop [36]

Ferroelectric hysteresis loop is characterized by three parameters: saturation polarization P_s, remnant polarization P_r, and coercive field E_c. When an electric field is applied to a ferroelectric material, the domains within the material start aligning in the direction of the field. As the field is increased, more and more domains align in the field direction until all domains are aligned and the polarization reaches its maximum value P_s.

Once all the domains are aligned, further increasing the electric field will not increase the polarization any further. When the electric field is slowly decreased to zero, the polarization also decreases but does not completely vanish. This is due to the fact that the domains are not completely randomized upon removal of the electric field, resulting in some residual polarization known as remnant polarization, which can only be removed by applying an electric field in the opposite direction. The field strength required to reduce the polarization to zero is known as the coercive field, E_c, and its value depends on the temperature and frequency of the applied field [15, 34]. When the electric field is reversed, the dipoles within the ferroelectric material align in the opposite direction, and reversing the field again creates a loop-shaped curve known as the hysteresis loop.

1.6.2. Phase Transition in Ferroelectrics:

Ferroelectric materials exhibit spontaneous polarization only below a critical temperature T_c, above which they become non-polar and behave like paraelectric materials. The change in spontaneous polarization above T_c is a result of a structural change in the unit cell, which is referred to as the ferroelectric phase transition [36]. Beyond T_c, the material completely loses its ferroelectric properties, and this transition temperature is called the Curie temperature (T_c).

However, ferroelectric properties can still be induced above T_c by applying an electric field above a certain threshold. Moreover, a significantly large electric field can shift T_c to higher temperatures. As the temperature approaches T_c, the dielectric constant displays an anomalous behavior and increases rapidly to a very high value. Above T_c, the dielectric constant follows Curie-Weiss law which is given by;

$$\varepsilon(T > T_c) = \frac{C}{T - T_c}$$

The change in spontaneous polarization in ferroelectric materials can either be continuous or discontinuous. A discontinuous change is referred to as a first-order transition, such as in Barium Titanate, while a continuous change is known as a second-order transition, such as in Rochelle salt [15].

1.7. Piezoelectricity:

Piezoelectricity is a phenomenon in which crystalline materials generate polarization due to the application of mechanical stress. This effect occurs in materials with a non-centrosymmetric crystal structure. When a piezoelectric material undergoes compression or mechanical deformation, a shift in the positions of its positive and negative charges takes place, resulting in the material becoming polarized, known as the direct piezoelectric effect. Piezoelectric materials also exhibit the converse or inverse piezoelectric effect, in which an electric field applied to the crystal causes mechanical deformation. Examples of important piezoelectric materials include Barium Titanate ($BaTiO_3$), lead zirconate titanate (PZT), quartz, polyvinylidene fluoride (PVDF), polyvinyl fluoride (PVF), and lithium niobate [15].

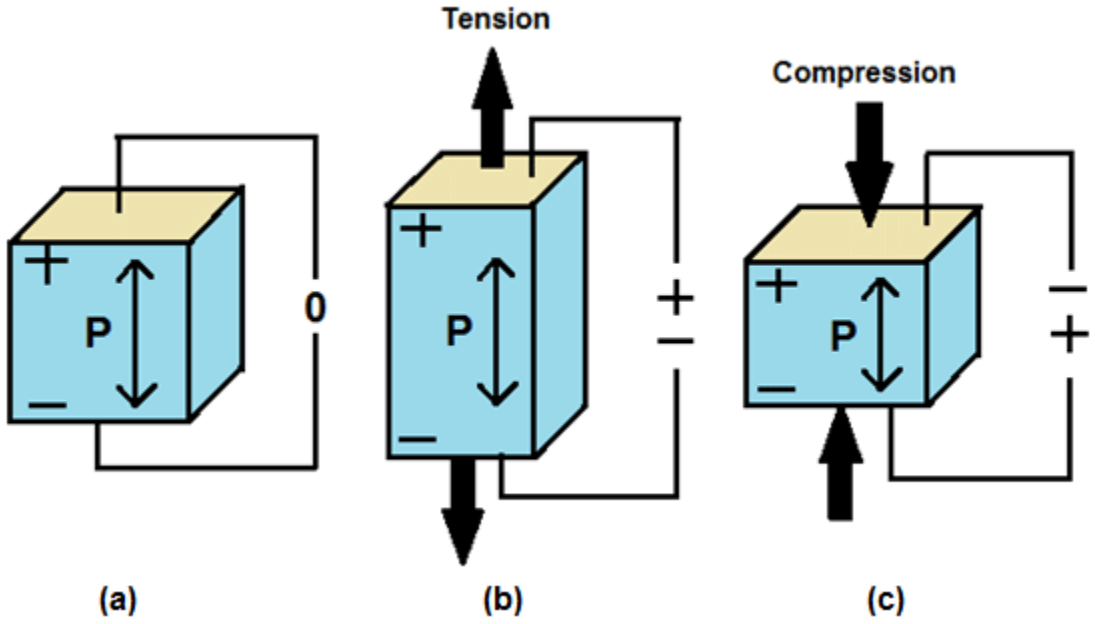

Figure 1.11 Piezoelectricity [37]

1.8. Pyroelectricity:

The pyroelectric effect refers to the alteration of a material's polarization due to a change in its temperature, resulting in a displacement of its atoms from their neutral position. Non-uniform temperature variations cause the material to experience a temperature gradient, which causes mechanical stress and piezoelectricity. In these circumstances, both pyroelectric and piezoelectric effects are observable. However, if the temperature change is uniform throughout the material, only the pyroelectric effect is present [15].

1.9. Ferrites:

The term 'ferrite' has its roots in the Latin word 'ferrum' which means iron. The earliest known magnetic material used by humans was lodestone, which consists of magnetite (Fe_2O_3) ore. Contrarily, ferrite, a particular kind of ceramic substance created by mixing iron oxide with a metallic element, serves as an insulator that is electrically non-conductive. Around 800 BC, ferrites are thought to have been found for the first time in ancient Greece. Ferrites emerged as a result of Forestier's 1928 heat treatment method, and they became important commercial materials in 1947 [38, 39]. As television became more commonly used in the 1950s, the ferrite sector saw enormous expansion. This was because ferrite cores, which are perfect for use in high-voltage transformers

and electron beam deflection yokes due to their magnetic characteristics, electrical resistivity, and low magnetic losses [40].

1.10. Classification of Ferrites:

Based on their magnetic characteristics and crystal formations, ferrites are divided into the following classes.

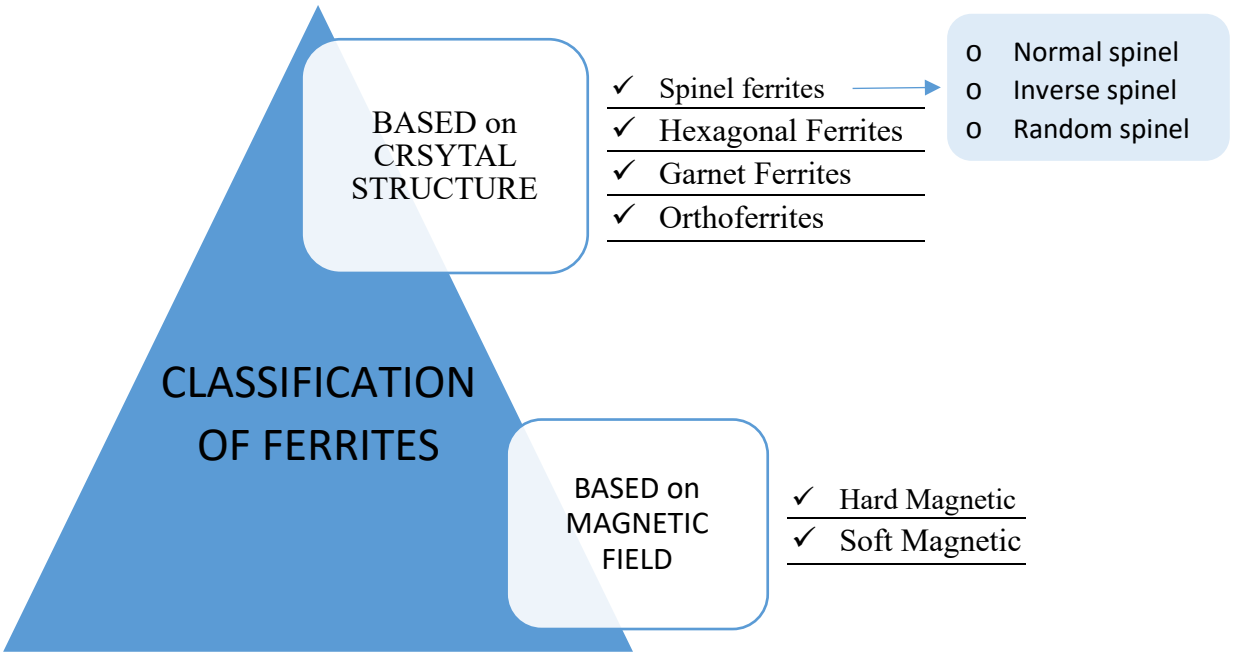

Figure 1.12 Classification of Ferrites

1.10.1. Based on Crystal Structure:

1.10.1.1. Spinal Ferrites:

Spinel ferrites are a type of magnetic materials with the general formula MFe_2O_4, where M denotes divalent metal ions such as Ni, Zn, Cu, Cd, Co, Mg, and Mn. When compared to metallic magnets, these ferrites perform more magnetically and have intriguing qualities like high electrical resistance, low magnetic losses, and improved magnetic performance [41]. Spinel ferrites can also be modified by substituting trivalent ions like Al, Cr, and Ga in place of Fe^{+3}. The two most popular types of spinel ferrite are nickel-zinc ferrites and manganese-zinc ferrites, both of which have high magnetic permeability and may be altered to have a variety of intrinsic properties. [42]. The cubic crystal structure of spinel ferrites comprises a close-packed oxygen anion arrangement with tetrahedral and octahedral coordination sites. When sharing only one edge, the ionic locations in

the octants are the same; however, when sharing a face, they are different. Four oxygen ions are present in each octant, which are all arranged along the body diagonals as depicted in figure 1.13.

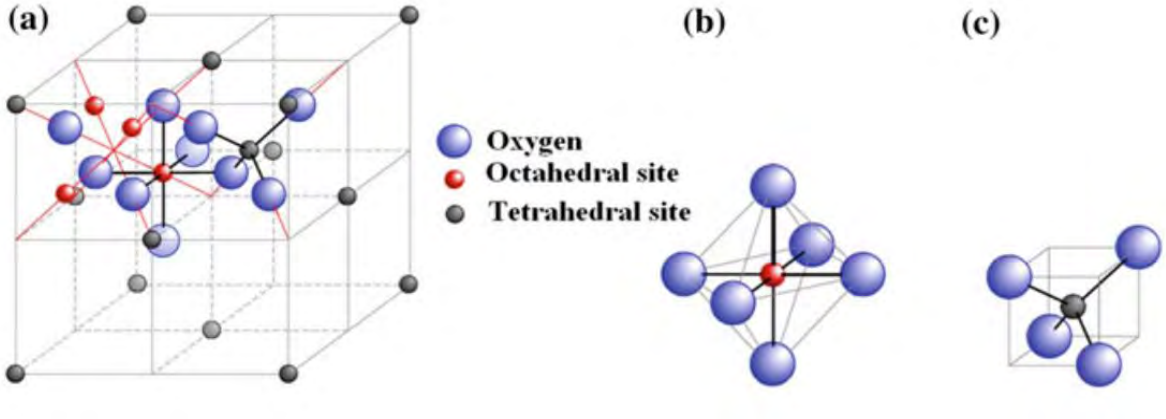

Figure 1.13 a) Spinel Ferrite Unit Cell Structure, b) Octahedral Interstice, and c) Tetrahedral Interstice

Based on the arrangement of cations in the octahedral site (B) and tetrahedral site (A), there are three different types of spinel ferrites: [43]

- **Normal spinel ferrites** are characterized by the arrangement where divalent metal ions are situated at the tetrahedral (A) site, while two trivalent Fe^{3+} ions occupy the octahedral (B) site. Examples include zinc ferrite ($ZnFe_2O_4$) and cadmium ferrite ($CdFe_2O_4$).
- **Inverse spinel ferrites** are distinguished by the presence of a single trivalent Fe^{3+} ion occupying the tetrahedral (A) site, while the remaining trivalent Fe^{3+} ions and divalent metal ions are situated at the octahedral (B) site. Examples include ferric oxide (Fe_3O_4), nickel ferrite ($NiFe_2O_4$), and cobalt ferrite ($CoFe_2O_4$) [44].
- **Random spinel ferrites** exhibit a distribution of both divalent metal ions and trivalent Fe^{3+} ions across both the tetrahedral (A) and octahedral (B) sites. An illustration of this type is copper ferrite ($CuFe_2O_4$). The arrangement of cations in random spinel ferrites is influenced by various factors, including ionic radii, electronic configuration, and the electrostatic energy of the lattice. [45, 46].

1.10.1.2. Hexagonal Ferrites:

Hexagonal ferrites, also known as rhombohedral ferromagnetic oxides, were first identified in 1952 and 1956. They are denoted by an $MFe_{12}O_{19}$ formula, where M is one of the elememts

barium, strontium, calcium, or lead. Hexaferrites are valuable as hard magnets because of their closed-packed hexagonal crystal structure, strong coercivity, and permanent magnet characteristics. These materials find utility across diverse applications, including magnetic recording, data storage materials, and electrical devices operating at microwave/GHz frequencies. Hexaferrites are classified into six subclasses based on the M and Me ions present. Recently, their potential has been explored for unique applications, such as electronic components for mobile and wireless communication, electromagnetic wave absorbers, as well as various types of electromagnetic interference filters and sensors. Additionally, hexaferrites are employed in common mode chokes, spike suppression and gate drive transformers, and flat cable beads, among other uses. Their applications extend to computers and peripherals, communication systems, automobiles, and power supplies. [47-49].

1.10.1.3. Garnet Ferrites:

Garnets are minerals with the general formula $X_3Fe_5O_{12}$, two magnetic ions are present typically iron and rare earth element such as Sm, Dy, Gd, Tb, Eu, Er, Y, Lu, and Tm. These ferrites exhibit a complex crystal structure with dodecahedral (12-coordinated), tetrahedral and octahedral sites that possess magnetic hardness. Tetrahedral and octahedral site interactions are antiparallel, and the net magnetic moment is antiparallel to the rare earth ions on the 'c' sites. The garnet structure, which has 160 ions in the unit cell, is one of the most intricate crystal structures and challenging to depict in two dimensions. For use in different domains, including memory devices, garnet-based nanoferrites are being widely explored. [50].

1.10.1.4. Orthoferrites:

Orthoferrites are materials characterized by the general formula $MFeO_3$, where M represents one or more rare earth elements. These substances possess an orthorhombic crystal structure and exhibit weak ferromagnetic properties. Examples of orthoferrites are $PrFeO_3$, $LaFeO_3$, and $DyFeO_3$, which have various applications such as sensors of magnetic fields, catalysts, electrical circuits, spin valves, and optical Internet. The perovskite structure of orthoferrites consists of large divalent or trivalent ions (A) occupying the corners of a cube, small trivalent or tetravalent metal ions (B) situated at the center of the cube, and oxygen ions positioned centrally on the faces of the cube [51]. Crystal structure of orthoferrite is illustrated in figure 1.14.

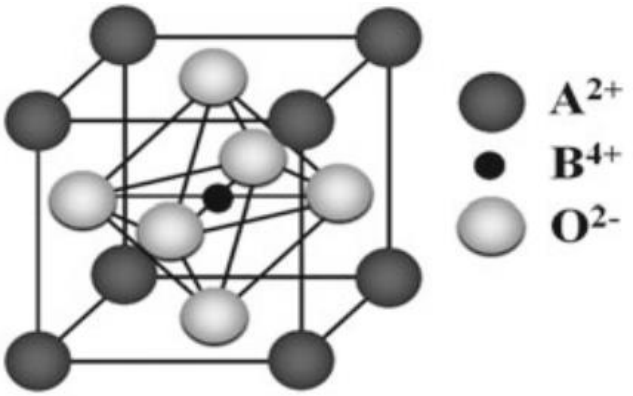

Figure 1.14 Structure of Orthoferrite [40]

- **Soft ferrites**

  Soft ferrite is a type of magnetic material that only exhibits ferromagnetism when magnetic field is applied. It is commonly used in electronics and various industrial applications. In television, telecommunications, military equipment and space research, manganese-zinc ferrite, a type of soft ferrite, is employed as a soft magnet that operates at high frequencies. [40].

- **Hard ferrites**

  Iron oxide and barium or strontium oxide are the two magnetic constituents of hard ferrites, which are utilised to make ceramic magnets. They can build permanent ferrite magnets and exhibit ferromagnetism without an external field. Hard ferrites are inexpensive, have a higher coercivity and remanence after magnetization, and can hold stronger magnetic fields.. They are used in various industries such as telecommunications, electronics, and household products like refrigerator magnets. Both $BaO\text{-}6Fe_2O_3$ and $SRO\text{-}6Fe_2O_3$ have the hexagonal ferrite structure, however Sr-M hexaferrite has somewhat superior magnetic properties. [40].

1.11. Poly (vinylidene fluoride):

Poly (vinylidene fluoride) (PVDF) is a polymer known for its characteristic of being semi-crystalline in nature and desirable ferroelectric and piezoelectric properties, making it a sought-after material for many researchers. Its exceptional chemical and thermal stability, mechanical

properties, and high piezo and pyro coefficients make it suitable for numerous applications, including transducers, detectors, memory devices, and biomedicine [52].

PVDF's crystallinity can vary from 35-70% based on its processing conditions, and it comprises repeating units of doubly fluorinated ethane, CH_2-CF_2, with a dipole moment of $7 \times 10^{-30}\ cm$ per unit. Commercial PVDF exhibits a density range of 1.75 to 1.78 gcm^{-3}, while melt PVDF homopolymer has a density range of 1.45 to 1.48 gcm^{-3} at 230 ºC and 1.0 bar [53]. PVDF homopolymers have a 59.4% fluorine content and 3% hydrogen content and are typically synthesized through free radical polymerization of CH_2 = CF_2 [54]. The orientation of the molecular segments around the carbon backbone is described as a trans bond (t) when the angle between them is 180º, or a gauch bond (+g/-g) when the angle is ± 60º. PVDF's ferroelectric and piezoelectric characteristics are largely influenced by its structural composition, which can take on four primary forms: alpha (α), beta (β), gamma (γ), and delta (δ) phases.

1.11.1. Alpha Phase:

The most frequently noticed PVDF phase is the alpha phase, and it is kinetically favored [53]. It has a monoclinic crystal structure [55], with chains arranged in TGTG' configurations. This arrangement causes the dipole moments to cancel out each other, resulting in a nonpolar phase [56]. The alpha phase can be achieved by slow cooling of films after annealing [57]. The lattice parameters for the alpha phase are a = 4.96 Å, b = 9.64 Å and c = 4.62 Å as shown in figure 1.15. [53]. Stretching can change it into the beta phase, while thermal treatments can change it into the gamma phase, and the Delta phase by poling at high fields as shown in figure 1.16 [58].

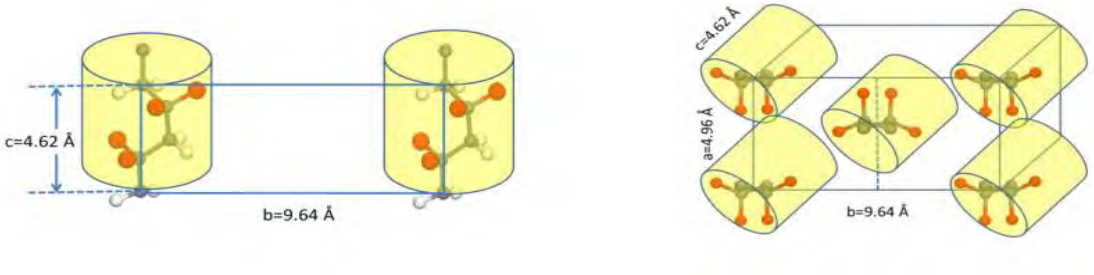

Figure 1.15 Chain Conformation and Crystal Cell of PVDF during α-Phase [53]

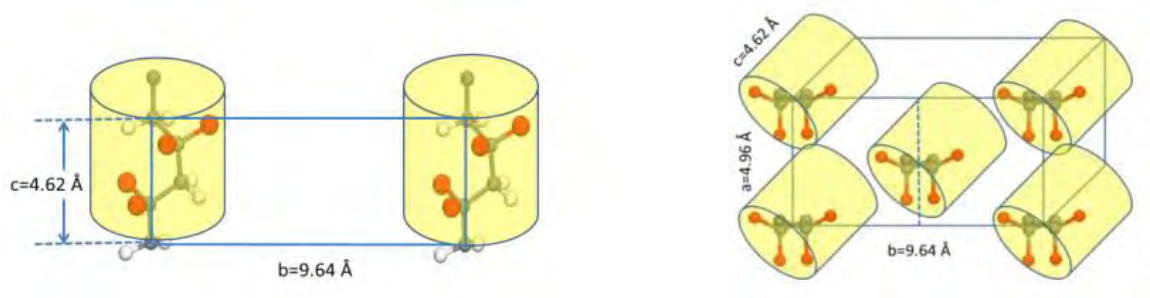

Figure 1.16 Chain Conformation and Crystal Cell of PVDF during δ-Phase [53]

1.11.2. Beta Phase:

The *β*-phase of PVDF is characterized by a TTTT chain conformation and has lattice parameters of a = 8.58 Å, b = 4.91 Å and c = 2.56 Å as depicted in figure 1.17. It is a member of the Cm2m space group and has an orthorhombic structure. In this phase, the dipoles within the polymer chain align uniformly in a perpendicular direction to the carbon backbone axis. This results in the *β*-phase exhibiting the highest polarization and having significant ferroelectric and piezoelectric properties [59, 60]. Moreover, the *β*-phase of PVDF is regarded as the phase with the highest level of thermodynamic stability among its various phases. To obtain the *β*-phase, one can stretch and pole *α* and *γ*-phase samples at high electric fields. Other methods to convert *α*-phase to *β*-phase include solid-state drawing, cold drawing, high-temperature annealing, and the use of PVDF nanocomposites [61, 62].

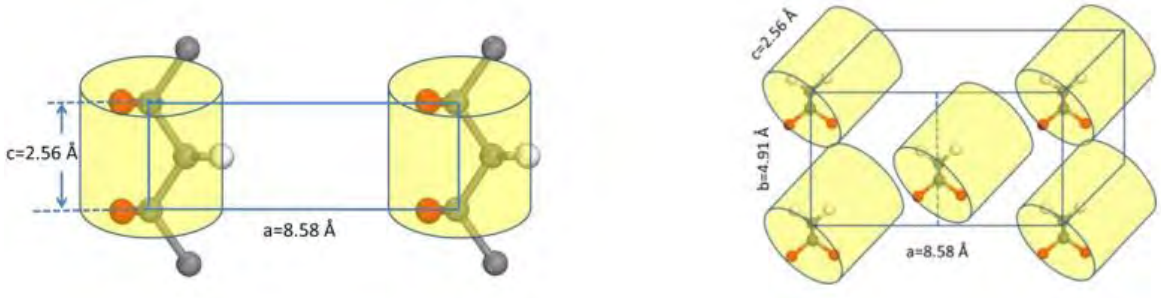

Figure 1.17 Chain Conformation and Crystal Cell of PVDF during *β*-Phase [53]

1.11.3. Gamma phase:

PVDF in *γ*-phase exhibits a monoclinic crystal structure and has TTTG+TTTG' chain conformation [53]. It belongs to the C121 space group and has lattice parameters of a = 4.97 Å, b

= 9.66 Å, and c = 9.18 Å as shown in figure 1.18. This phase can be obtained via procedures like high-temperature annealing or the low-temperature evaporation of polar solvents. [63]. While γ-phase is ferroelectric, it is less polar than β-phase. The non-polar version of γ-phase is known as ε-phase shown in figure 1.19 [64].

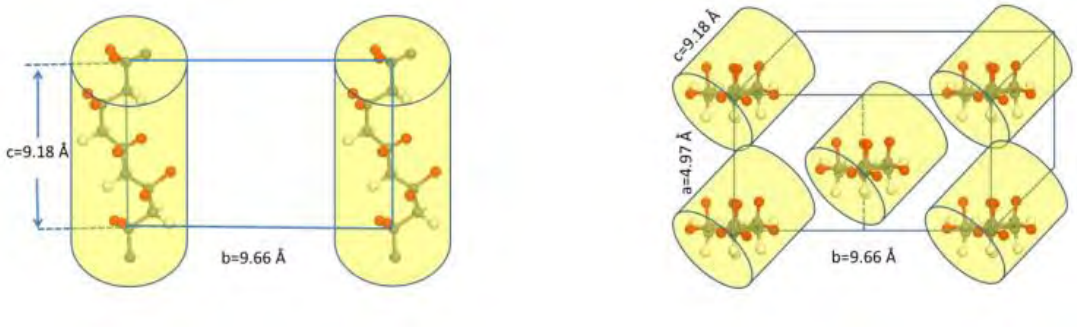

Figure 1.18 Chain Conformation and Crystal Cell of PVDF during γ-phase [53]

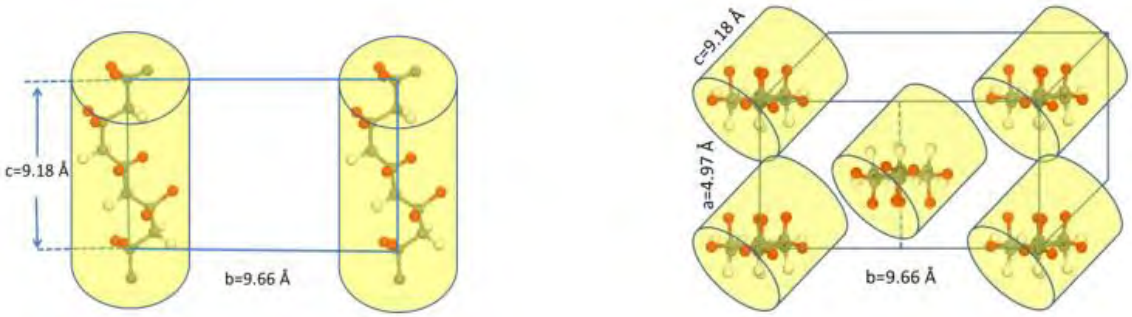

Figure 1.19 Chain Conformation and Crystal Cell of PVDF during ε-phase [53]

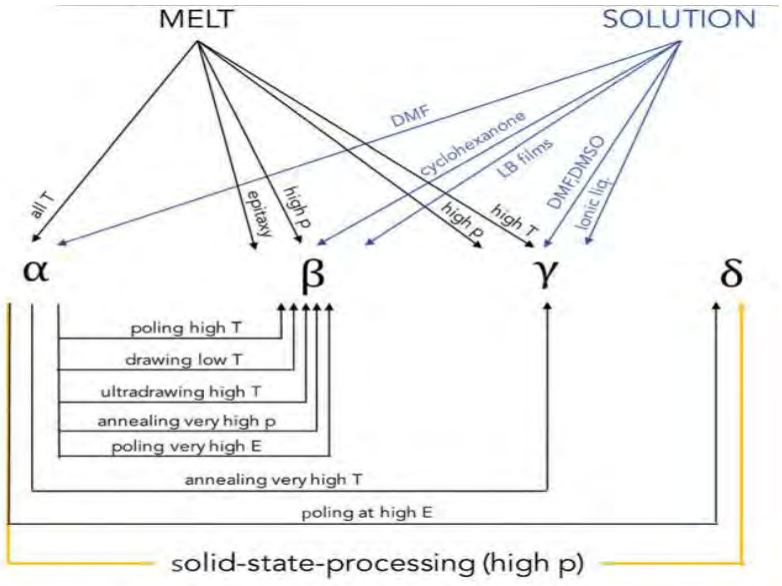

Figure 1.20 Processing Routes of PVDF towards Each Phase [65]

1.12. Contribution of Defects to Ferroelectricity in PVDF:

PVDF is a polymer that has a perfect structure with hydrogen atoms bonded only to carbon atoms that are further bonded to fluorine atoms. However, there are two different types of structural defects caused by certain monomers becoming reversed during the synthesis of PVDF: Head-to-Head (HH) and Tail-to-Tail (TT) defects shown in figure 1.21. These defects exist in pairs and produce steric hindrance between the fluorine atoms of neighboring chains, which raises the energy of the system. The defect density of commercially available PVDF is around 4-5%, and this density strongly affects the crystal structure of PVDF. The energy of the alpha phase is less than the beta phase, if the defect density is lower than 10%, and if the defect density is greater than 10%, the beta phase is favored due to its lower energy. The steric hindrance produced by HHTT defects increases the energy of the system, making the alpha phase unfavorable. However, beta phase can tolerate incoming HHTT defects more as compared to the alpha phase. If the defect density is greater than 12%, then the lowest possible energy will be of the beta phase, which results in the occurrence of ferroelectricity in PVDF [66].

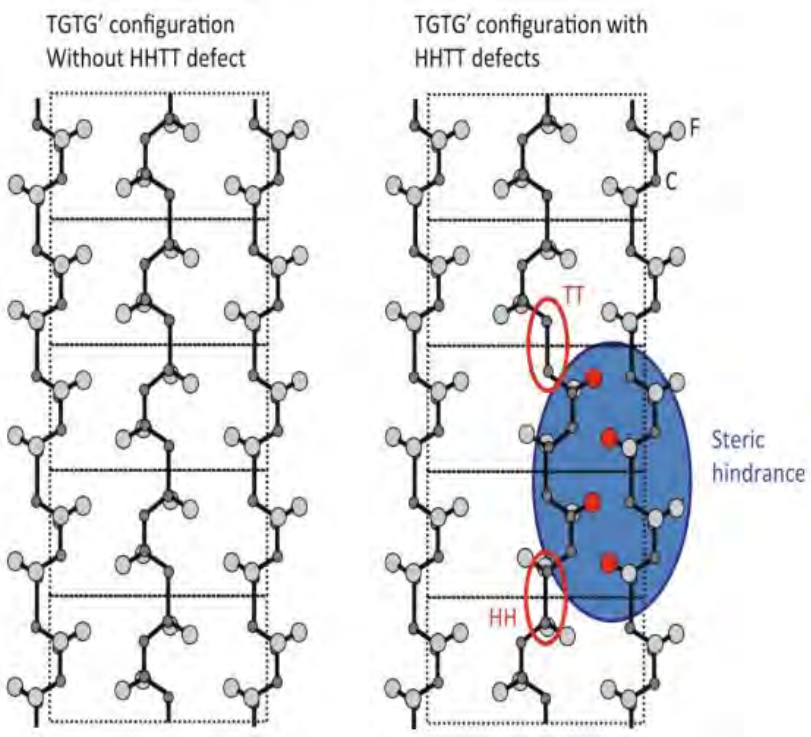

Figure 1.21 Crystal Structure with the Defects Configuration [66]

1.13. Poly (vinylidene fluoride-trifluoro ethylene):

Poly (vinylidene fluoride-trifluoro ethylene) P(VDF-TrFE) is a semi-crystalline random copolymer composed of VDF and TrFE monomers. At low temperatures, it possesses an orthorhombic structure (Cm2m) resembling PVDF, with slight expansion in lattice parameters. Conversely, at high temperatures, its chains exhibit a hexagonal structure (6/mmm). Interestingly, with a molar percentage ranging between 20-35%, it can induce β-phase transformation, regardless of post-treatment, while also enabling the increase of crystallinity up to 90% [58].

PVDF and its copolymers with TrFE exhibit high remnant polarization and piezoelectric efficiency, with TrFE content ranging from 90/10 to 70/30 being the most suitable for achieving ferroelectric properties. However, increasing the TrFE content beyond this range may result in a decrease in ferroelectric properties due to a decrease in crystallite size [66]. The addition of TrFE monomers to PVDF induces steric hindrance, which has a significant destabilizing effect on the alpha phase structure. However, this steric hindrance has negligible effect on the beta phase of PVDF as shown in figure 1.23. Therefore, the addition of TrFE monomers provides phase control of PVDF from alpha to beta phase.

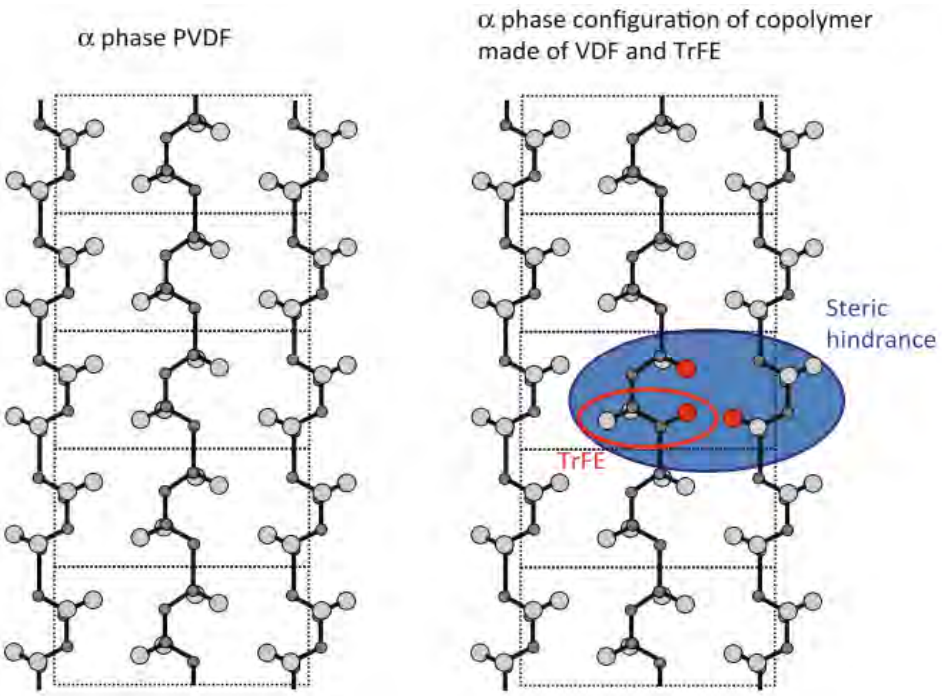

Figure 1.22 The α-phase Configuration of the Copolymer Made of VDF and TrFE [66]

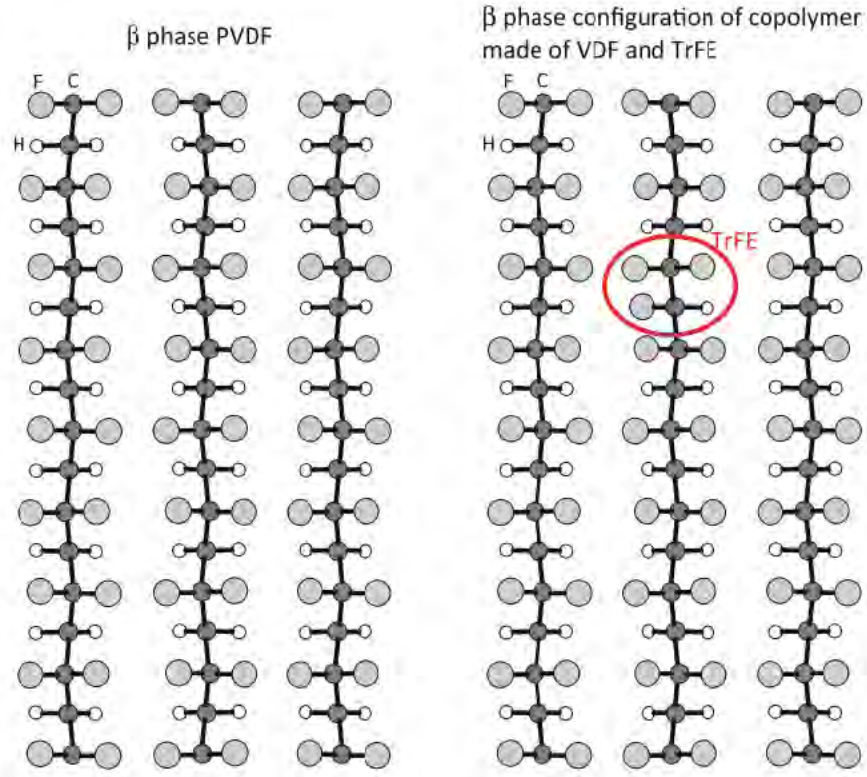

Figure 1.23 No Serious Steric Hindrance in β-Conformation of P(VDF-TrFE) [66]

1.14. Cobalt Ferrite ($CoFe_2O_4$):

Ferrite magnetic materials have drawn a lot of attention in a variety of disciplines because of its great dielectric and magnetic properties, high electrical resistivity, excellent mechanical hardmess, and comparatively inexpensive cost. [67, 68]. Among them, cobalt ferrite ($CoFe_2O_4$ or CFO) is of particular interest due to its unique properties, such as piezo-magnetic [69], its coercivity is high, crystalline anisotropy is strong, magnetism is modest (80 emu/g), and the Curie temperature is high (520 ºC) [70]. Its versatility makes it appropriate for a variety of applications, including batteries made of lithium ion [70], a high level of data storage [70], magnetic tape [71], magnetic fluids [70], magnetic medication delivery [72], catalytic [73], biological sensors [74], and hypothermia [75].

CFO has a semi-hard nature and is member of the space group Fd3m, with lattice parameter a = 8.38 Å. It is a ferrimagnet with a Neel temperature of 800 K [76]. The magnetic properties of $CoFe_2O_4$ are mainly due to the tetrahedral and octahedral sites.

1.14.1. Crystal Structure of CFO:

Cobalt ferrites are characterized by their chemical formula $CoFe_2O_4$ and an inverse spinel structure. Each unit cell in $CoFe_2O_4$ spinel structure has 56 ions, with larger oxygen ions arranged in a dense Face Center Cubic (FCC) pattern. These oxygen ions are separated by smaller cobalt ions, which are divided into two types. The first type, also called the A-site or tetrahedral, is positioned at the center of a tetrahedral-shaped structure, where the oxygen ions are situated at the corner points. The second type, called the octahedral or B-site, consists of cobalt ions surrounded by oxygen ions in an octahedral arrangement [69]. Structure of CFO particles is depicted in the figure 1.24.

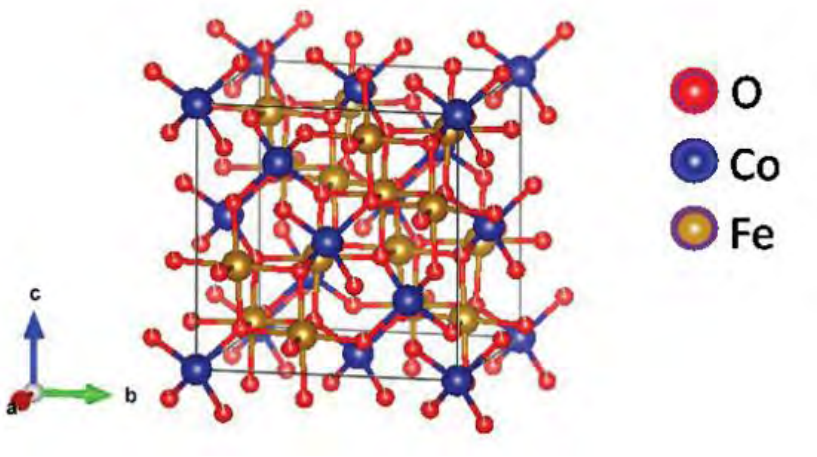

Figure 1.24 Structure of Cobalt Ferrite [69]

1.15. Multiferrioc:

Multiferroics are the materials that have the existence of at least two ferroic orders together in a single phase [77]. Ferroic orders include (anti) ferromagnetism, (anti) ferroelectricity, (anti) ferroelasticity. Ferromagnetism refers to the capability of magnetization to be altered by an external magnetic field, while ferroelectricity is the ability of electric polarization to be modified by an applied Electric field. Ferroelasticity signifies the distortion that can be adjusted by an imposed force. Hans Schmid was the first person to introduce the term "multiferroic" during a conference in Ascona back in 1993, as an extension to the earlier categorization of ferroic materials by Aizu [78]. Now the term is used as the coexistence of these properties in multiphase materials as well. The specialty of multiferroics is not limited to the fact that they display multi-order states but more important is the cross-coupling effects which can occur between different ferroic orders. The coexistence and coupling of ferroelastic property and ferroelectric property are termed as piezoelectric property and the materials are known as piezoelectric materials. For ferroelastic and ferromagnetic, it is known as magnetostrictive and the coupling of ferroelectric order and ferromagnetic order is called magnetoelectric property. After the introduction of these materials, multiferroic materials have been researched to study solid-state physics and attracted the attention of scientists and researchers to explore them in spintronics [79], sensors [80] and data storage field [81] etc.

1.17. Types of Multiferriocs:

1.17.1. Single-Phase Multiferriocs:

Single phase materials refer to homogenous material that has multiphase (magnetic and electric) coexisting at any point within a single material. They are chemically isotropic. There are two classifications for single phase multiferroic materials, which are as follows. [81]:

- **Type 1:**

  Type 1 single-phase materials are those materials in which electrical ordered phase and magnetic ordered phase coexist within the same material and are independent of each other, and the microscopic origins of both the phases are different.

- **Type 2:**

  Type 2 single-phase multiferroic materials are characterized by the coexistence of electric and magnetic ordered phases within a homogeneous material and ferroelectricity is induced due to magnetism so the origin is dependent. This type of multiferroics has a very strong coupling between its phases i.e., magnetoelectric coupling.

1.17.2. Limitation of Single-Phase Multiferriocs:

The coupling between the ferroelectric and ferromagnetic order parameters in many single-phase multiferroics is often weak, resulting in limited influence of one property on the other. This weak coupling poses challenges in efficiently controlling and manipulating the multiferroic properties [82]. Furthermore, The manifestation of multiferroic behavior in single-phase multiferroics is commonly restricted to low temperatures. At elevated temperatures, the interaction between the ferroelectric and ferromagnetic order parameters may weaken or vanish, thereby restricting their practical applications to temperatures below room temperature [82, 83].

1.17.3. Composite Multiferriocs:

Material having multiphase and show multiferroic properties are known as composite multiferroic. In 1961, ME coupling in single-phase material was firstly observed, subsequently in polymer crystalline single-phase material, and the largest value for magnetoelectric (ME) coupling was 20 $mVcm^{-1}Oe^{-1}$ for Cr_2O_3 [84]. The ME effect in a single phase is although has some value but it is very small that It cannot be useful at high temperature and applications. The fundamental issue is that polarization and magnetization favoring electrical configurations are incompatible

with one another. Since the interchange between the spin and polar subsystems in single-phase ME materials is typically relatively weak, these materials are frequently antiferromagnetic.

Now the alternative option for the multiferriocs/ME effect with high value is to turn towards multiphase / composites materials. Composite multiferroics exhibit a distinctive feature where the ordered phases within the material are physically segregated from each other. This has been done by Philips for the first time [84, 85], but he did not achieve the high/enhanced value for the ME coupling. ME coupling with high value can be achieved by using magnetostrictive and piezoelectric layers or piezoelectric and ferrites layers place over each other. So basically, the mechanical action between the two layers results in the ME effects. (Magnetic force produce stress and strain in magnetostrictive material and that force produce electric polarization in piezoelectric material that is combined by the layer) Thus, only the end result of the two phases can exhibit magnetoelectricity, not the individual layer. It is the magneto-elastic-electric effect [84].

1.17.3.1. Connectivity:

In composite, multiferrioc property of material strongly depend upon the synthesis of the material i.e., fabrication of the composites. In a single-phase, breaking of spatial and time-reversal symmetry limited their multiferroic properties. However, the symmetry criteria is automatically satisfied in composite multiferroic materials for any combination in any conceivable geometry. Figure 1.25 shows various composite multiferroic geometries and their geometries-based classification.

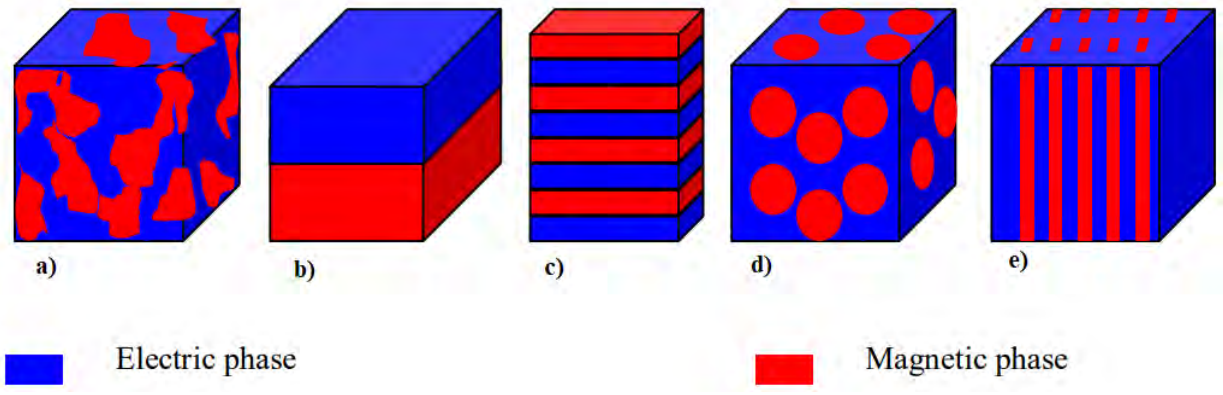

Figure 1.25 a) Uniform combination of the electric and magnetic phases; b) Bi-layer laminated structure; c) Multilayer laminated structure; d) Composite consisting of a matrix and many constituent parts; e) Composite multiferroic fiber [81]

There are three basic connectivities as show in figure 1.25;

- 2-2 (laminated / bi layer) [86]
- 1-3 [87]
- 0-3 [88]

Where 1, 2, and 3 indicate the dimension of material e.g., 2-dimension layer on 2-dimension layer, rod (1-D) in the 3-dimensional cube, a particle (0-D) embedded in 3-dimension cube. The 2-2 laminated structure will give good multiferroic properties and infect the highest among all [81]. Following table show some of single phase and composite multiferriocs.

Chapter 2 Techniques and Characterization

In this chapter, different experimental techniques and characterization are studied for the samples (polymer films). The properties studied are structural, dielectric, and multiferroic properties. An overview of different techniques is presented below in the flow chart i.e. figure 2.1.

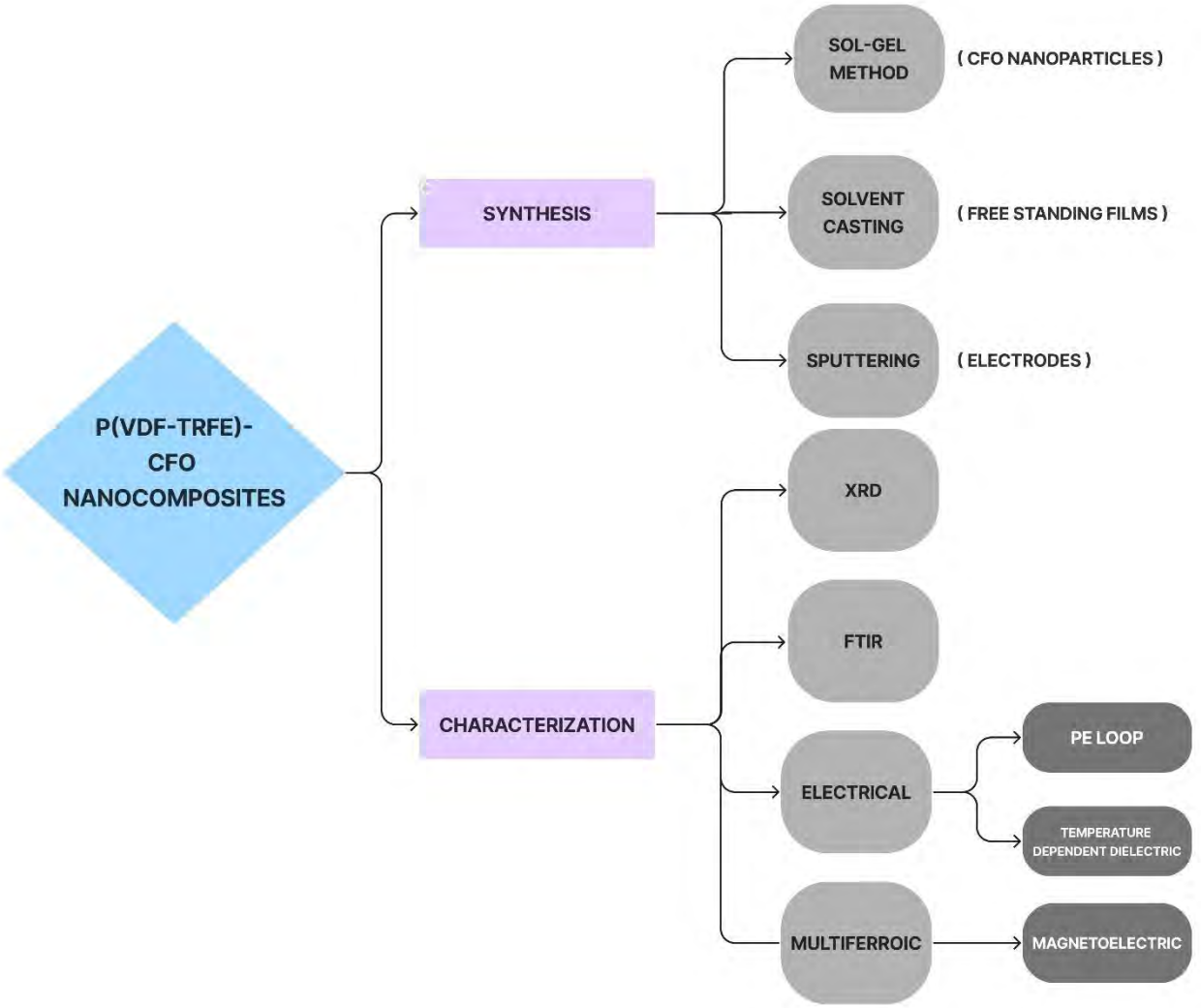

Figure 2.1 The Complete Set Up of Experimental Techniques.

The discussion will begin with exploring techniques followed by an examination of characterization.

2.1. Sol-Gel Method:

Sol-gel, mechanical alloying, vapor phase compression, electrochemical, and plasma methods are only a few of the current technologies used to create nanoparticles. However, the sol-gel method is among the most popular and commonly used of these due to its widespread use in industry for the creation of huge amounts of nanomaterial. [89-92].

Bottom up synthesis is accomplished via the sol-gel procedure. The sol-gel method transforms monomers into a colloidal solution (sol) that serves as a starting point for constructing a networked structure (or gel) of either discrete particles or network polymers by using metal alkoxides as precursors. This technique is commonly employed to manufacture ceramic nanoparticles e.g. Cobalt ferrite (CFO) etc.

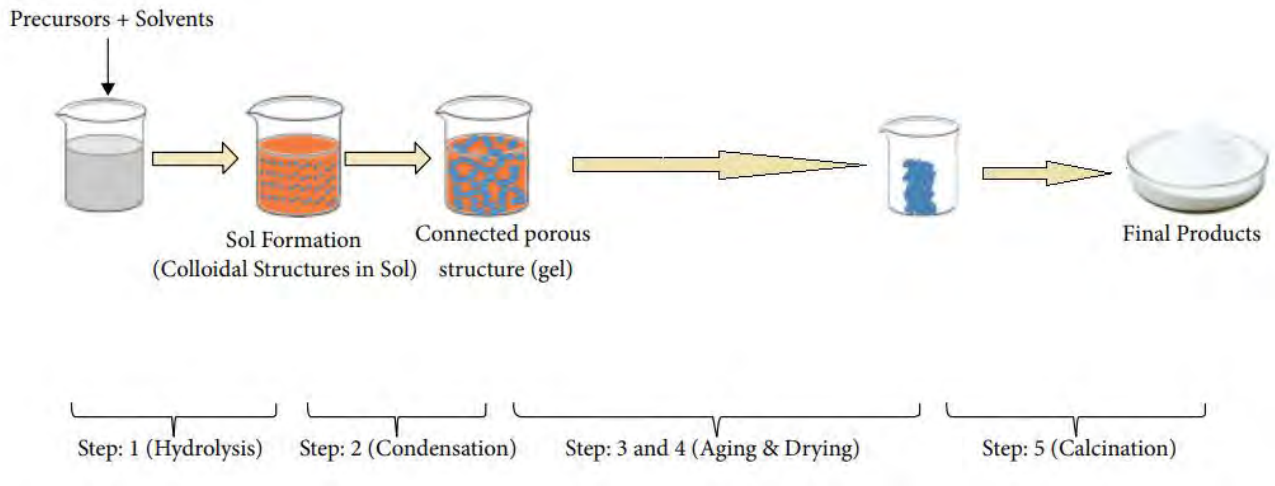

Figure 2.2 Schematic Diagram of Sol Gel Method [93]

Precursor are the materials used to start the sol gel process. Precursor should

- Capable of dissolving in the medium of the reaction.
- Be reactive enough to take part in gel formation [94].

The transition of sol to gel in the sol-gel process typically involves altering the pH or solution concentration [95-97]. This technique offers several benefits, such as achieving a uniform nanostructure, narrow particle size distribution, and high product purity at low temperatures. Metal nano oxides can be synthesized using this method [98, 99]. Various methods, mostly involving gentle drying to eliminate the solvent, can be used to transition from sol to gel. In the present work

CFO nano particles are synthesized through sol gel method. There are several different instruments that were used for the process like mortar and piston for fine grinding, oven for drying and tube furnace for annealing. Two of the instruments explained below.

2.1.2. Mortar and Piston:

A laboratory instrument consists of two tools used to prepare different particle like nanoparticles grinding and crushing them into powder of nano-sized. The mortar is basically a bowl made of hard material e.g. ceramic, metal, granite etc. however the second component called pestle which is used to press the substance placed in mortar. The substance has to be wet during grinding. The liquid used to wet the specimen is called the mixing agent. Usually acetone is used as a mixing agent. Grinding is used to reduce the particles size and particles of different precursor become in contact with each other. This is the most important and essential step because at contact points, reaction may occur. The key advantage of the mortar and pestle is that it had deeper bowl to confine the material to be crushed without the waste and spillage that occur with flat grinding stones. It is used for synthesis of CFO nanoparticles.

Figure 2.3 Agate Mortar and Pestle

2.1.2. Tube Furnace:

Inorganic and organic molecules can both be synthesized and purified using tube furnaces, which are electric heating equipment. It has a cylinder-shaped cavity with heating coils surrounding it, and the coils are wrapped in a thermal insulating substance. Thermocouples are

there to control the temperature. At room temperature, some particles do not react, so high temperature is used for solid state reaction. The range of tube furnace used in the laboratory has a temperature range of 0 ºC to 1000 ºC. The advantage of the tube furnace is its heating rate is fast and has a smaller volume capacity. Smaller samples can be easily handle by these furnaces.

Figure 2.4 Tube Furnace [100]

2.2. Solvent Casting:

Film extrusion generates films with better optical, mechanical, and physical qualities; a substitute approach is solvent casting. The procedure entails dissolving or dispersing the polymer in a solution, coating a substrate with it, and then drying to remove the solvent or water and leave behind a solid layer. To make a film that can be further laminated or coated to manufacture multi-layer products, this layer can be removed from the substrate.

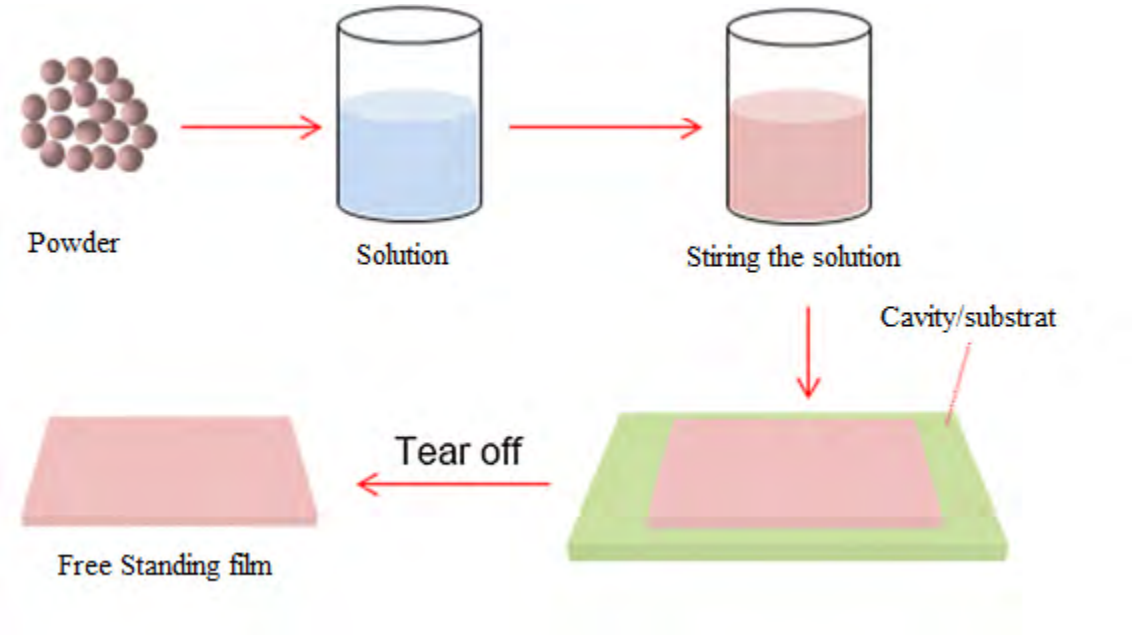

Figure 2.5 Schematic Diagram Of Solvent Casting [101]

Solvent casting offers several advantages over traditional film extrusion methods in the manufacturing process which include:

- • The capacity to process at low temperatures, making it appropriate for active compounds that are sensitive to temperature.
- It is capable of producing high-temperature resistant films from non-thermoplastic, soluble raw materials.
- The film's thickness and dimensional stability can be adjusted.
- With casting from aqueous or solvent-based solutions, this method allows for the production of multi-layer films in a single pass and provides a greater selection of material options.

2.3. Sputtering:

Sputtering is a process in which energetic ions mainly gas ions bombard on the target (solid state) and atoms are ejected from target and transform them into the gas phase. It is commonly known as sputter deposition, which is a coating technique that uses high vacuum and belongs to the family of Physical Vapor Deposition (PVD) processes. The basic diagram of sputter coater is given below.

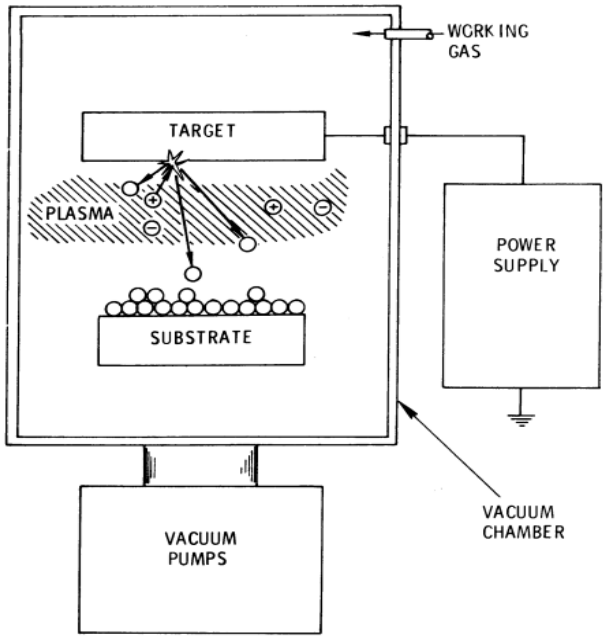

Figure 2.6 Basic Illustration of Sputtering Technique [102]

To deposit a target material onto a substrate, a sputtering process is used. However, the presence of airborne particles can impede this process, so a vacuum is created within the chamber using a vacuum pump. Then, an inert gas (argon) is backfilled into the chamber, and plasma is generated by applying an electrical potential to the gas, causing electrons to be knocked out of the argon atoms. As a result, argon becomes positively ionized and flows in the direction of the negatively charged target material (e.g. gold). This results in positively ionized argon, which moves towards the negatively charged target material (in our case, gold). As the ionized gas hits the target material, it dislodges particles from its surface, which fall onto the substrate, creating a film. To carry out this process, we used a GSL-1100X-SPC-12 Compact Plasma Sputter Coater, which has a vacuum chamber, a gold target, a needle valve for gas flow control, and a timer and display for adjusting the sputtering duration and viewing the vacuum and current settings. The coater can achieve a medium vacuum range up to 0.001 torr, and sputtering can be adjusted from 0 to 110 seconds.

Figure 2.7 GSL-1100X-SPC-12 Compact Plasma Sputter Coater [103]

2.4. X-Rays Diffraction:

A modern technique which is used to see the atomic spacing and molecular structure of the material is known as X-ray diffraction (XRD). Albert Wallace Hull discovered the XRD technique in 1880-1966. XRD is also used to determine the stress, defect, phase composition, crystallite size and lattice parameters. XRD arises from the constructive interference of monochromatic X-rays with a crystalline sample. The generation of X-rays is achieved using a Cathode Ray Tube (CRT), which produces a broad spectrum of radiation. To obtain monochromatic radiation, the X-rays are filtered and then directed towards the sample. A part of it called diffractometer is used to detect and determine the crystal structure. Each material has its own specific pattern and is independent of the each other. It is also known as fingerprint of a material [104].

2.4.1. Working Principle:

X-ray diffraction operates based on Bragg's law, which is formulated as follows.

$$n\lambda = 2dsin\theta \qquad 0.1$$

Where d, θ, n, and λ represent the atomic plane spacing, incidence angle, positive integer and the incident X-ray beam's wavelength respectively. This law connects the X-ray wavelength to the diffraction angle and lattice spacing. The atoms in the crystal are arranged in an ordered way, with lattice spacing d. as interplanar spacing comparable to the wavelength of X-rays, so we used X-rays for this purpose. When an atom is exposed to X-rays, electrons absorb the energy of the X-

rays. Electrons have specific energy levels around the atom. In order to discharge the electrons, the energy collected by them must be reemitted as new X-rays with the same energy as the original. This condition is known as elastic scattering. In a crystal, atoms are arranged in several planes that are spaced apart by well-defined distance. The evenly spaced atoms in these atomic planes scatter the X-ray beam when it strikes them. The scattered photons can interface either constructively or destructively, depending on their path difference. Constructive interference occurs when the path difference is a wavelength integral multiple. The resulting peak is recorded. A detector converts the recorded X-ray signal into a count rate, this count rate is transferred to the computer and displayed as a specific pattern on the screen. The obtained pattern consists of peaks with different intensities at different angles. Crystal structure of material is determined by comparing this obtained pattern to known standard pattern. Now a days the application of X-ray diffraction technology view the pattern (fingerprint) of other different types of material such as powders, single crystal epitaxial thin film and even amorphous materials that are randomly orientated.

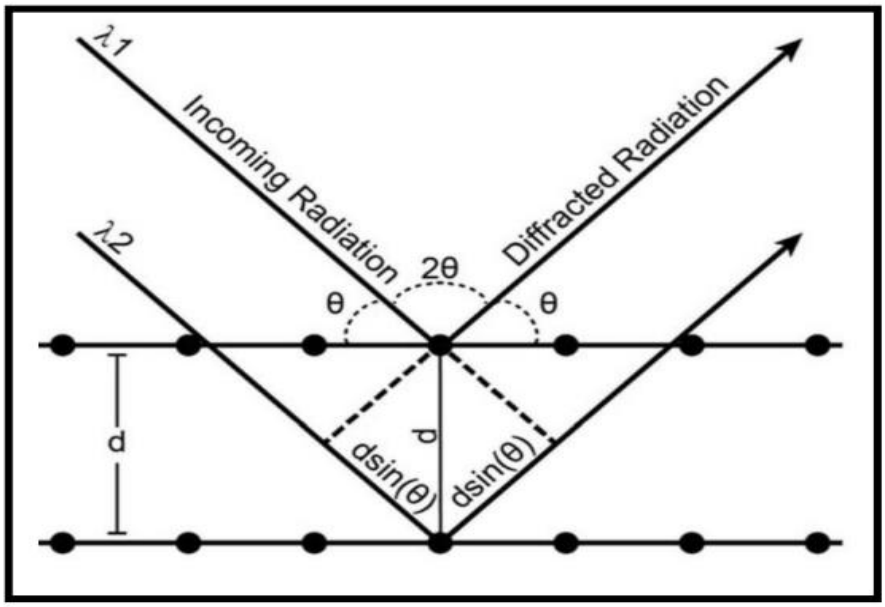

Figure 2.8 X-Ray Diffraction at Crystal Lattice [105]

For the structural analysis, the apparatus which is used for X-ray diffractometer known as a PAN analytical Empyrean system for structural characterization of samples. The instrument operates at 40 mA and 45 kV for current and voltage, respectively, and employs Cu as the X-ray source with characteristic wavelengths Cu - Kα of 0.15418 nm. The sample holder, which is

situated between the X-ray source and detector, is a flat glass slide. The X-ray beam generated from the source hits the specimen, and the detector on the opposite side records the reflected beam. The range of angle covered in our analysis was from 10º to 80º, with an increment of 0.02º and a stay time of 2 seconds.

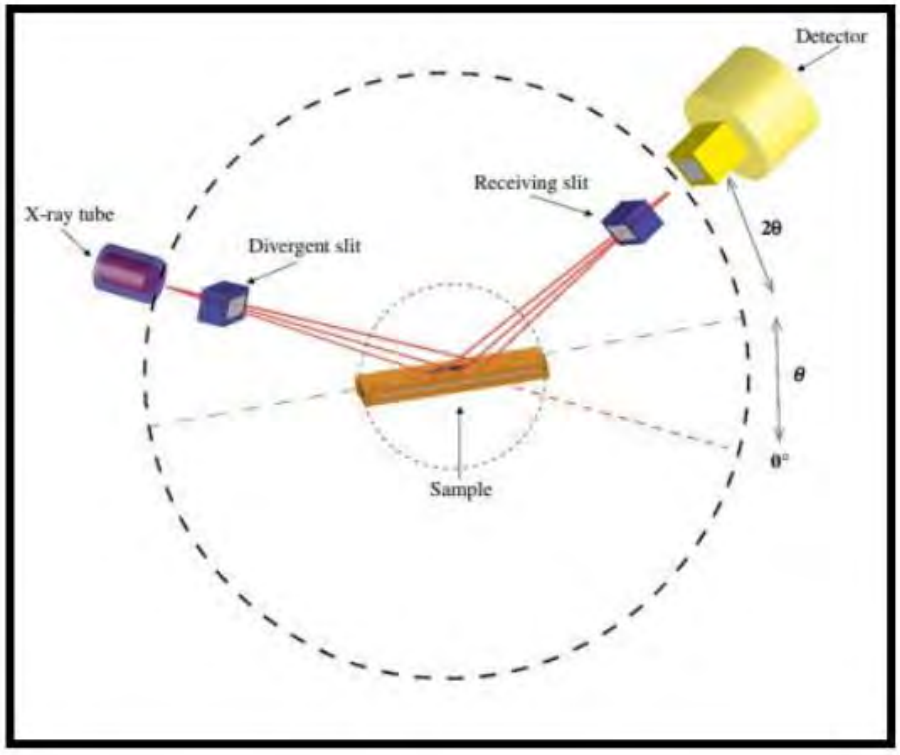

Figure 2.9 Bragg-Brentano Geometry of The Powder Sample Configuration [106]

The Bragg-Brentano geometry includes two types of slits for powder analysis. One is a fixed diverging slit (1º) on the incident beam side and the other is a series of slits (1/16º), placed at the focus of the diffracted beam. See figure 2.5.

The XRD setup that is used for our samples in the laboratory is illustrated in figure 2.10.

Figure 2.10 Setup of X-Ray Diffractometer Used In the Laboratory

2.5. Fourier Transform Infrared Spectroscopy:

Fourier Transform Infrared Spectroscopy (FTIR) is a technique that employs infrared (IR) radiation to identify the functional groups existing within materials. The technique measured the incorporation of IR radiation by each molecule bond, resulting in a spectrum showing transmittance (%) versus wave number cm^{-1}. To determine a molecule's functional group, it must be IR active, meaning that it possesses a dipole moment. The molecule absorbs energy when IR radiation interacts with covalent bonds, causing the adhesive to oscillate and vibrate. As a result, the molecule's net dipole moment changes, leading to absorption of infrared radiations. Symmetrical molecules with a single atom or a single bond do not absorb infrared radiations as they lack a net dipole moment. Since each bond has a distinct vibrational frequency, a particular infrared radiation frequency is absorbed, allowing for the identification of the functional group present.

Figure 2.11 Nicolet 5700 FTIR Spectrometer

2.5.1. Sample Preparation:

Preparing the sample is crucial for the analysis of Infrared spectra. Glass materials and plastics strongly absorb Infrared radiation, therefore, the sample holder or cell is made from ionic substances like KBr or NaCl. KBr plates are preferred over NaCl plates as they cover a wider range of 400 cm^{-1} - 4000 cm^{-1}. To prepare the sample, KBr powder is grind with acetone for 45-60 mins and compressed into pellets. The sample is placed between two pellets and inserted into the cell. Background spectrum is run to eliminate the interference caused by CO_2 and H_2O, which are present in the atmosphere. This background spectrum is subtracted from the compound spectrum for better clarity.

Table 2.1 Numerous Functional Groups Range in Wave Number (cm^{-1})

Range (cm^{-1})	Functional Groups
2500–3000	Carboxylic (O–H)
2260–2220	Nitrile (CN)
1750–1680	Ketone C = O
3500–3500	O = C – N – H stretch
1740–1690	Aldehyde C = O
3200–3550	O – H stretching

2.5.2. Working Principle of FTIR:

The principle behind infrared spectroscopies is that molecules absorb specific frequencies unique to their structure. By using a lionizing black body source, a beam of IR rays is emitted and controlled by an aperture before entering the detector. The beam then passes through the interferometer for spectral encoding and exits the interferometer as a signal. Once in the sample compartment, the beam interacts with the sample's surface, transferring and measuring the sample's distinctive frequencies. The detector captures the beam, producing a signal for final calculation. This signal is digitalized and processed through Fourier transformation on a computer. Figure 2.12 shows a schematic representation of a simple spectrometer configuration.

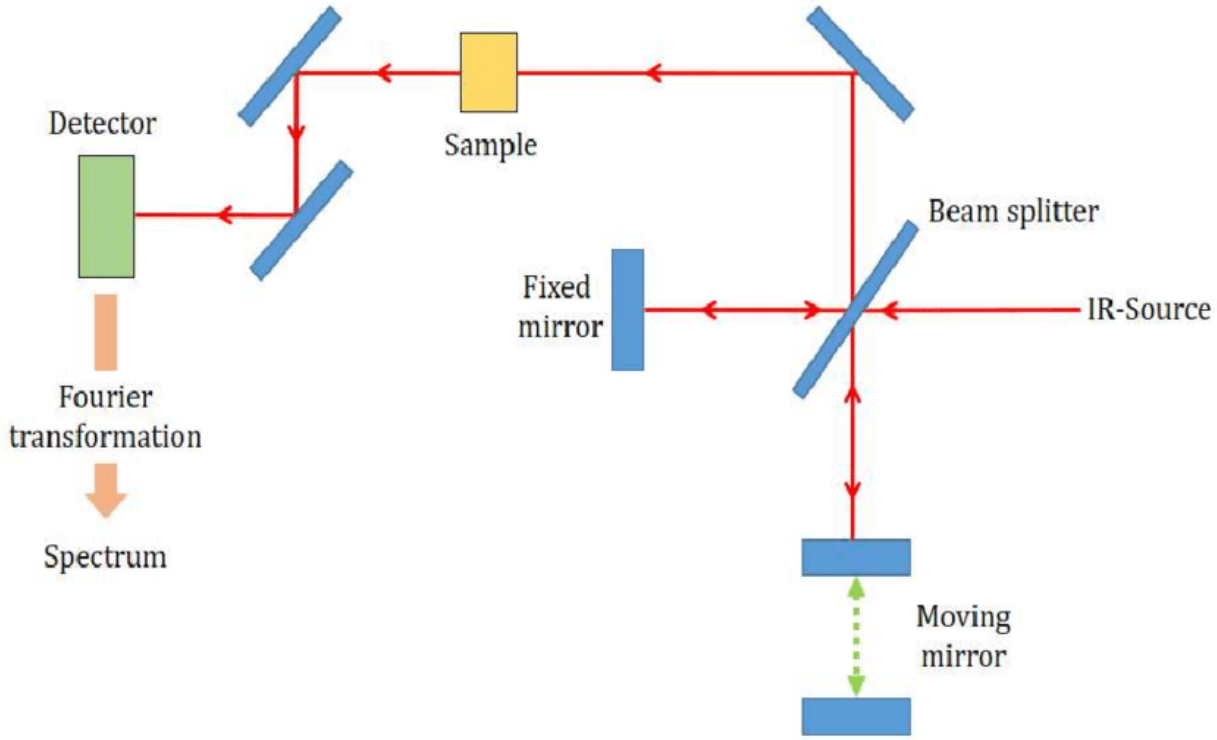

Figure 2.12 Simple Spectrometer Layout

2.6. Ferroelectric Characterizations:

A *P-E* loop is graphical representation of the induced polarization or charge (*P*) and the electric field (*E*) applied to device at a specific frequency. Understanding the *P-E* loop of simple linear devices can help comprehend the significance of this measurement. In an ideal linear capacitor, the *P-E* loop exhibits a straight line characteristic (as depicted in figure 2.13a), where

the slope of the line is directly proportional to the capacitance. This behavior arises due to the fact that in an ideal capacitor, the voltage lags 90º behind the current. Consequently, the charge, which is the integral of current over time, is in phase with the voltage. On the contrary, ideal resistors follow a different pattern where the *P-E* loop forms a circle centered at the origin (as shown in figure 2.13b). This circular behavior is observed because the current and voltage in ideal resistors are in phase. Combining these two components in parallel results in a *P-E* loop in figure 2.13c that represent the lossy capacitor with an area proportional to the dissipation factor and the slope proportional to the capacitance. For non-ideal devices such as nonlinear ferroelectrics, the *P-E* loop is more complex and differs from the linear ones as shown in figure. 2.13d.

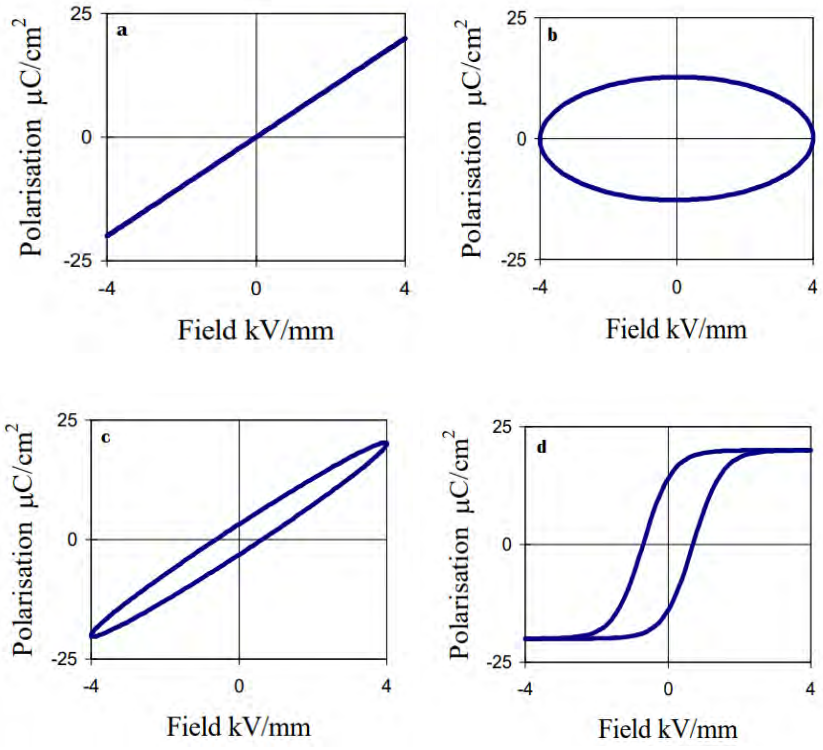

Figure 2.13 (a) Ideal response of a linear capacitor. (b) Response of Ideal Resistor. (c) Response of Lossy Capacitor (d) Ferroelectric Non-Linear Response [107]

The hysteresis property of certain materials, such as thin film ferroelectric memories, can be utilized in various applications, including defining drive parameters and investigating long and short-term performance through *P-E* loop measurements. Despite the fact that some parameters, such as P_S and E_c may imply that the field in hysteresis measurements must always be driven to saturation, valuable insights can also be gained from measurements at lower fields. Additionally,

the field need not stop at saturation and can be raised until breakdown occurs, allowing the study of breakdown behavior and the possibility of determining a pre-breakdown characteristic.

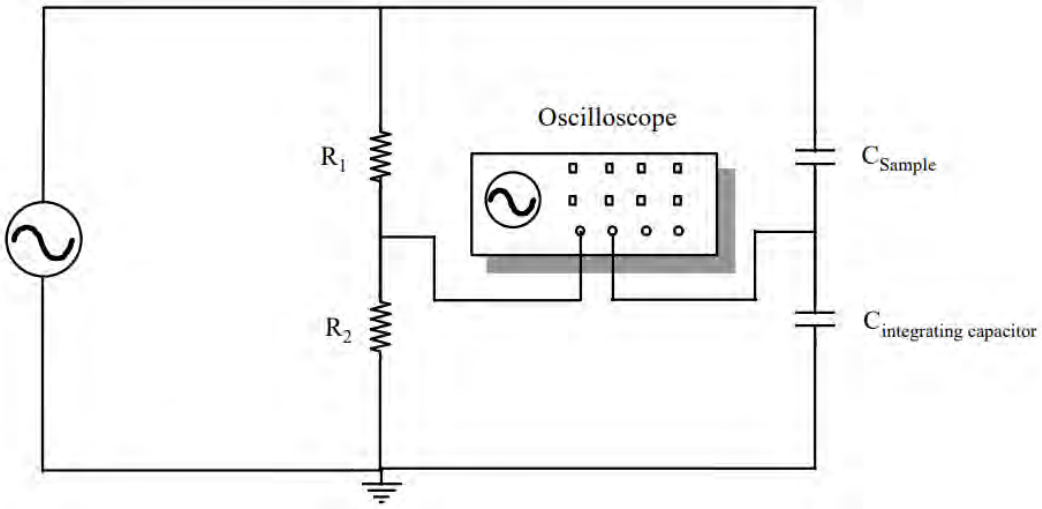

Figure 2.14 Illustration of the Sawyer Tower Circuit for P-E Loop Measurements [107]

2.6.1. Working:

The *P-E* loop setup work under the circuit diagram in the figure 2.14. The circuit consist of two capacitors connected in series, one of them is sample capacitor and the other is reference capacitor. A resistive divider attenuates the electrical field that is applied to the sample. The current is incorporated into the sample's charge by the reference capacitor, which is linked in series with it. To the oscilloscope's X and Y axes, these two voltages are fed, creating a *P-E* loop. Usually sinusoidal is applied. The form of the loop is dependent on the history of the material since the instantaneous value of polarization (P) is dependent on the amount of current and the applied electric field (E). In the present investigation, PolyK polarization loops and dielectric breakdown testing were used to quantify P-E. The device depicted in Figure 2.15.

Figure 2.15 PolyK test systems for dielectric breakdown and polarization loop

2.7. Temperature Dependent Dielectric Measurement:

Relative permittivity, often known as the dielectric constant, is the ratio of a material's permittivity ε to that of free space permittivity ε_o.

$$\varepsilon_r = \frac{\varepsilon}{\varepsilon_o} \qquad 0.2$$

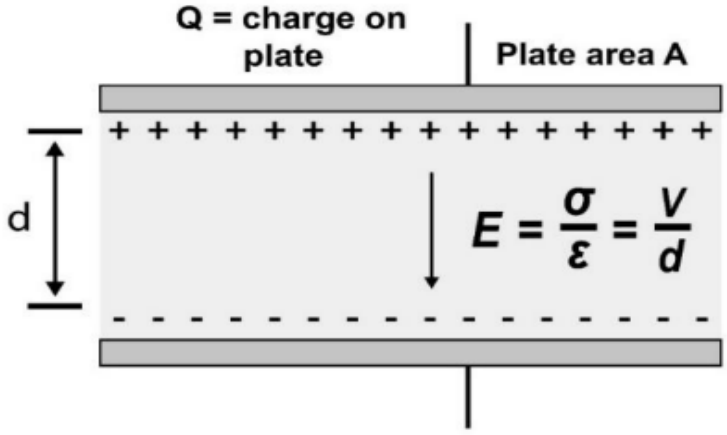

Figure 2.16 Parallel plate capacitor geometry [108]

In the parallel plate capacitor, setup depicted in Figure 2.16, the two platinum electrodes function as conductive plates with an area *A*, separated by a distance *d*. By inserting a dielectric material between the plates and applying a voltage, the electric charge on the plates increases. The

resulting potential difference between the plates is directly depending on the quantity of charge which is held on them.

$$Q \; \alpha \; V$$

$$Q \; = \; constant \; V$$

$$Q \; = \; C \; V \qquad 2.3$$

Where *V* denotes the applied voltage, *Q* denotes the charge, and *C* is the capacitor's capacitance. The electric field between the capacitor's plates is calculated using Gauss's equation and is given by;

$$E \; = \frac{\sigma}{\varepsilon_o}$$

By putting the value of *E* in the equation 2.3, the capacitor's plates' potential difference is;

$$V = \; Ed \; = \left(\frac{\sigma}{\varepsilon_o}\right)$$

$$V = \frac{Qd}{\varepsilon_o A}$$

From Equation 2.3, capacitance is given as

$$C = \frac{Q}{V} = \frac{\varepsilon_o A}{d}$$

Now dielectric material is placed which result in increase in capacitance of capacitor

$$C' = \; \varepsilon_r C = \frac{\varepsilon_r \varepsilon_o A}{d}$$

$$\varepsilon_r = \frac{C'd}{\varepsilon_o A} = \frac{\varepsilon}{\varepsilon_o}$$

Where $\varepsilon_o, \varepsilon_r$ and ε is already defined above. The dielectric constant is complex quantity i.e., It is composed of both real and imaginary parts and given by;

$$\varepsilon = \; \varepsilon' + \varepsilon''$$

Where ε′ is a real part or in phase part that represents the energy stored within the material and ε′′ is imaginary part or out of phase part which represents dielectric loss exhibited by the material.

2.7.1. Dielectric Loss:

The Dielectric loss is basically the energy dissipation in material which is caused by the charge migration when the direction of polarization changes according to an externally applied electric field. When a dielectric substance is exposed to an oscillating electric field, it absorbs electrical energy. This is referred to as "dielectric loss".

Figure 2.17 Dielectric Setup

In the present work, LCR Meter Bridge is used for measuring permittivity as a function of temperature at various frequencies as shown in figure 2.17. A Wayne Kerr LCR meter was used to test the samples' capacitance and dielectric loss over the frequency range of 1 kHz to 1 MHz. 90 K to 470 K is the measuring range for temperature. The LCR meter is connected to a computer system, which shows the results on the screen.

Chapter 3 Structure and Characterization

This chapter will address the process of preparing the samples, which involves the synthesis of Cobalt Ferrite ($CoFe_2O_4$) nanoparticles, as well as the preparation of solutions and films of P(VDF-TrFE), and the composite P(VDF-TrFE)/CFO. The synthesis process and subsequent structural analysis will be discussed in detail.

3.1. Synthesis:

The synthesis process will be presented in accordance with the outlined flow chart that is Figure 3.1.

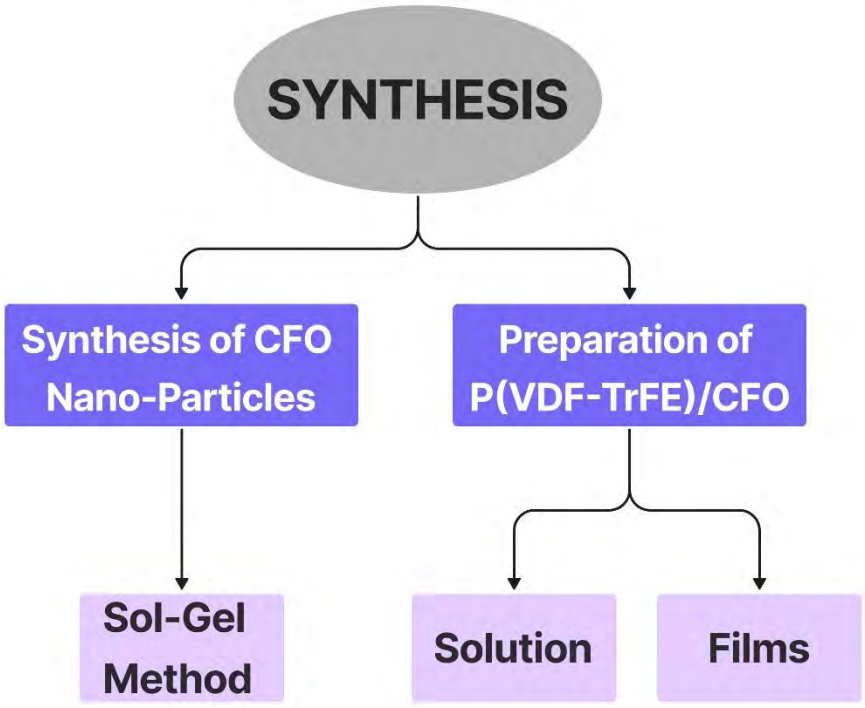

Figure 3.1 Outline of Synthesis

3.1.1. Cobalt Ferrite Nanoparticle Synthesis:

CFO nanoparticles can be made via a variety of techniques, such as co-precipitation [109], wet chemical route [110], precipitation, heat treatment [111], and sol-gel. Particularly effective, economical, and time-saving is the sol-gel technique. The sol-gel approach was used in the present

study for making CFO nanoparticles, and the process is described in detail below, also the details of the precursors and solvents is given in table 3.1.

Table 3.1 Precursors Used In the Synthesis of CFO Nanoparticles.

Chemicals	Formula	Purity	Suppliers
Cobalt Nitrate Hexahydrate	$Co(NO3)_2 \cdot 6H_2O$	99%	Aladdin® China
Iron Nitrate Nanohydrate	$Fe(NO_3)_2 \cdot 9H_2O$	99.99%	RHAWN™ China
Acetic Acid	CH_3COOH	99.80%	Chem.-Lab Belgium
Ethylene Glycol	$C_2H_6O_2$	99%	PANREAC QUMICA SA

3.1.1.1. Synthesis Method:

The process of synthesizing CFO (Cobalt Ferrite) nanoparticles involves mixing stoichiometric amounts of Cobalt nitrate hexahydrate ($Co(NO_3).6H_2O$) with ethylene glycol ($C_2H_6O_2$) and acetic acid (CH_3COOH) to create Solution-1, and mixing stoichiometric amounts of Iron nitrate nanohydrate with ethylene glycol and acetic acid to create Solution-2. These solutions are then stirred separately for 2 hours without heat, and then mixed together in a separate beaker and stirred for an additional 4 hours and 30 minutes without heat. The resulting solution is then placed on a magnetic stirrer at 60 ºC for 30 minutes, poured into a Petri dish, and covered with aluminum foil. After making small pores in the aluminum foil which is for easy and steadily evaporation, the Petri dish is placed in an oven at 80 ºC for 14 hours, leading to the forming of a solid gel. The solid gel is then grind into nanoparticles in acetone with a mortar and pestle for 60 minutes (figure 3.2a). These nanoparticles were placed in boats (figure 3.2b) and then post-annealed in a tube furnace with ambient air, using the annealing temperature for controlling the nanoparticles size. Finally, the CFO nanoparticles are calcined in a tube furnace at 800 ºC for 240 minutes. The synthesis procedure is depicted in flow chart i.e. Figure 3.3.

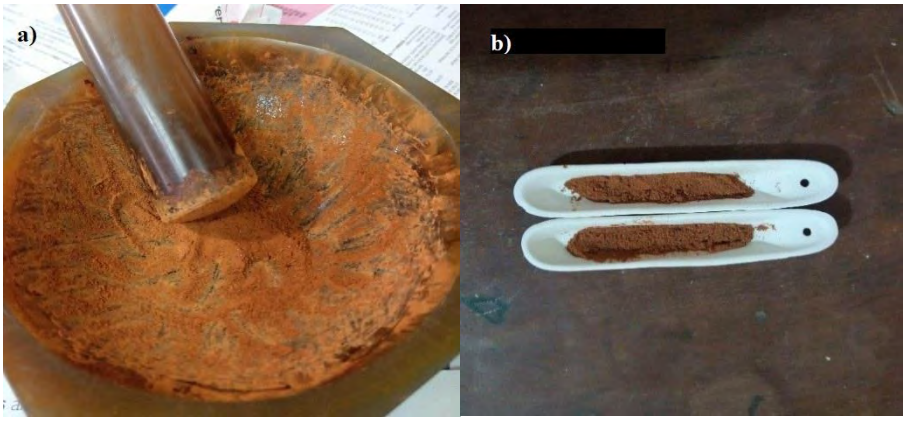

Figure 3.2 CFO Nanoparticles a) During Grinding b) Before Calcination

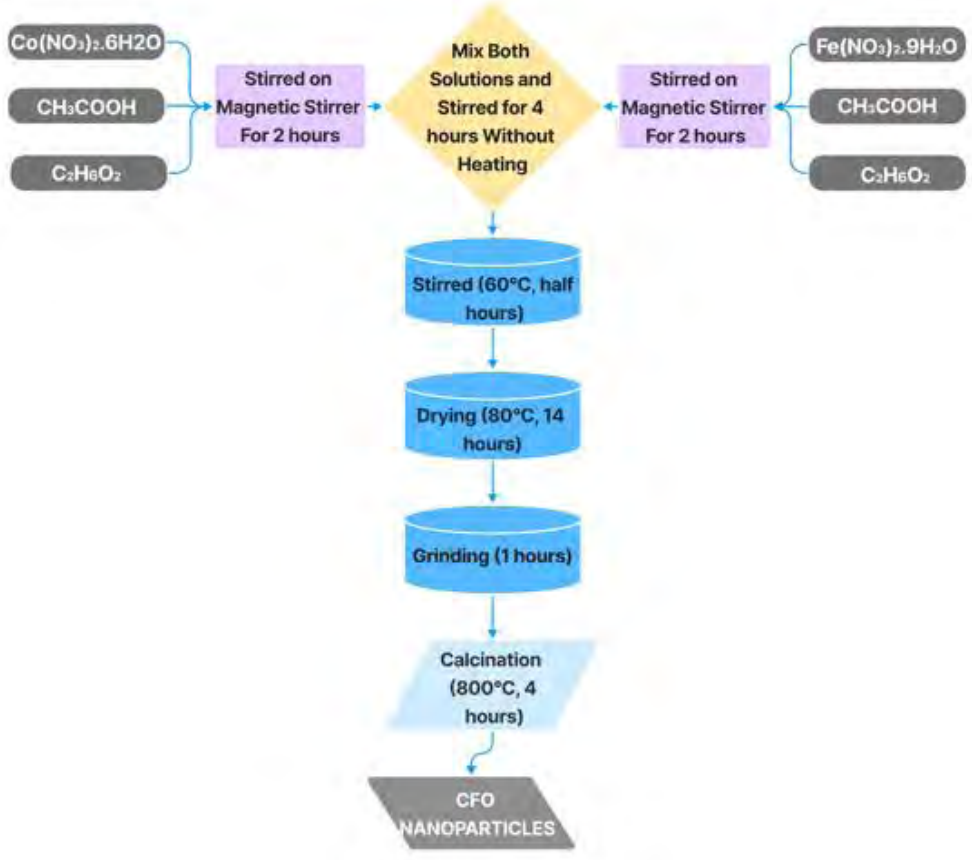

Figure 3.3 Synthesis of CFO Nanoparticles

3.1.2. Preparation of P(VDF-TrFE) and P(VDF-TrFE)/CFO Films:

Various techniques can be employed to produce P(VDF-TrFE) and P(VDF-TrFE)/CFO free-standing films, such as solvent casting, spin coating, electrospray deposition (ESD),

electrospinning, and spray coating. This study used solvent casting to create free-standing films of P(VDF-TrFE) and P(VDF-TrFE)/cobalt ferrite composite films, which were prepared with varying concentrations of CFO. The composite films were named according to their respective CFO concentrations, ranging from 00% to 25%: P(VDF-TrFE)/Pure, P(VDF-TrFE)/CFO 95/5, P(VDF-TrFE)/CFO 90/10, P(VDF-TrFE)/CFO 85/15, P(VDF-TrFE)/CFO 80/20, P(VDF-TrFE)/CFO 85/25.

3.1.2.1. P(VDF-TrFE) Solution Preparation:

To prepare the P(VDF-TrFE) 15 wt% solution, the appropriate amount of the polymer was dissolved in DMF using a magnetic stirrer. First, DMF was added to a beaker and heated on a magnetic stirrer. Then, the calculated amount of P(VDF-TrFE) for a 15 wt% solution was added to the beaker and stirred for 1 hour at 60 ºC. The solution was then left to stir at room temperature for 24 hours to ensure that all polymer chains were aligned. A flowchart illustrating the steps for preparing the P(VDF-TrFE) solution is shown in Figure 3.4.

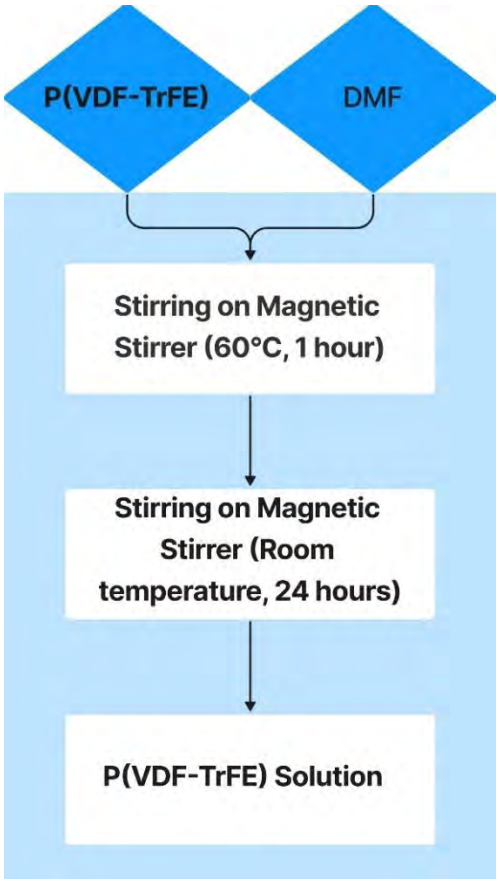

Figure 3.4 Flow Chart of Preparation of P(VDF-TrFE) Solution

3.1.2.2. P(VDF-TrFE)/CFO Composite Solution Preparation:

In order to create a P(VDF-TrFE)/CFO hybrid solution, cobalt ferrite nanoparticles were mixed into a polymer solution and stirred continuously for 3 hours using an electric motor powered by a DC power supply with a voltage of 1.8V and current of 4A. The resulting solution was uniform and homogeneous. Five different solutions were then created, each with a varying concentration of CFO: 5%, 10%, 15%, 20%, and 25%. Figure 3.5 displays a flow chart outlining the steps involved in preparing the P(VDF-TrFE)/CFO composite solution.

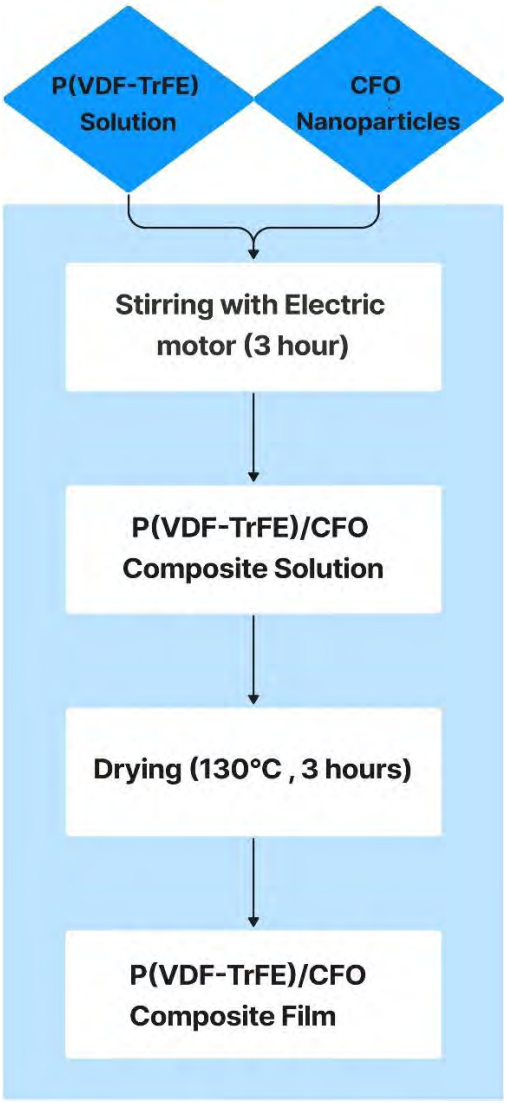

Figure 3.5 Flow Chart of Procedure of P(VDF-TrFE)/CFO Composite Film

3.1.3. Film Fabrication:

A hand-made 3×1 inch glass cavity was utilized for the formation of P(VDF-TrFE) and P(VDF-TrFE)/cobalt ferrite free-standing films. The prepared solution was filled into the cavity and then subjected to the oven. For P(VDF-TrFE) copolymer films, the evaporation temperature was set at 130 °C for a duration of 3 hours in the oven. P(VDF-TrFE) films were prepared using pure P(VDF-TrFE) solutions, while composite films of P(VDF-TrFE)/cobalt ferrite with varying concentrations (05wt%, 10wt%, 15wt%, 20wt% and 25wt %) of CFO were fabricated using a composite solution. The film fabrication process for composite films using the dry casting method is illustrated in Figures 3.4 and 3.5. Additionally, an 3×1 inch film of P(VDF-TrFE)/CFO 85/15 is presented in Figure 3.6.

Figure 3.6 3×1 Cavity

3.2. Characterization:

The samples were subjected to two types of structural characterization, namely X-rays diffraction (XRD) and Fourier Transform Infra-Red (FTIR) Spectroscopy. The XRD analysis will be discussed first, followed by the FTIR analysis.

3.2.1. X-Ray Diffraction:

The structural characteristics of the produced samples were analysed using the X-ray diffraction (XRD) technique. XRD study was conducted on all the films using the PANalytical Empyrean system in the 2θ range of 10º-80º with an angle increment of 0.02º and a step time of 1 second. The patterns of XRD of the P(VDF-TrFE), pure CFO, and P(VDF-TrFE)/cobalt ferrite composite films are presented in Figure 3.7 below.

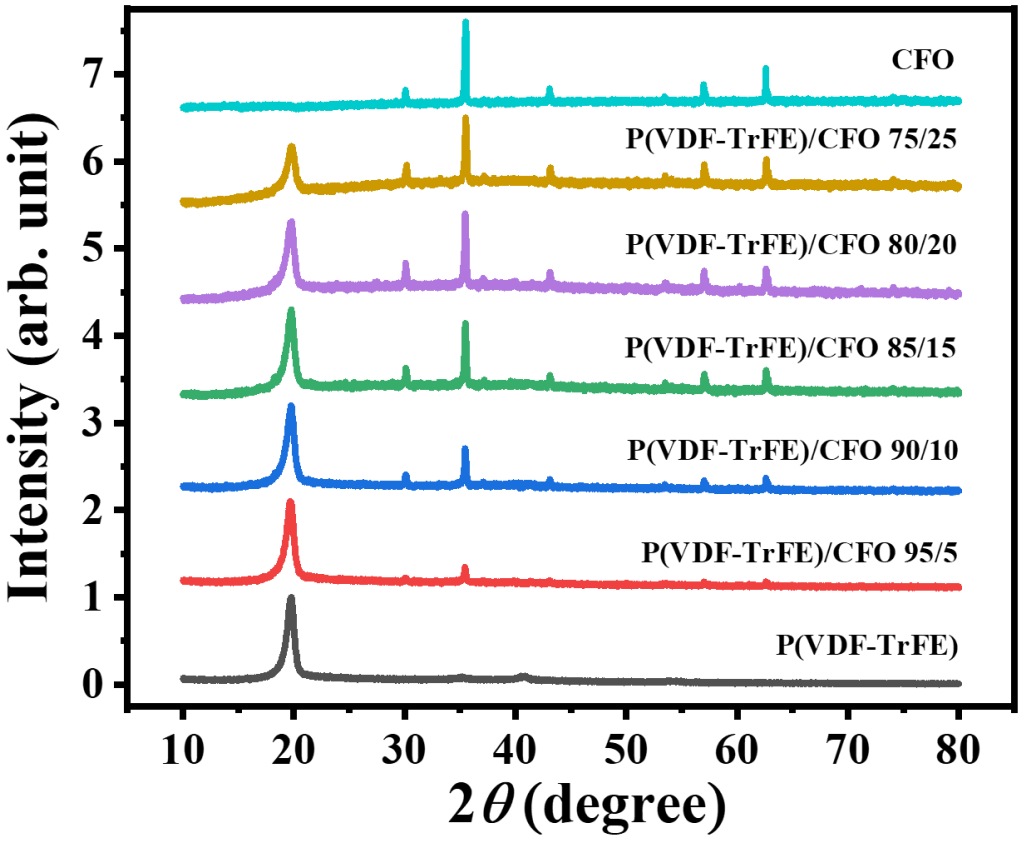

Figure 3.7 Pattern of XRD of Pure CFO and P(VDF-TrFE)/CFO Composite Films

The XRD peaks of pure cobalt ferrite (CFO) indicate a perfect match with the reference card PDF # 2.2-1086, confirming the presence of cobalt ferrite's spinel phase [112]. The XRD pattern of pure CFO in figure 3.7 displays multiple peaks corresponding to different diffraction planes such as (220), (311), (111), (511), and (440) [113], which are located at 29.8º, 35º, 42.8º, 56.7º, and 62º, respectively. These peaks confirm that the CFO material is crystalline.

The absence of any additional diffraction peaks rules out the existence of any impurity phases, which confirms the successful synthesis of pure cobalt ferrite nanoparticles. Furthermore, the application of the Scherer formula can assist in determining the average crystallite size of the CFO nanoparticles.

$$D = \frac{k\lambda}{\beta cos\theta}$$

Where k is the shape factor (constant value), λ is the X-rays wavelength, β is the full width half maxima (FWHM), and θ is Bragg's angle [88]. For CFO nanoparticles, the value of D is 36.72 nm as determined from the (311) peak.

The XRD pattern of P(VDF-TrFE) exhibits a strong peak at $2\theta = 19.8^{o}$, which refers to the (110) and (200) crystal planes of the β-phase, indicating the semi-crystalline nature of the polymer [114]. The sharpness of this peak indicates that only a single phase exists. Upon annealing P(VDF-TrFE) at 130 ºC, its crystallinity increases [115]. The composite samples XRD patterns demonstrate the presence of diffraction peaks for both polymer and cobalt ferrite nanoparticles.

In the P(VDF-TrFE)/CFO composite films with varying concentrations (95/5, 90/10, 85/15, 80/20, 75/25), a strong peak related to the β-phase at $2\theta = 19.8^{o}$ is present, but its intensity decreases as the concentration of CFO increases in the P(VDF-TrFE)/CFO composite films. This reduction in peak intensity suggests that the concentration of CFO nanoparticles affects the β-phase structure of P(VDF-TrFE), possibly due to the increased aggregation of nanoparticles at higher concentrations, which leads to non-uniform dispersion [116].

In all the composite films, CFO main intensity peak is observed at $2\theta = 35^{o}$. It is observed that with increase in the concentration of CFO nanoparticles in the P(VDF-TrFE)/CFO composite films, intensity of the peak related to CFO nanoparticles. Furthermore, the addition of a low concentration of nanoparticles induces crystallization of the β-phase polymer matrix [117]. However, the peak intensity of P(VDF-TrFE) decreases as the filler concentration increases [116].

3.2.2. Fourier Transform Infra-Red Spectroscopy:

The use of Fourier-transform infrared spectroscopy (FTIR) is used for the detection of various types of bonds present in a crystal. The FTIR pattern of all the samples prepared is shown

in Figure 3.8, and the majority of the copolymer's infrared-active vibrations occur in the range of 400–1500 cm^{-1}. This concentration of vibrational modes is attributed to the comparatively larger mass of the fluorine atom present in the material [118]. In spinel ferrites, two types of vibration modes are typically observed: octahedral sites, which appear in the frequency range of 370–430 cm^{-1}, and tetrahedral locations, which are apparent in the frequency range of 500–600 cm^{-1} [87]. Additionally, a minor peak at 580 cm^{-1} corresponds to a characteristic peak of spinel ferrite [113].

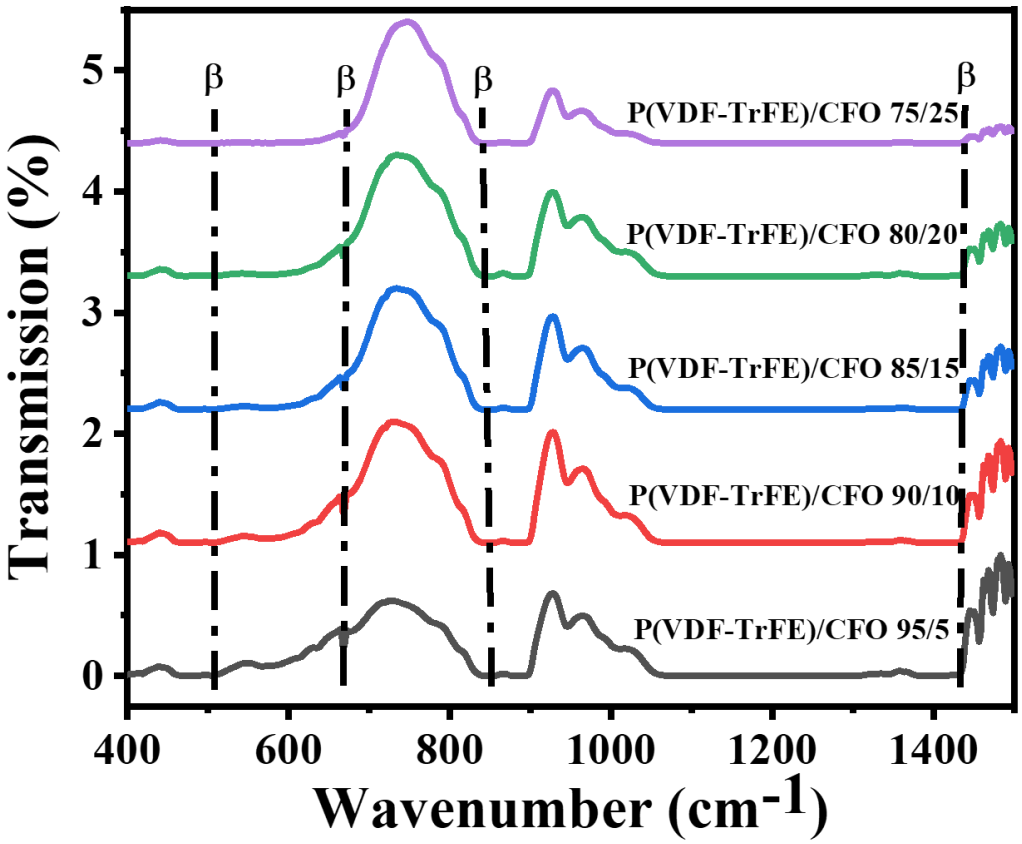

Figure 3.8 FTIR Pattern of Pure CFO and P(VDF-TrFE)/CFO Composite Films

The P(VDF-TrFE) polar *β*-phase exhibits stretching vibrations at 504, 661, 841, and 1431 cm^{-1} [113]. In the 520-580 cm^{-1} range, absorption bands indicate tetrahedral metal-oxygen bonding stretching vibrations, whose intensity decreases as the concentration of CFO filler content in P(VDF-TrFE) increases. At 578 cm^{-1}, the stretching vibrations of Fe^{3+} [76] ↔ O bond are observed in the tetrahedral site. The intensity of this mode decreases up to the 15wt% CFO sample, beyond

which it disappears completely. Additionally, a mode at 838 cm^{-1} is assigned to the mixed CH_2 rocking vibrations and CF_2 asymmetric stretching, which is characteristic of the β-phase [119].

The absorption modes assigned to the tetrahedral complexes, which are observed at 583-587 cm^{-1}, also decrease in intensity as the filler content increases [120]. As the amount of magnetic nanoparticles (CFO) increases, the ferroelectric beta-absorption decreases in all samples, up to the P(VDF-TrFE)/CFO ratio of 75/25. These findings are consistent with previous research articles, as cited in reference [121].

Chapter 4 Result and Discussion

The results of ferroelectric and dielectric properties of all the prepared samples at different sintering temperatures will be discussed in this chapter.

4.1. Ferroelectric Properties:

The standard Sawyer Tower circuit, as previously described in section 2.3, was utilized to measure the ferroelectric hysteresis loops. *P-E* loops are tested at 10 Hz frequency and room temperature. Gold (*Au*) electrodes were deposited on thick films for measuring ferroelectric hysteresis loops, through the sputter coater method. *P-E* hysteresis loops of P(VDF-TrFE) measured at different voltages are shown in figure 4.1. Saturated ferroelectric hysteresis loops are observed, with increased value of maximum polarization as a function of applied voltage. Observed saturated hysteresis loops confirms the presence of *β*-phase in P(VDF-TrFE) as claimed in XRD analysis.

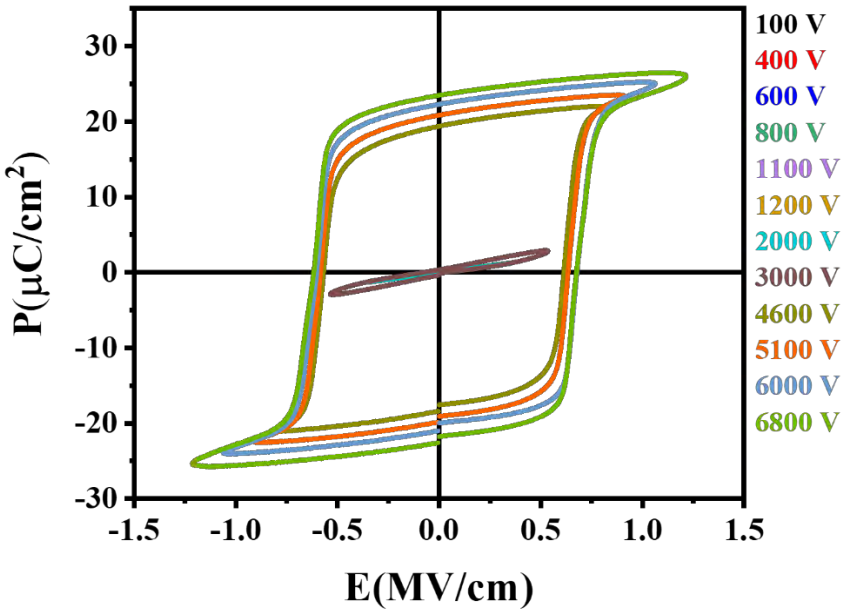

Figure 4.1 *P-E* hysteresis loop of P(VDF-TrFE) at 10 Hz

Ferroelectric hysteresis loops of all composite films at room temperature, are shown in figures 4.2 (a-d).

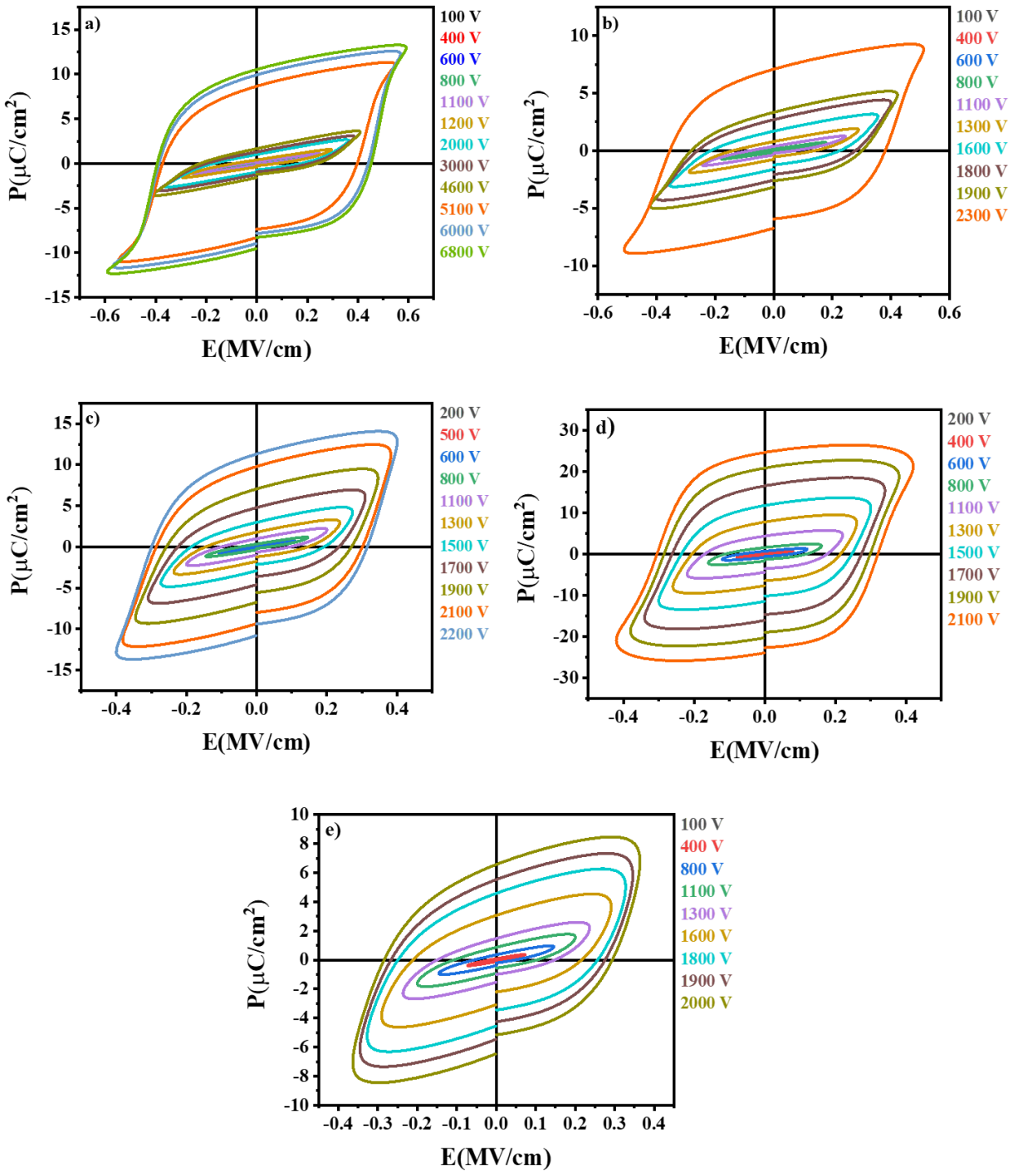

Figure 4.2 *P-E* loop at 10 Hz for a) P(VDF-TrFE)/CFO 95/5, b) P(VDF-TrFE)/CFO 90/10, c) P(VDF-TrFE)/CFO 85/15, d) P(VDF-TrFE)/CFO 80/20 and e) P(VDF-TrFE)/CFO 85/25

It is observed that with increasing the CFO concentration in P(VDF-TrFE) matrix, shape of the hysteresis loop changes from saturation towards circular form. Circular shape of the hysteresis loops indicates the lossy loop which is due to leakage current within a system. When the CFO is exposed to electric field, defects in the CFO structure causes its instability and because of this instability oxygen displace from its position. To get stability, electrons can undergo hopping between Fe^{+2} and Fe^{+3} states. This hopping occurs because the 3d orbital in Fe^{+3} is more stable then 3d orbitals in Fe^{+2} due to the crystal field effect. As a result, the electrons can move between these energy levels, leading to the leakage current and causes the conduction.

It is also observed from figures 4.1 and 4.2 that P(VDF-TrFE)/CFO composites have lower breakdown strengths as compared to P(VDF-TrFE). As the concentration of CFO increases, the higher instability in CFO, as described previously, leads to an increased number of electron hopping between Fe^{+2} and Fe^{+3} ions.. As a result, the samples contain high CFO content, greater the conduction is observed which result in its early breakdown.

Coercive field (E_c) of all the prepared samples are calculated at 10 Hz frequency and an applied field strength of 0.20 MV/cm. Calculated E_c are plotted as function of sample concentration as shown in figure 4.3(a). A strong correlation has been observed between the coercive field (E_c) and the concentration of cobalt ferrite (CFO) nanoparticles [116]. Increase in the values of coercive field are observed with increasing concentration of CFO nanoparticles. Calculated E_c value are 0.027, 0.044, 0.100, and 0.152 MV/cm, corresponding to 5%, 10%, 15% and 20% of CFO concentration respectively.

Two possible effects which are assumed to be responsible for such increase in E_c as a function of CFO concentration are explained below:

- **Dipole alignment effect:** When the electric field is applied on the P(VDF-TrFE), the polymer chains of P(VDF-TrFE) try to align themselves in the direction of applied electric field. By adding the CFO nanoparticles in P(VDF-TrFE), they act as center points for the electric field inside the P(VDF-TrFE)/CFO material. The electric field generated by the CFO nanoparticles has a stronger effect on the polymer chains of P(VDF-TrFE), and these polymer chains have an ability to align themselves more effectively as a result, so these effective alignment will require more electric field to randomize the chains.

- **Pinning effect:** In this effect, CFO nanoparticles strongly interact with P(VDF-TrFE), as a result CFO act as a pins to the P(VDF-TrFE) chains. They lock the polymer chains, so more electric field will be required to randomize those aligned chains. In the samples having higher CFO concentration, more CFO nanoparticles will help to lock the chains, hence E_c will be more.

Similarly, remnant polarization (P_r) is also calculated from the measured hysteresis loops at 10 Hz frequency and an applied field strength of 0.20 MV/cm. These measured values are also plotted as a function of CFO concentration as shown in figure 4.3 (c). From the graph it is observed that the remnant polarization of P(VDF-TrFE) films also increase with an increase in the concentration of CFO nanoparticles (see figure 4.3).The above two effects explained in coercive field also explain this increase in P_r as well. By increasing CFO concentration, more CFO nanoparticles will help the P(VDF-TrFE) chains to remain at their polarized state even when electric field is removed, results in enhancing the remnant polarization of P(VDF-TrFE).

Figure 4.3b shows that addition of CFO concentration cause increase in the maximum polarization of P(VDF-TrFE)/CFO because when the CFO nanoparticles are added to the P(VDF-TrFE), there is an interface between the CFO nanoparticle and the surrounding P(VDF-TrFE) chains. This interface can create an electric charge imbalance, leading to the accumulation of charges at the surface of the CFO nanoparticles. It can bring along some extra electric charges. These charges help to balance and stabilize the polarization of the P(VDF-TrFE). This stabilization makes it easier for the P(VDF-TrFE) to maintain its polarization in a specific direction, which results in a higher saturation polarization value. Higher the content of CFO higher will charges and hence higher will the maximum polarization.

The concentration of CFO leads to increase coercive field (E_c), maximum polarization (P_s) and remanent polarization (P_r). By analyzing the *P-E* loops at a voltage of 0.20 MV/cm, one can calculate the values of P_s, P_s, and E_c. The compilation of these parameters can be observed in Table 4.1.

Table 4.1 The P_s, P_r and E_c values at 0.20 MV/cm, Ferroelectric Hysteresis Measurements.

Sample Name	P_s (μC/cm²)	P_r (μC/cm²)	E_c (MV/cm)
P(VDF-TrFE)/CFO 5/95	0.8081	0.1015	0.0270351
P(VDF-TrFE)/CFO 90/10	0.8809	0.1842	0.0444032
P(VDF-TrFE)/CFO 85/15	2.2459	0.9924	0.1003394
P(VDF-TrFE)/CFO 80/20	4.4483	3.2418	0.1526911

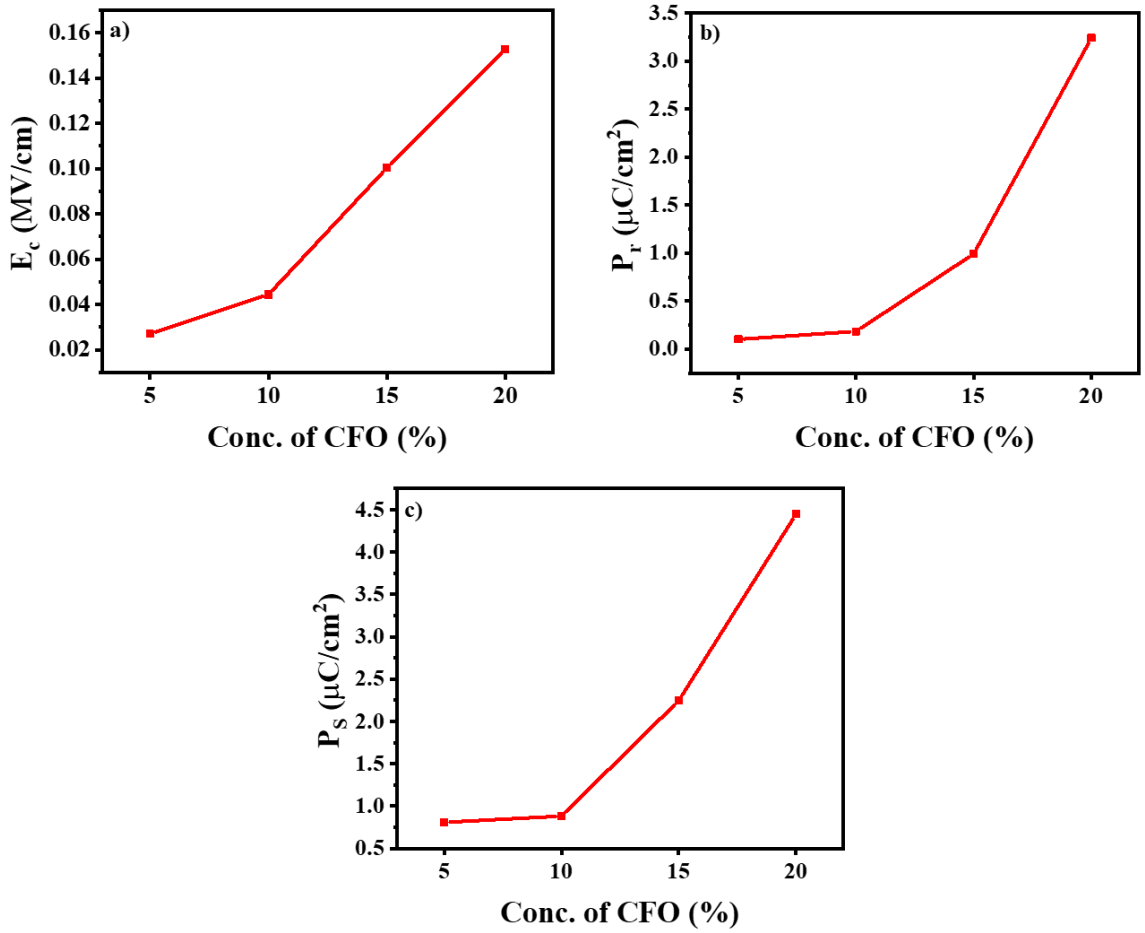

Figure 4.3 Value of a) E_c, b) P_s and c) P_r values plotted against weight fraction of CFO

At an electric field strength of 0.20 MV/cm and a frequency of 10 Hz, the loops of P(VDF-TrFE)/CFO with CFO concentration of 5%, 10%, 15% and 20% is shown in figure 4.4. It has been observed that the saturation polarization, remnant polarization, and coercivity of P(VDF-TrFE) films increase with an increase in the concentration of CFO, as shown in Figure 4.4.

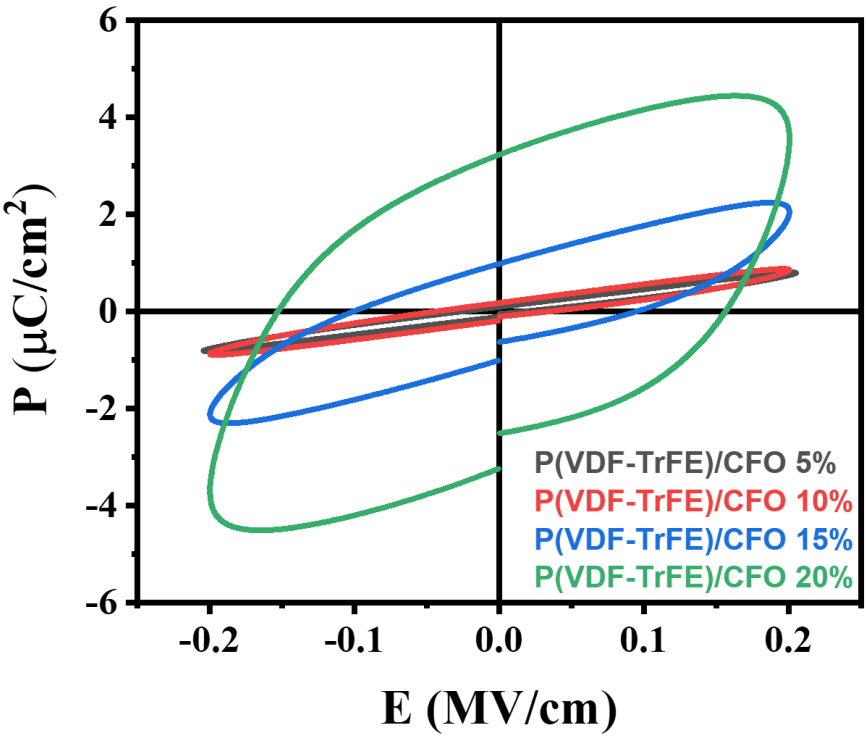

Figure 4.4 Ferroelectric loops of P(VDF-TrFE)/CFO films at maximum electric field of around 0.20 MV/cm

The introduction of CFO (cobalt ferrite) nanoparticles leads to a notable increase in the area under the loop as shown in figure 4.4. It is observed that at 0.20 MV/cm, maximum polarization increases. Additionally, at zero field the remnant polarization also increase, with this coercive field also increases, as a results it increases the area of loop [122, 123].

4.2. Dielectric response of P(VDF-TrFE) and P(VDF-TrFE)/CFO:

The temperature-dependent dielectric response of all the prepared films were taken over a frequency range from 1 kHz to 1000 kHz. Dielectric response of P(VDF-TrFE) as a function of temperature is shown in figure 4.5.

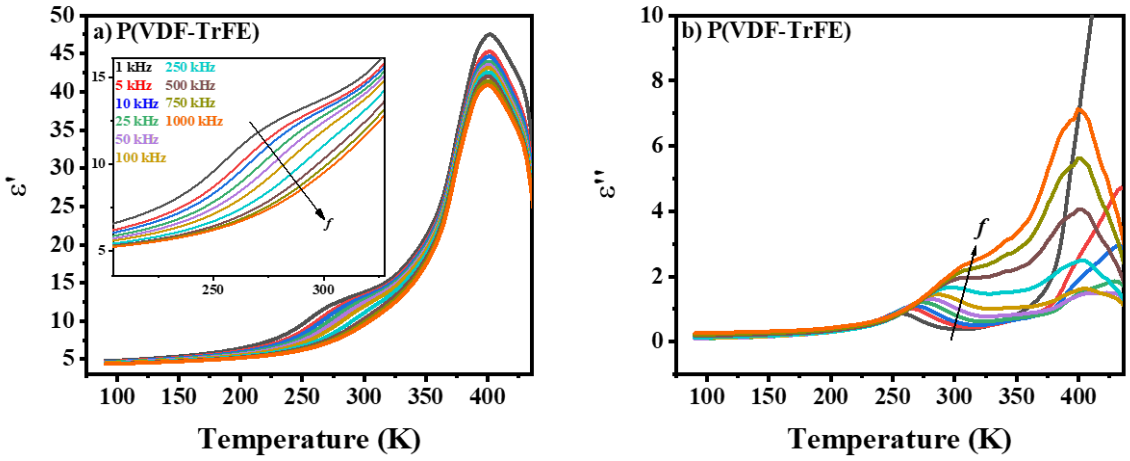

Figure 4.5 Dielectric response of P(VDF-TrFE) films

Figures 4.5 show three separate regions in the in-phase (ε') and out-of-phase (ε'') portions of the dielectric constant P(VDF-TrFE). The first region (80–200 K) is a temperature independent region where all the dipoles are frozen and an increase in temperature has no effect on the values of ε' and ε''. In the second temperature range (200–350 K), there is a broad peak in the in-phase (ε') and out-of-phase component (ε'') of dielectric constant. The third region (over 350 K) also shows a sharp increase in both in-phase and out-of-phase constant.

In the lower temperature region (80 K-200 K) of P(VDF-TrFE), the in-phase and out-of-phase part of dielectric permittivity almost remain constant as a function of temperature. In this temperature region, an increase in temperature has no effect on the values of ε' and ε''. Despite the polar nature of P(VDF-TrFE), it behaves as non-polar in this temperature range. Because at low temperature the chains of the polymer are frozen [124] and have no significant motion. Wei Jin Hu *et al.* research on temperature-dependent ferroelectric characteristics [125] also supports the

fact that 200 K is considered as the critical temperature, below which P(VDF-TrFE) and its composites lose their polar nature..

With increase in temperature i.e. second region 200 K-350 K, increase in the in-phase part of dielectric constant (ε') is observed and consistent peaks is observed in the out-of-phase dielectric constant. When temperature increases, the movement of the dipoles in the P(VDF-TrFE) chain gets stronger. When the temperature reaches glass transition temperature (T_g), chain segments in amorphous regions get enough activation energy and leading to local micro-Brownian motion of molecular segments. As a result, both in-phase and out-of-phase part of dielectric constant increases [126].

In the third temperature region (above 350 K), the in-phase and out-of-phase parts of the dielectric constant again start increasing. This phenomenon corresponds to the phase transition from ferroelectric to paraelectric. The ferroelectric to paraelectric transition peak is observed in both the in-phase and out-of-phase parts of the dielectric constant. This phenomenon of phase transition also known as first order phase transition. In P(VDF-TrFE) below T_c, the lattice packing of all trans bonds in the polymer chains in which all of the fluorine atoms are positioned on one side and all of the hydrogen atoms are located on the other side causes the dipole moment of the crystalline phase. Trans conformation of polymer chains cannot be constant above T_c. As the fluorine atoms gain enough kinetic energy to show segmental rotation [127], their mutual repulsion from one another increases. At this temperature, the C-C bond on TrFE units begins to rotate freely, causing the P(VDF-TrFE) chain conformation to change from TTTT to TTTG. As a result, the long, highly polar P(VDF-TrFE) chain is divided into very short TTT segments with moderate or lower polarity in G or G' conformation. When the temperature increases above T_c, the ferroelectric domain becomes more disordered, which leads to a sharp decrease in the dielectric constant and a sharp increase in dielectric loss [128].

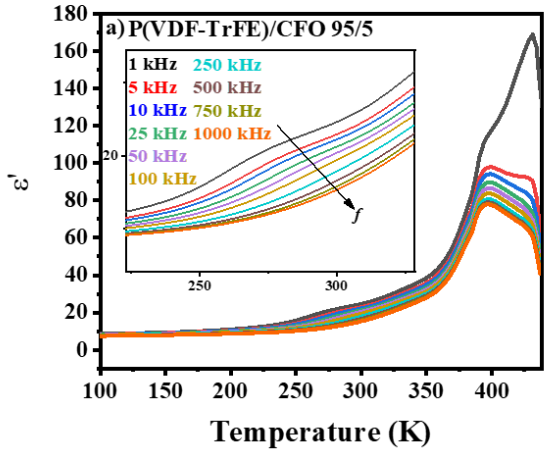
a) P(VDF-TrFE)/CFO 95/5
1 kHz
5 kHz
10 kHz
25 kHz
50 kHz
100 kHz
250 kHz
500 kHz
750 kHz
1000 kHz
f
ε'
Temperature (K)

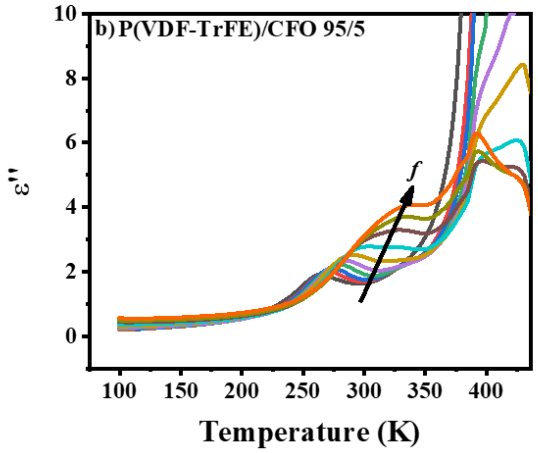
b) P(VDF-TrFE)/CFO 95/5
f
ε''
Temperature (K)

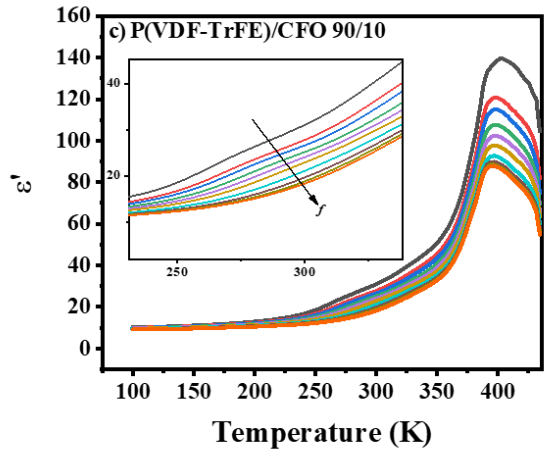
c) P(VDF-TrFE)/CFO 90/10
f
ε'
Temperature (K)

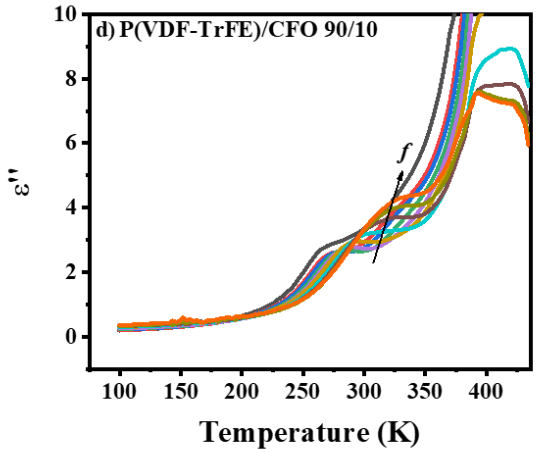
d) P(VDF-TrFE)/CFO 90/10
f
ε''
Temperature (K)

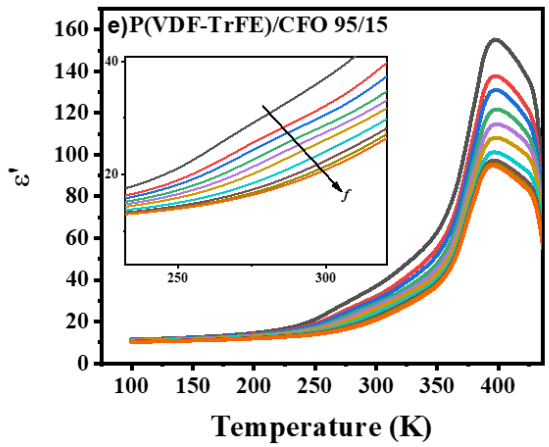
e) P(VDF-TrFE)/CFO 95/15
f
ε'
Temperature (K)

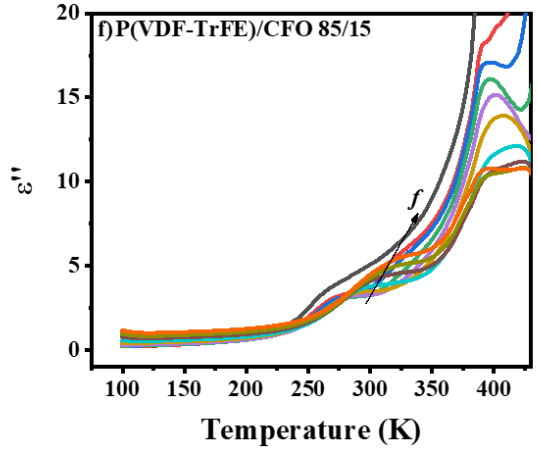
f) P(VDF-TrFE)/CFO 85/15
f
ε''
Temperature (K)

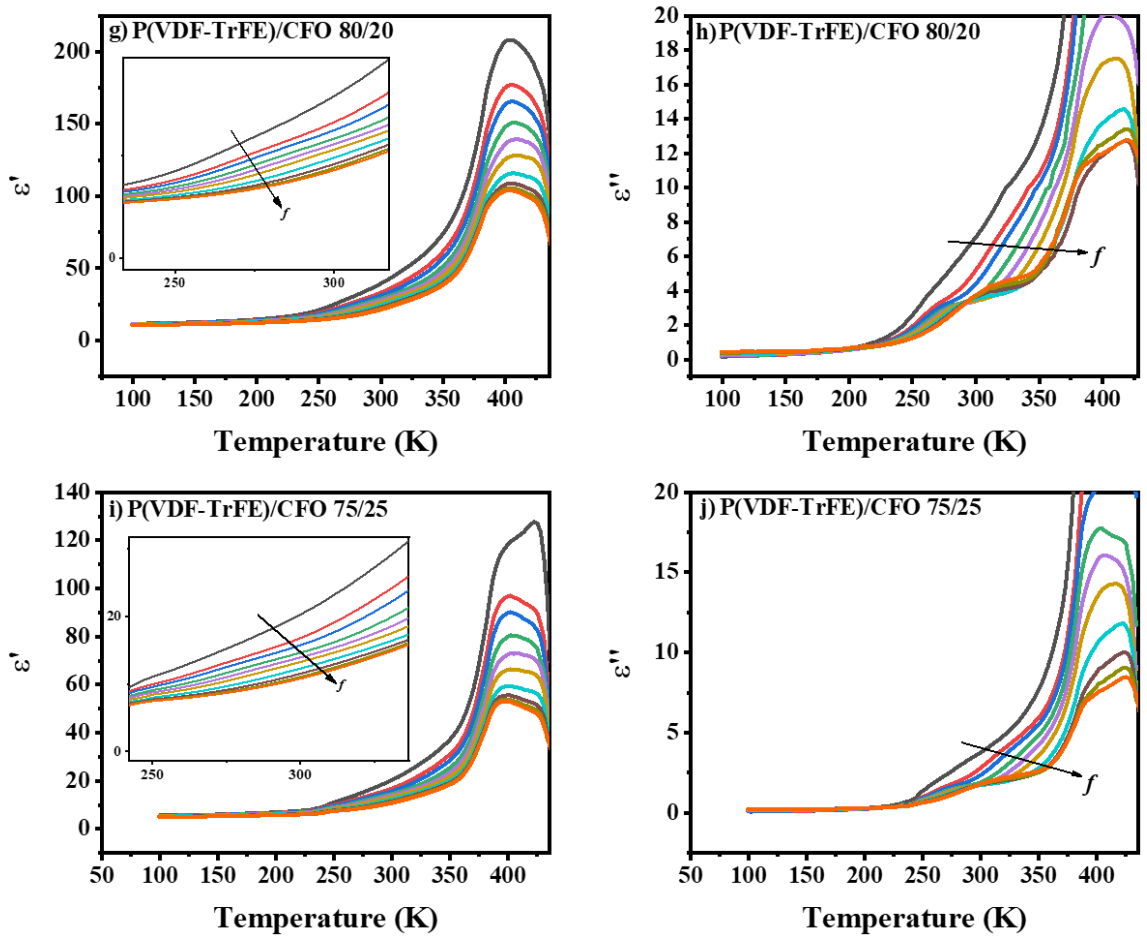

Figure 4.6 Dielectric response of P(VDF-TrFE)/CFO composite films a) In phase part of 5% CFO, b) Out of phase part of 5% CFO, c) In phase part of 10% CFO, d) Out of phase part of 10% CFO, e) In phase part of 15% CFO, f) Out of phase part of 15% CFO, g) In phase part of 20% CFO, h) Out of phase part of 20% CFO, i) In phase part of 25% CFO, j) Out of phase part of 25% CFO

Dielectric permittivity of P(VDF-TrFE)/CFO as a function of temperature are shown in figure 4.6. The in-phase and out-of-phase components of the dielectric constant are almost identical as a function of temperature for all frequencies in the low temperature range (80 K-200 K) which shows the same behavior as observed in P(VDF-TrFE). It has already been discussed that all the dipoles of CFO nanoparticles and P(VDF-TrFE) are frozen and act as non-polar in this low temperature range [124].

In the second region, which ranges from 200 K to 350 K, the glass transition peak, also known as β-relaxation, is observed in P(VDF-TrFE)/CFO, as shown in figure 4.6, but it gets broad when CFO content increases. This is because of the three reasons. Firstly, the addition of CFO nanoparticles restricts and limits the movement of chains of P(VDF-TrFE) (pinning effect), which affect the glass transition temperature, so when CFO concentration increases, the transition could become so small that it seems like there is no glass transition at all. Secondly, the interface of CFO nanoparticles with P(VDF-TrFE) chains causes polarization called interfacial polarization. This polarization increases the in-phase and out-of-phase parts of the dielectric constant. This caused the glass transition peak to broaden. As the concentration of CFO increases, the interfacial polarization effects become more prominent, potentially causing the glass transition peak to become less visible [129]. Thirdly, when CFO concentration is increased, the nanoparticles agglomerate. This agglomeration introduces heterogeneity and phase separation regions within the composite, which give rise to distinct regions having their own glass transition temperature. As a result, the glass transition peak in the in-phase and out-of-phase parts of the dielectric constant may become broader due to the presence of multiple overlapping transitions associated with these different regions.

At the temperature above 350 K, a second peak is observed in P(VDF-TrFE)/CFO in-phase and out-of-phase components of the dielectric constant. This peak in the in-phase and out-of-phase parts is due to the interfacial polarization. There are several interfacial contributions that cause this increase. The first contribution comes from the interface between the crystalline phase and the amorphous phase. P(VDF-TrFE) is composed of both crystalline and amorphous region; hence, heterogeneous interfacial polarization affects its dielectric response. The second interfacial contribution comes from the possibility of micro-crack formation during P(VDF-TrFE)/CFO film preparation. The third contribution comes from the interface between the CFO nanoparticles and P(VDF-TrFE) chains, which also enhances the dielectric constant [130].

It is observed that as the CFO content increases, the dielectric loss of composite films also increases. It occurs due to more particle aggregation in the films with an increase in CFO nanoparticles concentration, which results in increased conduction loss.

Another important observation in second and third region is the frequency dependence of dielectric constant. The value of ε' decreases as frequency increases because the dipoles may not

be able to keep up with the rapidly varying electric field. This trend is also same in all P(VDF-TrFE) and P(VDF-TrFE)/CFO films (see Figure 4.5 and Figure 4.6).

4.2.2. Activation energy of P(VDF-TrFE) and P(VDF-TrFE)/CFO composite films:

The activation energy for the β-relaxation in PVDF-TrFE and PVDF-TrFE/CFO composite films was calculated using the Arrhenius law. The linear fit for these films is shown in Figure 4.7, it is observed that glass transition temperature, and β-relaxation are related. The data needed to use the Arrhenius law to determine the activation energies of PVDF-TrFE and PVDF-TrFE/CFO composite films is provided in Table 4.2.

Table 4.2 β-relaxation peak temperatures at different frequencies for P(VDF-TrFE) and P(VDF-TrFE)/CFO composite films

Frequency (Hz)	P(VDF-TrFE)	P(VDF-TrFE)/ CFO 5%	P(VDF-TrFE)/ CFO 10%	P(VDF-TrFE)/ CFO 15%	P(VDF-TrFE)/ CFO 20%	P(VDF-TrFE)/ CFO 25%
1000	277.32	276.57	273.87	266.44	267.84	264.67
5000	280.15	279.12	276.57	275.62	273.97	273.76
10000	284.34	282.95	279.98	279.44	278.22	278.03
25000	288.42	286.34	282.68	282.31	283.4	282.9
50000	293.15	291.02	286.14	284.98	288.59	286.83
100000	296.7	294.42	290.31	290..08	292.48	292.02
250000	299.75	297.85	294.54	293.38	297.58	297.05
500000	300.23	300.82	297.59	296.05	301.54	299.28
750000	301.64	304.65	300.244	299.04	304.71	300.49
1000000	304.25	306.35	304.06	304.76	307.86	302.34

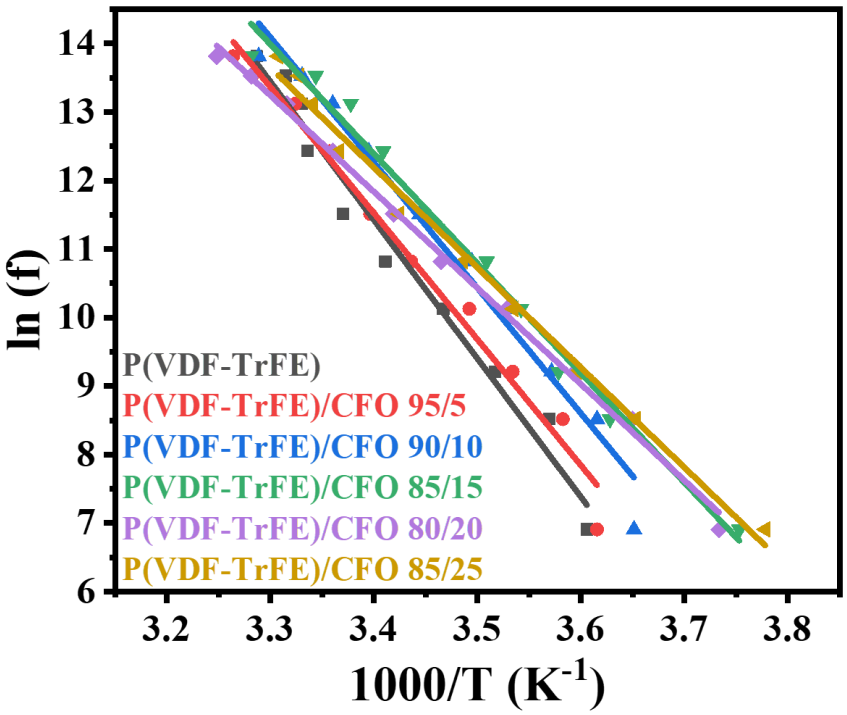

Figure 4.7 Arrhenius plots for the activation energies of P(VDF-TrFE) pristine and P(VDF-TrFE)/CFO composite films

Table 4.3 Activation energy estimated from β-relaxation peak, for P(VDF-TrFE) and P(VDF-TrFE)/CFO composite films

Sample Name	Activation Energy E_a (eV)
P(VDF-TrFE)	1.72
P(VDF-TrFE)/CFO 95/5	1.59
P(VDF-TrFE)/CFO 90/10	1.57
P(VDF-TrFE)/CFO 85/15	1.37
P(VDF-TrFE)/CFO 80/20	1.21
P(VDF-TrFE)/CFO 75/25	1.26

Table 4.3 shows activation energies of P(VDF-TrFE) and P(VDF-TrFE)/CFO composite films. With increases in CFO concentration, dielectric constant is also increasing which lower the activation energy. This is due to the fact that materials with higher dielectric constants allow charge carriers (like polar molecules or ions) to interact with the electric field more strongly, which helps their movement inside the material.

4.3. Magnetic Properties:

For some of the selected samples, magnetic measurements were taken at a magnetic field of 2 T. The graph of the magnetic moment versus magnetic field of the P(VDF-TrFE)/CFO 95/5, P(VDF-TrFE)/CFO 85/15, and P(VDF-TrFE)/CFO 75/25 at room temperature is depicted in Figure 4.8.

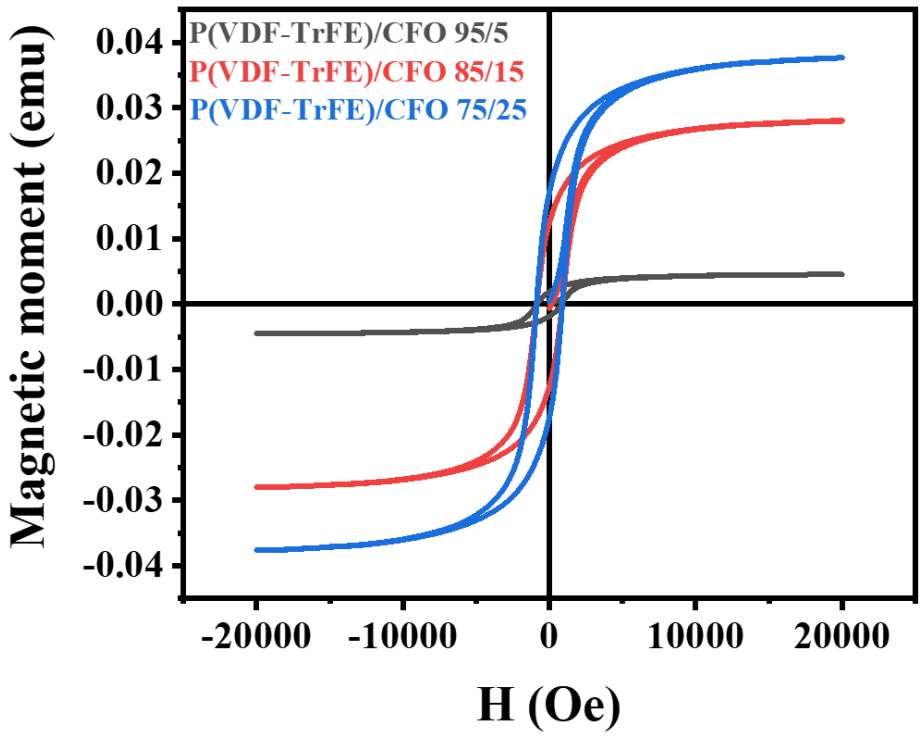

Figure 4.8: *M-H* loop of the samples

Ferromagnetic hysteresis loops are observed in all the three films of P(VDF-TrFE)/CFO due to the existence of CFO nanoparticles in it. Cobalt ferrite (CFO) contains intrinsic magnetic moments in the form of small magnetic fields that are connected to the spinning of the electrons

around the atomic nuclei of the cobalt (Co) and iron (Fe) ions. The magnetic moments of individual atoms align in a specific way in a magnetic material like cobalt ferrite to create a macroscopic magnetic effect [131].

From graph, it is observed that with increase in CFO concentration, the maximum magnetic moments (M_s) increases as depicted in figure 4.9b. This is due to the volume fraction of CFO nanoparticles and the magnetization of the film are related by:

$$M_s = \phi_{vn} M_{ns}$$

where ϕ_{vn} is the volume fraction of the nanoparticles in the composite film and M_{ns} is the saturation magnetization of each individual nanoparticle. So the sample having higher concentration of CFO will have higher value of maximum magnetic moments [132], as more nanoparticles will interact with polymer matrix and create a strong magnetic moment within the composite. The observed values of maximum magnetic moment of P(VDF-TrFE)/CFO 95/5, P(VDF-TrFE)/CFO 85/15 (M1), and P(VDF-TrFE)/CFO 75/25 is 0.00452 emu. 0.02802 emu and 0.03763 emu respectively.

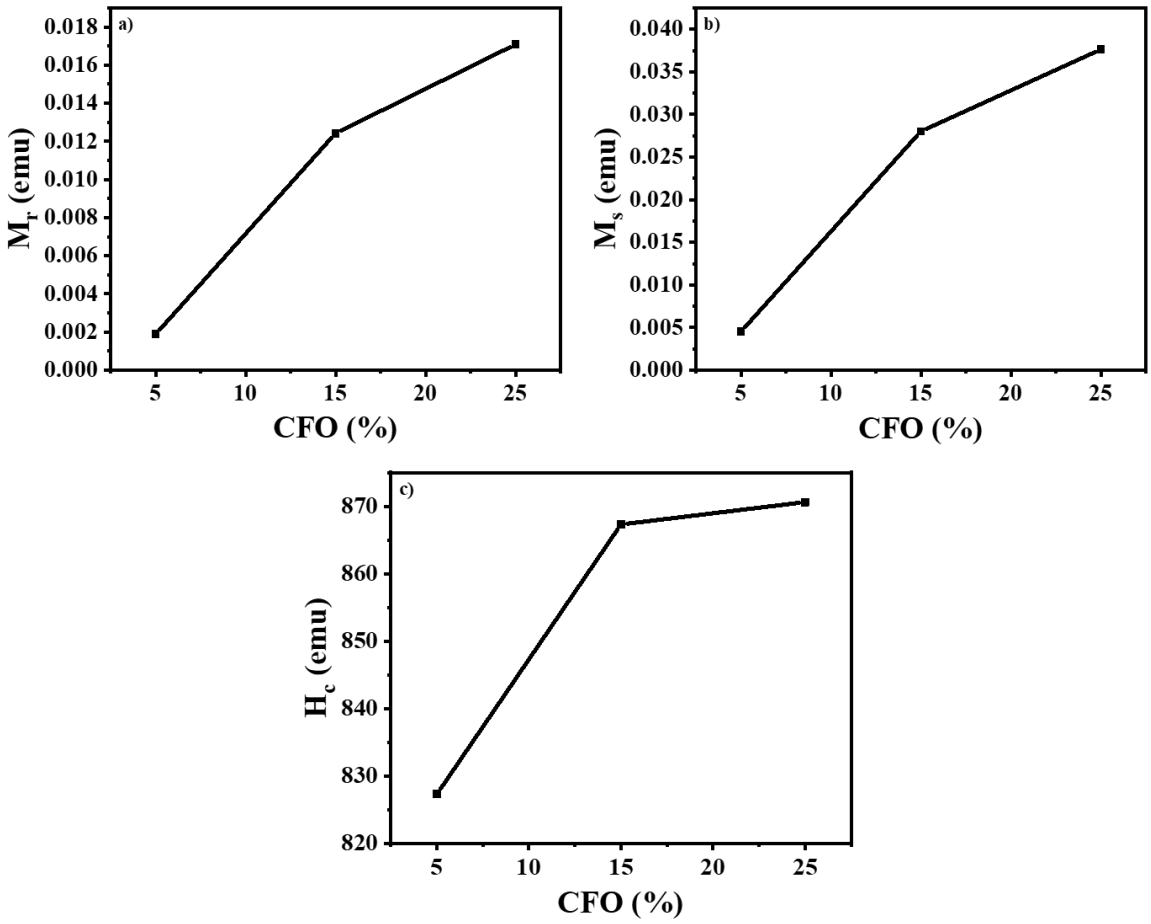

Figure 4.9 Effect on M_r, M_s, and H_c by increasing the concentration of CFO nanoparticles in P(VDF-TrFE)

When the concentration of CFO nanoparticles increases in polymer matrix, the overall magnetic strength of the composites increases. As a result the composite becomes more magnetically responsive, and it is capable of keeping its magnetic moment for long time even when the magnet field is removed which means its remanant magnetic moment (M_r) will increases with increases in CFO concentration as shown in figure 4.9a [127]. The observed values of remanent magnetic moment of P(VDF-TrFE)/CFO 95/5, P(VDF-TrFE)/CFO 85/15 (M1), and P(VDF-TrFE)/CFO 75/25 is 0.00188 emu. 0.01250 emu and 0.01718 emu respectively.

When the concentration of CFO nanoparticles increases in P(VDF-TrFE). The magnetic coercivity (H_c) also increases as depicted in figure 4.9c, as the CFO nanoparticles in the composite increases so high field will require to randomize all the dipoles.

Table 4.4 The Values of M_s, M_r and H_c from *M-H* loop of different concentration of CFO in P(VDF-TrFE)

CFO (%)	M_s (emu)	M_r (emu)	H_c (emu)
5	0.00189	0.00452	827.268
15 M1	0.01242	0.02802	867.313
25	0.01709	0.03763	870.615

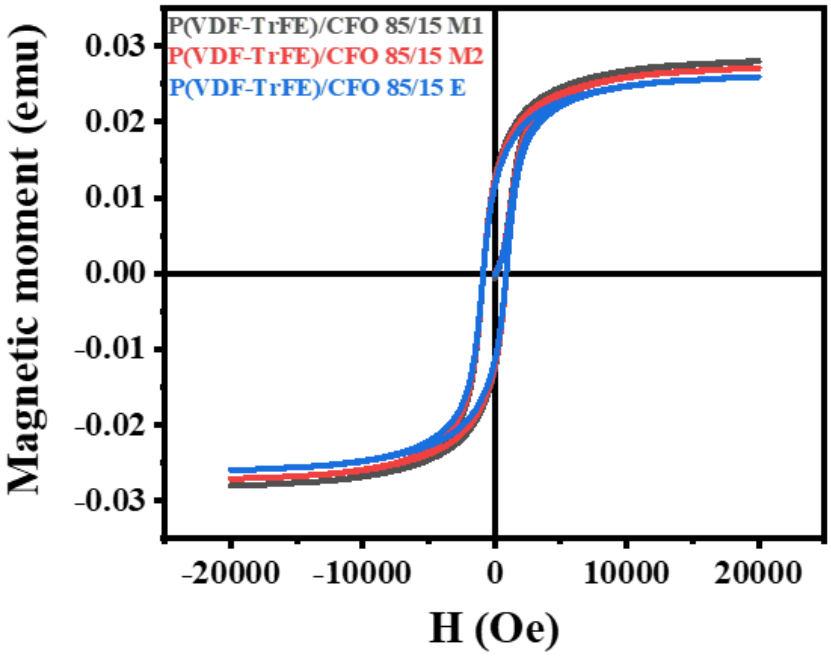

Figure 4.10: *M-H* loops of three different regions of P(VDF-TrFE)/CFO 15%

M-H loop is taken at three different regions of the film of P(VDF-TrFE)/CFO 85/15, i.e., M1 (from the mid of the film), E (from the edge of the film), and M2 (between E and M1), as shown in figure 4.11. Three different *M-H* loops at three different regions of the film are observed in figure 4.10, which indicates the inhomogeneity of the film. It means CFO nanoparticles are not well dispersed in the P(VDF-TrFE) matrix.

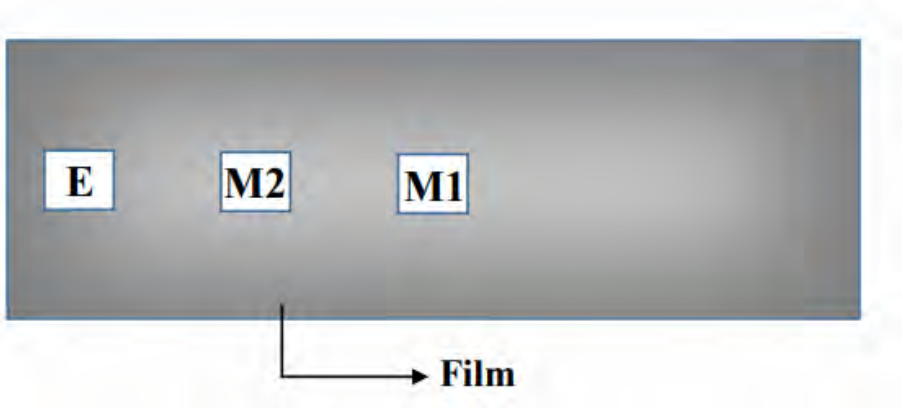

Figure 4.10 Three different regions *M1*, *M2* and *E* of the films

4.4. Summary and Conclusion:

Multiferroics are a class of materials that are composed of more than one ferroic orders. In the current work, ferroelectric polymer has been combined with ferromagnetic particles, forming a composite. In this work, the structural, electrical and magnetic properties of polymer nanocomposites with ceramic fillers are mainly investigated. These composites are in the form of flexible, free-standing film. The $CoFe_2O_4$ nanoparticles have been selected as a fillers due to their chemical stability, mechanical hardness, high saturation magnetization, coercivity and high electromagnetic performance. While P(VDF-TrFE) is chosen as the polymer matrix due to its high breakdown strength, ferroelectric properties, and mechanical flexibility. $CoFe_2O_4$ nanoparticles were synthesized by the sol-gel method. The cubic spinel structure of $CoFe_2O_4$ nanoparticles is confirmed by their XRD pattern. The addition of $CoFe_2O_4$ nanoparticles decreases the content of the β-phase and crystallinity of the P(VDF-TrFE) matrix, as shown by the XRD pattern of P(VDF TrFE)/$CoFe_2O_4$ composite films.

Ferroelectric loop measurements of P(VDF-TrFE) showed good ferroelectric loops, confirming that the addition of TrFE units in PVDF result in a high content of β-phase, which was also confirmed by XRD. Ferroelectric loop measurements of P(VDF TrFE)/$CoFe_2O_4$ films showed good ferroelectric loops at low $CoFe_2O_4$ filler concentrations, confirming that the $CoFe_2O_4$ nanoparticles are well dispersed in the polymer matrix. However, the loop become circular when the concentration is increased to 25% because extra charges in $CoFe_2O_4$ induces conductivity. Comparing P(VDF TrFE)/$CoFe_2O_4$ composite films with varying $CoFe_2O_4$ content at 0.20 MV/cm

showed the contribution of interfacial polarization and leakage current increases the value of saturated polarization at the given field as the content of $CoFe_2O_4$ filler increases. Additionally, coercivity and remnant polarization also increase mainly due to the pinning effect of $CoFe_2O_4$ nanoparticles within the polymer matrix. Another significant observation was the decrease in the breakdown electric field of composite films with an increase in $CoFe_2O_4$ content. Temperature-dependent dielectric measurements showed that the dielectric constant increases with increase in the concentration of $CoFe_2O_4$ nanoparticles but when $CoFe_2O_4$ concentration increases to 25% the dielectric constant drops due to a decrease in the content of the β-phase, which was confirmed by XRD. *M-H* loops of the selected samples were taken, which indicates that by increasing CFO concentration, the maximum magnetic moment will also increase. However, three different *M-H* loops at three different regions of the film illustrated that CFO nanoparticles are not well dispersed within the polymer matrix.

References

1. Feynman, R.P. *Plenty of Room at the Bottom*. in *APS annual meeting*. 1959.
2. Lockwood, D.J., *Nanostructure science and technology*. 2005, Springer.
3. McClelland, J.J., et al., *Nanotechnology with atom optics.* Science and Technology of Advanced Materials, 2004. **5**(5-6): p. 575.
4. Cowburn, R., *The attractions of magnetism for nanoscale data storage.* Philosophical Transactions of the Royal Society of London. Series A: Mathematical, Physical and Engineering Sciences, 2000. **358**(1765): p. 281-301.
5. Sarikaya, M., et al., *Molecular biomimetics: nanotechnology through biology.* Nature materials, 2003. **2**(9): p. 577-585.
6. Kumar, N. and S. Kumbhat, *Essentials in nanoscience and nanotechnology*. 2016: John Wiley & Sons.
7. Nasrollahzadeh, M., et al., *Applications of nanotechnology in daily life.* Interface science and technology, 2019. **28**: p. 113-143.
8. Benelmekki, M., *Introduction to nanoparticles and nanotechnology*, in *Designing Hybrid Nanoparticles (Second Edition)*. 2021, IOP Publishing.
9. Wilhelm, P.D.M., *Introduction to Polymerscience.* 2019.
10. Amsc, N. and A.A. CMPS, *Composite materials handbook.* Polymer matrix composites materials usage, design, and analysis, 2002.
11. Yılmaz, E., *Preparation and characterization of polymer composites containing gold nanoparticles*. 2011, Bilkent Universitesi (Turkey).
12. Morgan, P.W., *Brief history of fibers from synthetic polymers.* Journal of Macromolecular Science—Chemistry, 1981. **15**(6): p. 1113-1131.
13. Kittel, C., *Introduction to solid state physics Eighth edition.* 2021.
14. Davis, D.C.L., *Dielectric Materials.*
15. Kao, K.C., *Dielectric phenomena in solids*. 2004: Elsevier.
16. Hongbo, L., *Dielectrics under Electric Field.* Electric Field, 2018: p. 322.
17. Wang, B., et al., *High-k gate dielectrics for emerging flexible and stretchable electronics.* Chemical reviews, 2018. **118**(11): p. 5690-5754.
18. Lasaga, A.C. and R.T. Cygan, *Electronic and ionic polarizabilities of silicate minerals.* American Mineralogist, 1982. **67**(3-4): p. 328-334.
19. *Various Polarization Processes.*
20. Balasubramanyam, J., M. Lohith K S, and S. Thomas, *Lecture Notes on Engineering Physics*. 2014.
21. Sawada, A., *Theory of space-charge polarization for determining ionic constants of electrolytic solutions.* The Journal of chemical physics, 2007. **126**(22): p. 224515.
22. Peiris, T.A.N., *Microwave-assisted processing of solid materials for sustainable energy related electronic and optoelectronic applications*. 2014.
23. Guo, J., et al., *Optimization and experimental verification of coplanar interdigital electroadhesives.* Journal of Physics D: Applied Physics, 2016. **49**(41): p. 415304.
24. Hao, X., *A review on the dielectric materials for high energy-storage application.* Journal of Advanced Dielectrics, 2013. **3**(01): p. 1330001.
25. Raju, G.G., *Dielectrics in electric fields: Tables, Atoms, and Molecules*. 2017: CRC press.
26. USMA, D., *dies of ultifer Ti) O3.*
27. Chaudhari, V.A. and G.K. Bichile, *Synthesis, structural, and electrical properties of pure PbTiO3 ferroelectric ceramics.* Smart Materials Research, 2013. **2013**.
28. Bain, A.K. and P. Chand, *Ferroelectrics: Principles and applications*. 2017: John Wiley & Sons.

29. Cholleti, E.R., et al., *Mechanical behaviour of large strain capacitive sensor with barium titanate ecoflex composite used to detect human motion.* Robotics, 2021. **10**(2): p. 69.
30. Lee, J.K., K.S. Hong, and J.W. Jang, *Roles of Ba/Ti ratios in the dielectric properties of BaTiO3 ceramics.* Journal of the American Ceramic Society, 2001. **84**(9): p. 2001-2006.
31. Lines, M.E. and A.M. Glass, *Principles and applications of ferroelectrics and related materials*. 2001: Oxford university press.
32. Mills, A.A., *The lodestone: History, physics, and formation.* Annals of Science, 2004. **61**(3): p. 273-319.
33. Cullity, B.D. and C.D. Graham, *Introduction to magnetic materials*. 2011: John Wiley & Sons.
34. Bassani, F., G. Leidl, and P. Wyder, *Encyclopedia of Condensed Matter Physics (6 Volume Set).* MRS Bull, 2006. **31**: p. 192-208.
35. Nguyen, M.D., et al., *Experimental evidence of breakdown strength and its effect on energy-storage performance in normal and relaxor ferroelectric films.* Current Applied Physics, 2019. **19**(9): p. 1040-1045.
36. Izyumskaya, N., et al., *Processing, structure, properties, and applications of PZT thin films.* Critical reviews in solid state and materials sciences, 2007. **32**(3-4): p. 111-202.
37. Nwanji, E., J. Ugbodaga, and O. Daye, *SUSTAINABLE MEANS FOR ENERGY GENERATION: A MODEL FOR HARNESSING ENERGY FROM DOOR MOTION USING A PIEZO ELECTRIC MATERIAL*. 2017.
38. Vigoureux, P., *Physics without Einstein.* Electronics and Power, 1970. **16**(5): p. 198.
39. Foster, L.S., *New developments in ferromagnetic materials*. 1948, ACS Publications.
40. Jadhav, V.V., R.S. Mane, and P.V. Shinde, *Bismuth-Ferrite-Based Electrochemical Supercapacitors*. 2020: Springer.
41. Sugimoto, M., *The past, present, and future of ferrites.* Journal of the American Ceramic Society, 1999. **82**(2): p. 269-280.
42. Herrera, J.O., et al., *LiMnPO 4: Review on synthesis and electrochemical properties.* Journal of Materials Science and Chemical Engineering, 2015. **3**(05): p. 54.
43. Valenzuela, R., *Novel applications of ferrites.* Physics Research International, 2012. **2012**.
44. Verwey, E. and E. Heilmann, *Physical properties and cation arrangement of oxides with spinel structures I. Cation arrangement in spinels.* The Journal of Chemical Physics, 1947. **15**(4): p. 174-180.
45. Ortiz-Quiñonez, J.-L., U. Pal, and M.S. Villanueva, *Structural, magnetic, and catalytic evaluation of spinel Co, Ni, and Co–Ni ferrite nanoparticles fabricated by low-temperature solution combustion process.* ACS omega, 2018. **3**(11): p. 14986-15001.
46. Thien, J., et al., *Cationic ordering and its influence on the magnetic properties of Co-rich cobalt ferrite thin films prepared by reactive solid phase epitaxy on Nb-doped SrTiO3 (001).* Materials, 2021. **15**(1): p. 46.
47. Pullar, R.C., *Hexagonal ferrites: a review of the synthesis, properties and applications of hexaferrite ceramics.* Progress in Materials Science, 2012. **57**(7): p. 1191-1334.
48. Wu, J. and T. Wu, *A Bright New World of Ferroelectrics: Magic of Spontaneous Polarization*. 2020, ACS Publications. p. 52231-52233.
49. Makovec, D., et al., *Discrete evolution of the crystal structure during the growth of Ba-hexaferrite nanoplatelets.* Nanoscale, 2018. **10**(30): p. 14480-14491.
50. Geller, S. and M. Gilleo, *The crystal structure and ferrimagnetism of yttrium-iron garnet, Y3Fe2 (FeO4) 3.* Journal of Physics and Chemistry of solids, 1957. **3**(1-2): p. 30-36.
51. Köferstein, R. and S.G. Ebbinghaus, *Synthesis and characterization of nano-LaFeO3 powders by a soft-chemistry method and corresponding ceramics.* Solid State Ionics, 2013. **231**: p. 43-48.

52. Benz, M. and W.B. Euler, *Determination of the crystalline phases of poly (vinylidene fluoride) under different preparation conditions using differential scanning calorimetry and infrared spectroscopy.* Journal of applied polymer science, 2003. **89**(4): p. 1093-1100.
53. Cui, Z., et al., *Crystalline polymorphism in poly (vinylidenefluoride) membranes.* Progress in Polymer Science, 2015. **51**: p. 94-126.
54. Ameduri, B., *From vinylidene fluoride (VDF) to the applications of VDF-containing polymers and copolymers: recent developments and future trends.* Chemical reviews, 2009. **109**(12): p. 6632-6686.
55. Tao, M.-m., et al., *Effect of solvent power on PVDF membrane polymorphism during phase inversion.* Desalination, 2013. **316**: p. 137-145.
56. Nasir, M., et al., *Control of diameter, morphology, and structure of PVDF nanofiber fabricated by electrospray deposition.* Journal of Polymer Science Part B: Polymer Physics, 2006. **44**(5): p. 779-786.
57. Mohammadi, B., A.A. Yousefi, and S.M. Bellah, *Effect of tensile strain rate and elongation on crystalline structure and piezoelectric properties of PVDF thin films.* Polymer testing, 2007. **26**(1): p. 42-50.
58. Meng, N., et al., *Nanoscale interfacial electroactivity in PVDF/PVDF-TrFE blended films with enhanced dielectric and ferroelectric properties.* Journal of Materials Chemistry C, 2017. **5**(13): p. 3296-3305.
59. Li, Y., C. Liao, and S.C. Tjong, *Electrospun polyvinylidene fluoride-based fibrous scaffolds with piezoelectric characteristics for bone and neural tissue engineering.* Nanomaterials, 2019. **9**(7): p. 952.
60. Meng, N., et al., *Ultrahigh β-phase content poly (vinylidene fluoride) with relaxor-like ferroelectricity for high energy density capacitors.* Nature Communications, 2019. **10**(1): p. 4535.
61. Kabir, E., et al., *Pure β-phase formation in polyvinylidene fluoride (PVDF)-carbon nanotube composites.* Journal of Physics D: Applied Physics, 2017. **50**(16): p. 163002.
62. Botero, E., J. Nobrega, and D. Trombini, *Influence of NiFe 2 O 4 on β phase formation in PVDF composites.* Mater. Sci. Eng, 2020. **4**: p. 83-86.
63. Reainthippayasakul, W., *Silica-coated BaTiO3/P (VDF-CTFE) nanocomposites for electrical energy storage.* 2015.
64. Lovinger, A.J., *Annealing of poly (vinylidene fluoride) and formation of a fifth phase.* Macromolecules, 1982. **15**(1): p. 40-44.
65. Martín, J., et al., *Solid-state-processing of δ-PVDF.* Materials Horizons, 2017. **4**(3): p. 408-414.
66. Fujisaki, Y., *Poly (vinylidenefluoride-trifluoroethylene) P (VDF-TrFE)/semiconductor structure ferroelectric-gate FETs.* Ferroelectric-Gate Field Effect Transistor Memories: Device Physics and Applications, 2016: p. 157-183.
67. Yang, L., et al., *Preparation and magnetic performance of Co0. 8Fe2. 2O4 by a sol–gel method using cathode materials of spent Li-ion batteries.* Ceramics International, 2016. **42**(1): p. 1897-1902.
68. Qu, Y., et al., *The effect of reaction temperature on the particle size, structure and magnetic properties of coprecipitated CoFe2O4 nanoparticles.* Materials Letters, 2006. **60**(29-30): p. 3548-3552.
69. Dedi, et al. *Magnetic properties of cobalt ferrite synthesized by mechanical alloying*. in *AIP Conference Proceedings*. 2018. AIP Publishing LLC.
70. Cernea, M., et al., *CoFe2O4 magnetic ceramic derived from gel and densified by spark plasma sintering.* Journal of Alloys and Compounds, 2016. **656**: p. 854-862.
71. Swatsitang, E., et al., *Characterization and magnetic properties of cobalt ferrite nanoparticles.* Journal of Alloys and Compounds, 2016. **664**: p. 792-797.

72. Veiseh, O., J.W. Gunn, and M. Zhang, *Design and fabrication of magnetic nanoparticles for targeted drug delivery and imaging.* Advanced drug delivery reviews, 2010. **62**(3): p. 284-304.
73. Singh, R., N.K. Singh, and J.P. Singh, *Electrocatalytic properties of new active ternary ferrite film anodes for O2 evolution in alkaline medium.* Electrochimica acta, 2002. **47**(24): p. 3873-3879.
74. Chithra, M., et al., *Exchange spring like magnetic behavior in cobalt ferrite nanoparticles.* Journal of Magnetism and Magnetic Materials, 2016. **401**: p. 1-8.
75. Kim, D.-H., et al., *Heat generation of aqueously dispersed CoFe2O4 nanoparticles as heating agents for magnetically activated drug delivery and hyperthermia.* Journal of Magnetism and Magnetic Materials, 2008. **320**(19): p. 2390-2396.
76. Hosni, N., et al., *Semi-hard magnetic properties of nanoparticles of cobalt ferrite synthesized by the co-precipitation process.* Journal of Alloys and Compounds, 2017. **694**: p. 1295-1301.
77. Fiebig, M., et al., *The evolution of multiferroics.* Nature Reviews Materials, 2016. **1**(8): p. 1-14.
78. Lottermoser, T. and D. Meier, *A short history of multiferroics.* Physical Sciences Reviews, 2020. **6**(2): p. 20200032.
79. Chang, S.-J., et al., *GdFe0. 8Ni0. 2O3: a multiferroic material for low-power spintronic devices with high storage capacity.* ACS Applied Materials & Interfaces, 2019. **11**(34): p. 31562-31572.
80. Surowiak, Z. and D. Bochenek, *Multiferroic materials for sensors, transducers and memory devices.* 2008.
81. Vopson, M.M., *Fundamentals of multiferroic materials and their possible applications.* Critical Reviews in Solid State and Materials Sciences, 2015. **40**(4): p. 223-250.
82. Dehsari, H.S., M.H. Amiri, and K. Asadi, *Solution-Processed Multiferroic Thin-Films with Large Magnetoelectric Coupling at Room-Temperature.* ACS nano, 2023. **17**(9): p. 8064.
83. Schmid, H., *Multi-ferroic magnetoelectrics.* Ferroelectrics, 1994. **162**(1): p. 317-338.
84. Zhai, J., et al., *Magnetoelectric laminate composites: an overview.* Journal of the American Ceramic Society, 2008. **91**(2): p. 351-358.
85. Van den Boomgaard, J. and R. Born, *A sintered magnetoelectric composite material BaTiO 3-Ni (Co, Mn) Fe 2 O 4.* Journal of Materials Science, 1978. **13**: p. 1538-1548.
86. Zhai, J., et al., *Coupled magnetodielectric properties of laminated PbZr 0.53 Ti 0.47 O 3/NiFe 2 O 4 ceramics.* Journal of applied physics, 2004. **95**(10): p. 5685-5690.
87. Vadivel, M., et al., *CTAB cationic surfactant assisted synthesis of CoFe2O4 magnetic nanoparticles.* Ceramics International, 2016. **42**(16): p. 19320-19328.
88. Patterson, A., *The Scherrer formula for X-ray particle size determination.* Physical review, 1939. **56**(10): p. 978.
89. Feinle, A., M.S. Elsaesser, and N. Huesing, *Sol–gel synthesis of monolithic materials with hierarchical porosity.* Chemical Society Reviews, 2016. **45**(12): p. 3377-3399.
90. Liao, Y., Y. Xu, and Y. Chan, *Semiconductor nanocrystals in sol–gel derived matrices.* Physical Chemistry Chemical Physics, 2013. **15**(33): p. 13694-13704.
91. Owens, G.J., et al., *Sol–gel based materials for biomedical applications.* Progress in materials science, 2016. **77**: p. 1-79.
92. Niederberger, M. and N. Pinna, *Metal oxide nanoparticles in organic solvents: synthesis, formation, assembly and application*. 2009: Springer Science & Business Media.
93. Bokov, D., et al., *Nanomaterial by sol-gel method: synthesis and application.* Advances in Materials Science and Engineering, 2021. **2021**: p. 1-21.
94. Li, Y., T. White, and S.H. Lim, *Structure control and its influence on photoactivity and phase transformation of TiO.* Rev. Adv. Mater. Sci, 2003. **5**: p. 211-215.
95. Shinde, S., et al., *Structural, optoelectronic, luminescence and thermal properties of Ga-doped zinc oxide thin films.* Applied Surface Science, 2012. **258**(24): p. 9969-9976.

96. Patil, S., S. Shinde, and K. Rajpure, *Physical properties of spray deposited Ni-doped zinc oxide thin films.* Ceramics International, 2013. **39**(4): p. 3901-3907.
97. Shinde, S., et al., *Influence of tin doping onto structural, morphological, optoelectronic and impedance properties of sprayed ZnO thin films.* Journal of Alloys and Compounds, 2013. **551**: p. 688-693.
98. Shinde, S., C. Bhosale, and K. Rajpure, *Photocatalytic degradation of toluene using sprayed N-doped ZnO thin films in aqueous suspension.* Journal of Photochemistry and Photobiology B: Biology, 2012. **113**: p. 70-77.
99. Shinde, S., C. Bhosale, and K. Rajpure, *Photoelectrochemical properties of highly mobilized Li-doped ZnO thin films.* Journal of Photochemistry and Photobiology B: Biology, 2013. **120**: p. 1-9.
100. Zhu, L., *Exploring strategies for high dielectric constant and low loss polymer dielectrics.* The journal of physical chemistry letters, 2014. **5**(21): p. 3677-3687.
101. Xu, F., et al., *Controllably degradable transient electronic antennas based on water-soluble PVA/TiO2 films.* Journal of materials science, 2018. **53**(4): p. 2638-2647.
102. Thornton, J.A., *Sputter Coating—Its Principles and Potential.* SAE Transactions, 1973: p. 1787-1805.
103. Koops, C., *On the dispersion of resistivity and dielectric constant of some semiconductors at audiofrequencies.* Physical review, 1951. **83**(1): p. 121.
104. Bunaciu, A.A., E.G. UdriŞTioiu, and H.Y. Aboul-Enein, *X-ray diffraction: instrumentation and applications.* Critical reviews in analytical chemistry, 2015. **45**(4): p. 289-299.
105. Stan, C.V., et al., *X-ray diffraction under extreme conditions at the Advanced Light Source.* Quantum Beam Science, 2018. **2**(1): p. 4.
106. Falsafi, S.R., H. Rostamabadi, and S.M. Jafari, *X-ray diffraction (XRD) of nanoencapsulated food ingredients*, in *Characterization of nanoencapsulated food ingredients*. 2020, Elsevier. p. 271-293.
107. Hall, D., M. Cain, and M. Stewart. *Ferroelectric hysteresis measurement & analysis*. in *Minutes of the NPL CAM7 IAG Meeting*. 1998.
108. *Capacitance of Parallel Plates.*
109. Houshiar, M., et al., *Synthesis of cobalt ferrite (CoFe2O4) nanoparticles using combustion, coprecipitation, and precipitation methods: A comparison study of size, structural, and magnetic properties.* Journal of Magnetism and Magnetic Materials, 2014. **371**: p. 43-48.
110. Siva, K.V., A. Kumar, and A. Arockiarajan, *Structural, magnetic and magnetoelectric investigations on CoFe2O4 prepared via various wet chemical synthesis route: A Comparative Study.* Journal of Magnetism and Magnetic Materials, 2021. **535**: p. 168065.
111. Rodríguez-Rodríguez, A.A., et al., *Spinel-type ferrite nanoparticles: Synthesis by the oil-in-water microemulsion reaction method and photocatalytic water-splitting evaluation.* international journal of hydrogen energy, 2019. **44**(24): p. 12421-12429.
112. Zhang, R., et al., *Dielectric and magnetic properties of CoFe2O4 prepared by sol-gel auto-combustion method.* Materials Research Bulletin, 2018. **98**: p. 133-138.
113. Mu, X., et al., *Poly (vinylidene fluoride-trifluoroethylene)/cobalt ferrite composite films with a self-biased magnetoelectric effect for flexible AC magnetic sensors.* Journal of Materials Science, 2021. **56**: p. 9728-9740.
114. Li, C., et al., *All polymer dielectric films for achieving high energy density film capacitors by blending poly (vinylidene fluoride-trifluoroethylene-chlorofluoroethylene) with aromatic polythiourea.* Nanoscale research letters, 2020. **15**(1): p. 1-9.
115. Ng, C., et al., *Structural control of the dielectric, pyroelectric and ferroelectric properties of poly (vinylidene fluoride-co-trifluoroethylene) thin films.* Physical Chemistry Chemical Physics, 2020. **22**(4): p. 2414-2423.

116. Zhang, J., et al., *The effect of magnetic nanoparticles on the morphology, ferroelectric, and magnetoelectric behaviors of CFO/P (VDF-TrFE) 0–3 nanocomposites.* Journal of Applied Physics, 2009. **105**(5): p. 054102.
117. Behera, C., R. Choudhary, and P.R. Das, *Development of multiferroism in PVDF with CoFe 2 O 4 nanoparticles.* Journal of Polymer Research, 2017. **24**: p. 1-13.
118. Reynolds, N.M., et al., *Spectroscopic analysis of the electric field induced structural changes in vinylidene fluoride/trifluoroethylene copolymers.* Macromolecules, 1989. **22**(3): p. 1092-1100.
119. Cai, K., et al., *A green route to a low cost anisotropic MoS2/poly (vinylidene fluoride) nanocomposite with ultrahigh electroactive phase and improved electrical and mechanical properties.* ACS Sustainable Chemistry & Engineering, 2018. **6**(4): p. 5043-5052.
120. Kefeni, K.K., T.A. Msagati, and B.B. Mamba, *Ferrite nanoparticles: synthesis, characterisation and applications in electronic device.* Materials Science and Engineering: B, 2017. **215**: p. 37-55.
121. Sharifi Dehsari, H., *Towards multi-ferroic nanocomposites from ferroelectric polymer and magnetic nanoparticles*. 2019, Johannes Gutenberg-Universität Mainz.
122. Sharma, M., J.K. Quamara, and A. Gaur, *Behaviour of multiphase PVDF in (1− x) PVDF/(x) BaTiO 3 nanocomposite films: structural, optical, dielectric and ferroelectric properties.* Journal of Materials Science: Materials in Electronics, 2018. **29**: p. 10875-10884.
123. Martins, P., et al., *Optimizing piezoelectric and magnetoelectric responses on CoFe2O4/P (VDF-TrFE) nanocomposites.* Journal of Physics D: Applied Physics, 2011. **44**(49): p. 495303.
124. Lu, X., et al., *Dielectric property and ac conductivity of P (VDF-CTFE)-PLZST polymer-ceramic composite films.* 2019. **45**(7): p. 8979-8987.
125. Fröhlich, H., *Theory of dielectrics: dielectric constant and dielectric loss*. Vol. 190. 1958: Oxford University Press, USA.
126. Gregorio, R. and E.J.J.o.m.s. Ueno, *Effect of crystalline phase, orientation and temperature on the dielectric properties of poly (vinylidene fluoride)(PVDF).* 1999. **34**: p. 4489-4500.
127. Arifin, D.E.S. and d.J. Ruan. *Study on the curie transition of P (VDF-TrFE) copolymer*. in *IOP Conference Series: Materials Science and Engineering*. 2018. IOP Publishing.
128. Li, Z., et al., *Ferro-and piezo-electric properties of a poly (vinyl fluoride) film with high ferro-to para-electric phase transition temperature.* 2015. **5**(99): p. 80950-80955.
129. Dwivedi, S., et al., *Relaxation processes and conduction behaviour in PVDF-TrFE and KNN-based composites.* Polymer, 2021. **232**: p. 124164.
130. Zhang, Y., et al., *Dielectric relaxation processes in PVDF composite.* 2020. **91**: p. 106801.
131. Van Groenou, A.B., et al., *Magnetism, microstructure and crystal chemistry of spinel ferrites.* 1969. **3**(6): p. 317-392.
132. Rana, D.K., et al., *Electrical and room temperature multiferroic properties of polyvinylidene fluoride nanocomposites doped with nickel ferrite nanoparticles.* 2019. **43**(7): p. 3128-3138.